Modeling moisture-induced cockling deformations of paper sheets

Smeenk, R.M.A.

Award date:
2019

Modeling moisture-induced cockling deformations of paper sheets

Under supervision of:	Dr. ir. L.H. (Louis) Saes	*Océ-Technologies B.V.*
	Dr. ir. R.H.J. (Ron) Peerlings	*Mechanical Engineering*
	Dr. ir. J.M.L. (Jos) Maubach	*Industrial and Applied Mathematics*
	Dr. ir. A.A.F. (Fons) van de Ven	*Industrial and Applied Mathematics*

Randy Smeenk 0811900 r.m.a.smeenk@student.tue.nl

A thesis submitted to Eindhoven University of Technology in partial fulfillment of the requirements for the degree of
Master of Science

Eindhoven, February 25, 2019

Abstract

New methods are sought to improve the two-dimensional post-buckling model of a paper sheet subject to a moisture-affected area, in terms of simulation time and robustness. This is investigated by extracting difficult parts of the two-dimensional plate model. Difficult parts are considered to be buckling and contact, which are studied independently as well as jointly using a non-linear one-dimensional finite element beam model. Eigenvalue analysis offers perspective regarding the buckling phenomena. Contact is investigated by means of a penalty method. The combination of contact and buckling is investigated via a cone constrained eigenvalue problem. The semi-smooth Newton algorithm used for the cone constrained eigenvalue problem is eventually applied to a two-dimensional finite element plate model. The resulting solutions from the semi-smooth Newton algorithm seem plausible, but so far incorrect, implying further research is necessary to make this method applicable. Regarding simulation time and robustness there is a significant improvement in simulation time, but robustness is not necessarily improved.

Acknowledgements

Writing these acknowledgements marks the end of my adventure at Eindhoven University of Technology as a student. This report is the result of almost a year of work at Océ-Technologies B.V., and what a blast it was. I thank all the people who have helped me in making this thesis possible.

First of all I thank Louis Saes, who was my daily supervisor at Océ-Technologies B.V. throughout this project. Furthermore, thanks Louis for your enthusiasm, insightfull discussions and the freedom you gave me to choose my own directions during the project.

At Eindhoven University of Technology I received excellent guidance from Ron Peerlings, Jos Maubach and Fons van de Ven. The discussions we had at the university and Océ-Technologies B.V. always offered new perspectives and inspiration on how to proceed. The guidance of Ron in modeling and simulation of mechanics is greatly appreciated. Thank you Jos for guiding me through the mathematical aspects of the project. Thank you Fons for the tireless work you have put into commenting on my intermediate work, and sharing parts of your vast knowledge of mechanics.

Thanks also to Daan van der Woude and Tom Leenen for being such great friends and study buddies during the master.

Last, but certainly not least, I thank my family, for their continuous love and support.

Table of Contents

1 Introduction

1.1 Background information

Nowadays, an effective printing process of high quality images knows two demands: first it has to maintain this quality of the image, and secondly the printing time must be as short as possible. Highly qualified printing units are necessary to satisfy these demands. A typical high speed inkjet printer uses 3 print-heads per color, where each print-head contains approximately 8000 nozzles. It is capable of delivering 80 million droplets per second, resulting in up to 294 A4 sheets per minute. The ink nozzles should be perfectly aligned to the paper sheet surface to be able to produce such high quality prints. Unfortunately, the paper sheets are not entirely flat and therefore it is not possible to align the nozzles perfectly to the paper sheet. Moreover, dropping ink onto the paper increases the moisture content of the paper sheet, inducing tensions and deformations. These moisture-induced deformations will compromise the print quality if they lead to in- and out-of-plane displacement of (parts of) the sheet. The different kinds of deformation paper can undergo are depicted in Fig. 1.1.

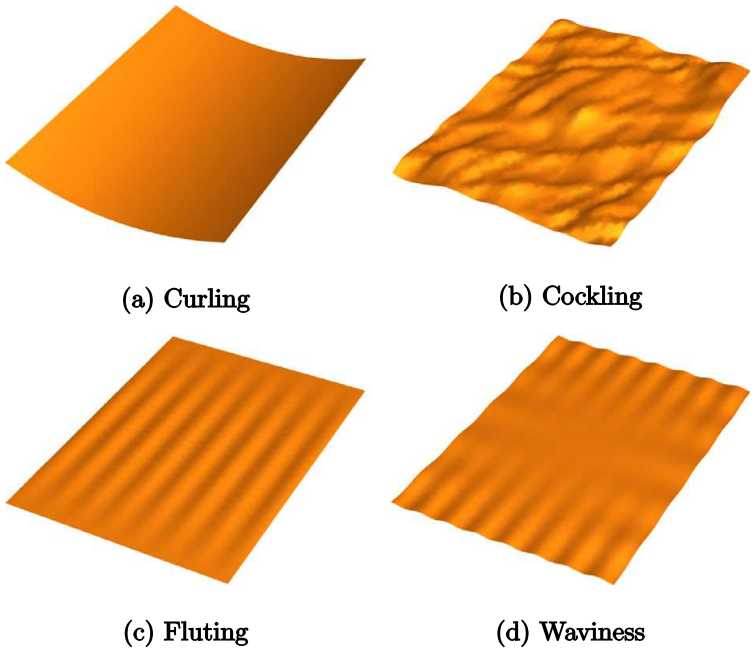

Figure 1.1: *Schematic representation of the deformations [1].*

These kind of deformations are investigated both experimentally and numerically in literature, see [1–3]. In this thesis we focus on numerical modeling of the cockling process. The cockling process is characterized by bifurcations that occur locally in the form of out-of-plane buckling deformations. A *bifurcation* is described by Crawford [4] as:

"*some sort of branching process, widely used to describe any situation in which the qualitative, topological picture of the object we are studying alters with a change of the parameters on which the object depends.*"

During the printing process the paper sheet is fixed to the printing table using suction: small holes are located in the printing table which enables suction of the paper sheet onto the printing table. This sucking process has two functionalities:

1. The paper sheet is not able to move during the printing process.

2. It resists the cockling process.

Nevertheless, it does not avoid the cockling process completely. Developing a numerical model that incorporates both the cockling process and contact between the paper sheet and the printing table is a difficult task. Océ-Technologies B.V. managed to create such a model in the commercially available finite element package Marc & Mentat.

1.2 Current approach and its limits

The numerical model in Marc & Mentat is a non-linear simulation. Moisture is added to a part of the paper sheet, and the amount of moisture is increased. At a certain moisture content cockling deformations occur, and adding more moisture makes these cockling deformations evolve in time.

One phenomenon the numerical model in Marc & Mentat has to deal with is buckling (cockling), which is a type of bifurcation. Since it is a bifurcation problem it contains a bifurcation point at which multiple solutions exist. To clarify this concept we illustrate it with an example of a beam subject to an axial compressive load P, see Fig. 1.2.

Figure 1.2: *Illustrative example of buckling, a special type of bifurcation, of a beam subject to an axial compressive load P.*

The load P is increased until a critical value is reached. As long as the load P is below this critical value, the beam is compressed axially and remains straight and horizontal. When P equals this critical value we are in the bifurcation point, and we have three possible solutions: two possible buckled configurations and the trivial configuration, see Fig. 1.2. This implies that no unique solution exists, which makes it numerically difficult to solve. Unless special measures are taken, a perfectly straight beam, with a compressive axial load P perfectly aligned with the central line of the beam tends to not buckle at all in simulations. This implies the beam remains in the trivial configuration, even though the buckled configurations are also solutions. This non-uniqueness can be bypassed by imposing a small initial disturbance on the initial configuration of the beam, e.g. a small initial displacement. Besides bypassing the non-uniqueness this also triggers buckling in the sense that the initial configuration is no solution, particularly when the applied load P increases above the critical value. A simulation with an initial disturbance where the load is increased above the critical value, is called a post-buckling simulation in the sequel. A disadvantage is that the shape of the deformed buckled configuration may depend on the initial disturbance.
Océ-Technologies B.V. applied this strategy in their model in Marc & Mentat. They imposed a small initial out-of-plane displacement on the initial configuration of the paper sheet. This avoids the initial configuration to be a solution, and it bypasses the non-uniqueness. Even though the small initial out-of-plane displacement is random it still induces some correlation between the initial and final sheet shape.

Another phenomenon present in these simulations is contact. The paper sheet is pushed onto the printing table using a pressure which mimics the suction present in the printer. When the cockling deformations are evolving over time the model has to check and update the contact conditions for each node present in the mesh. In case of buckling (cockling) it might occur that

nodes penetrate the table, which is not allowed and results in additional iterations to determine the correct solution. In some cases this even results in a lack of convergence of the simulation. Besides the uncertainty of convergence of the simulation, the contact conditions also increase the simulation time, which is a disadvantage.
The combination of these phenomena affects the robustness and simulation time of the model. The simulation times vary between a few minutes to a few days. This difference in simulation time is illustrated by an example. The deformed configurations of two "identical" simulations of the model in Marc & Mentat created by Océ-Technologies B.V., except for their random initial out-of-plane displacements, are shown in Fig. 1.3. The moisture-affected area is approximately the half paper sheet. The paper sheets are in contact with the printing table and a pressure is applied. The deformed configurations look similar, but the simulation of Fig. 1.3a is more than twice as fast compared to the simulation of Fig. 1.3b.

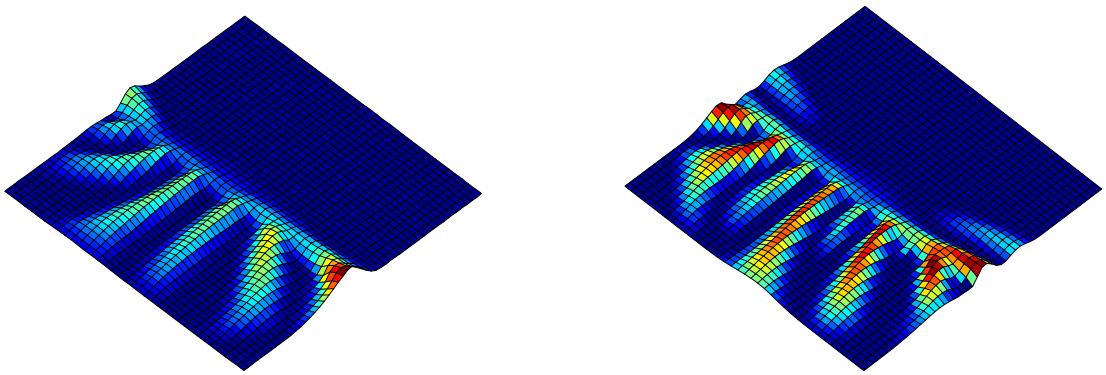

(a) *Result of simulation 1.* **(b)** *Result of simulation 2.*

Figure 1.3: *Results of two "identical" simulations, except for the random initial out-of-plane displacement.*

This example illustrates that a small change in initial conditions has a large impact on the simulation time.

1.3 Objectives

The Marc & Mentat model created by Océ-Technologies B.V. is able to mimic the moisture-induced cockling process of a paper sheet sucked to a printing table. However, it fails when it comes to robustness and simulation time. Therefore, one of the research questions is:

Is it possible to increase the robustness of the current model and decrease the simulation time, and if so, how can it be improved?

Océ-Technologies B.V. is particularly interested in determining the critical amount of moisture which can be added before buckling occurs, and how this value is related to the applied pressure (suction). To answer this question it is sufficient to consider the pre-buckling (including buckling) regime only. In principle, this should allow us to simplify the post-buckling simulation to a buckling simulation. The in-plane displacements in the pre-buckling regime are negligibly small, which allows us to apply the simplification of only considering the out-of-plane displacements. Since the paper sheet is subjected to contact conditions and an applied pressure (suction), we are not able to consider it as an ordinary buckling analysis. Therefore, we state the second research question:

How to qualify the paper sheet subjected to contact conditions and an applied pressure as a buckling simulation, which enables us to determine the critical moisture value at which buckling occurs?

1.4 Solution approach

To answer these research questions we start by considering and investigating the difficult parts of the two-dimensional[1] model from Marc & Mentat solely. The difficult parts refer to buckling (cockling) of the paper sheet and contact between the paper sheet and the printing table. To get a better understanding of these phenomena we create a one-dimensional beam model which mimics the contact and buckling conditions of the two-dimensional model. Since the precise finite element implementation in Marc & Mentat is unknown we develop a new model in MATLAB. To get insight in pure buckling and pure contact we consider them seperately. The buckling process is characterized as an eigenvalue problem, and solved using eigenvalue analysis techniques. Implementation of contact is possible using several techniques. We choose to implement contact by means of a penalty method. Eventually buckling and contact are treated simultaneously and a special form of an eigenvalue analysis is applied to obtain the solution. After gaining insight in the numerical aspects of buckling and contact we return to the two-dimensional model, where the newly learned techniques are applied.

1.5 Outline

The one-dimensional beam model used to investigate the contact and buckling phenomena is derived, discretized and validated in Sec. 2. When the model is validated we are able to use it to investigate buckling and contact, which is done in Sec. 3. We start with eigenvalue analysis techniques to model the buckling. After that we investigate contact conditions by means of the penalty method. Buckling and contact are combined and investigated together in the last part of Sec. 3. We want to apply the outcomes of Sec. 3 to the two-dimensional plate model. This is achieved by deriving a two-dimensional plate model on which the outcomes can be applied. Sec. 4 contains the derivation, discretization and validation of a simplified two-dimensional plate model, which is valid in the pre-buckling regime. The results of the two-dimensional simulations are given in Sec. 5. The concluding remarks and recommendations for future work are given in Sec. 6.

[1] Two-dimensional model refers to a thin plate, which can be interpreted as a two-dimensional object. One-dimensional beam model refers to a slender beam, which can be interpreted as a one-dimensional object.

2 Beam model

In this section the one-dimensional beam model is derived. First of all the kinematics and the assumptions we make are given. After that the equilibrium equations are derived and the strong form is given. Dimensionless quantities are introduced to turn the formulation in dimensionless form. After that the weak form is derived, and discretized using the *Bubnov-Galerkin* method. The model is validated through a mesh convergence study and by comparison with Marc & Mentat.

2.1 Kinematics

A slender beam is considered and shear effects are neglected such that Euler-Bernoulli theory (EBT) [5] can be used. Slender implies that $\varepsilon = R/L \ll 1$, with $R = \sqrt{A}$, A [m^2] the cross-sectional area, and L [m] the length of the beam. Fig. 2.1 shows a sketch of a slender beam.

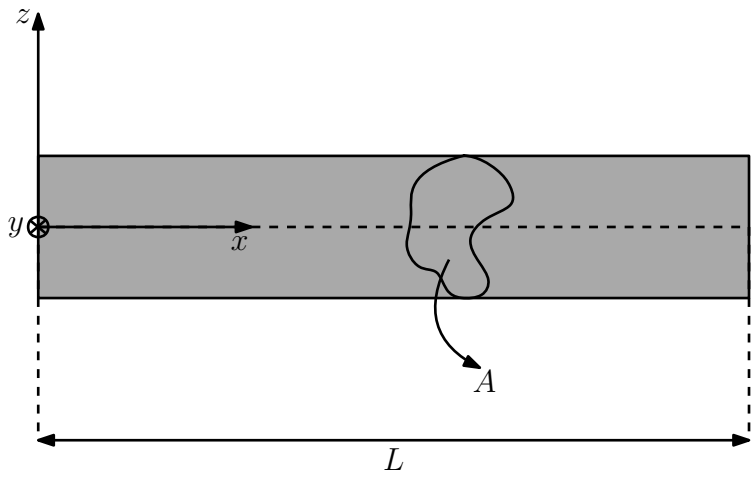

Figure 2.1: *Sketch of slender beam of length L, with arbitrary cross-section A.*

The $\{Oxyz\}$-coordinate system is chosen with the origin O in the left support, the x-axis along the central line of the beam, and the y- and z-axes transverse to the beam, along the central principle axes of the cross section.
The deformation pattern acting on the beam consists of bending in the x-z-plane and stretching in x-direction. For the bending deformation we make the following assumptions:

1. The length L of the central line of the beam does not change under bending.
2. The lateral surface of the beam is free of stress.
3. Plane normal cross-sections remain normal and planar after bending, i.e. no shear deformations.
4. All stresses except σ_{xx} are neglected.
5. The strains are sufficiently small, moderately large rotations are allowed (more precise definitions follow).

Any material point $\mathcal{P}$ in the body $\mathcal{B}$ of the beam can be described by the position vector $\underline{\boldsymbol{x}} = (x, y, z)^T \in \mathcal{B}$. The central line of the beam is defined as the domain

$$\mathcal{D} := \{\underline{\boldsymbol{x}} \mid x \in (0, L), y = z = 0\}, \tag{2.1}$$

and the origin is placed at the beginning of the central line, see Fig. 2.1. The set $\partial\mathcal{D} := \{0, L\}$ is used to indicate the boundary points of $\mathcal{D}$. Together we have $\overline{\mathcal{D}} := \mathcal{D} \cup \partial\mathcal{D}$, which is referred to as the closure of $\mathcal{D}$. The EBT is based on the displacement field $\underline{\boldsymbol{u}} = \underline{\boldsymbol{u}}(\underline{\boldsymbol{x}})$, given by [5]

$$\underline{\boldsymbol{u}}(\underline{\boldsymbol{x}}) = \begin{bmatrix} u_1(\underline{\boldsymbol{x}}) \\ u_2(\underline{\boldsymbol{x}}) \\ u_3(\underline{\boldsymbol{x}}) \end{bmatrix} = \begin{bmatrix} u(x) - z\theta(x) \\ 0 \\ w(x) \end{bmatrix}. \tag{2.2}$$

The displacements $u(x)$ and $w(x)$ represent the axial respectively transverse displacements of a point x on the central line of the beam, and are functions of the axial coordinate x only. The angle between the central line of the deformed beam and the horizontal axis is denoted by $\theta(x)$. Furthermore s represents the arc length of the deflected beam, see Fig. 2.2.

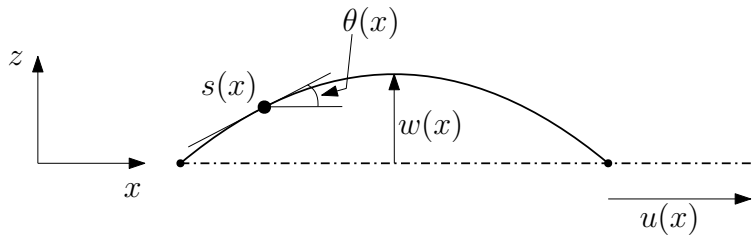

Figure 2.2: *Definition of $\theta(s)$ and a point s on the deformed beams arc.*

From Fig. 2.2 we infer that $\tan(\theta) = w_{,x}$, where a comma denotes differentiation with respect to the corresponding variable. Assuming θ to be sufficiently small allows us to use a Taylor approximation:

$$\tan(\theta) \approx \theta + \mathcal{O}(\theta^3) \tag{2.3}$$

such that $\theta \approx w_{,x}$ is a valid approximation within a second-order approximation. For the displacements of the beam we assume the axial displacement u to be one order smaller in R/L than the deflection w, which we assume of the same order as R. This allows for moderately large rotations and are known as the so-called *Von-Kármán* strains [1]. Employing these assumptions in the Green-Lagrange strain tensor results in one non-zero strain component:

$$\begin{aligned} \varepsilon_{xx} &= u_{,x} + \frac{1}{2}\theta^2 - z\theta_{,x} \\ &\approx u_{,x} + \frac{1}{2}w_{,x}^2 - zw_{,xx} \\ &= \varepsilon_{xx}^{(0)} + z\varepsilon_{xx}^{(1)} \\ \varepsilon_{xx}^{(0)} &:= u_{,x} + \frac{1}{2}w_{,x}^2, \qquad \varepsilon_{xx}^{(1)} := -w_{,xx}. \end{aligned} \tag{2.4}$$

The $\varepsilon_{xx}^{(0)}$ component describes the stretching of the beam, whereas bending of the beam is described by $\varepsilon_{xx}^{(1)}$. The constitutive equation that relates the stresses to the strains is given by

$$\sigma_{xx} = E\varepsilon_{xx}, \tag{2.5}$$

and is known as Hooke's law, with E [N/m^2] the Young's modulus.

2.2 Equilibrium equations

The cockling of a paper sheet is a form of buckling. This buckling process is mimicked in the one-dimensional beam model via an axial compressive load P [N]. Suction of the paper sheet to

the printing table is incorporated in the one-dimensional beam model via a constant transverse load per unit of length q [N/m]. Contact conditions between the sheet of paper and the printing table are introduced later, see Sec. 3.2. A sketch of the one-dimensional beam model is shown in Fig. 2.3.

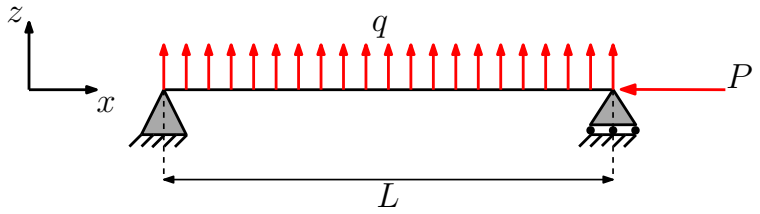

Figure 2.3: *Pinned-hinged Euler-Bernoulli beam subjected to an axial compressive force P, and distributed transverse load q.*

The beam is simply supported by a fixed support at the left end and a sliding support at the right end. The length of the beam is L and its cross-sectional area A. Furthermore we assume the beam to be *slender*. The beam is compressed in the x-direction and after buckling, bending of the beam is in the x-z-plane. The central line goes through the geometric centroids of the cross section, such that

$$(A, 0, I) = \int_A (1, z, z^2) \mathrm{d}A, \tag{2.6}$$

with I [m^4] the second moment of area.
From the *cross-sectional forces* we need the normal force N [N], the bending moment about the y-axis (in the x-z-plane) M [Nm], and the shear force in z-direction Q [N], which are defined in terms of the stresses by

$$N := \int_A \sigma_{xx} \mathrm{d}A, \qquad M := \int_A z\sigma_{xx} \mathrm{d}A, \qquad Q := \int_A \sigma_{xz} \mathrm{d}A. \tag{2.7}$$

NOTE: Although it was assumed that $\sigma_{xz} = 0$ (i.e. negligible), its integral resulting in the shear force Q is not. This may seem ambiguous, but is fully consistent within the Euler-Bernoulli beam theory.
Following Vaz and Silva [6], we derive the global equilibrium equations, which describe force and moment equilibrium of a small part ds of the deflected beam, see Fig. 2.4.

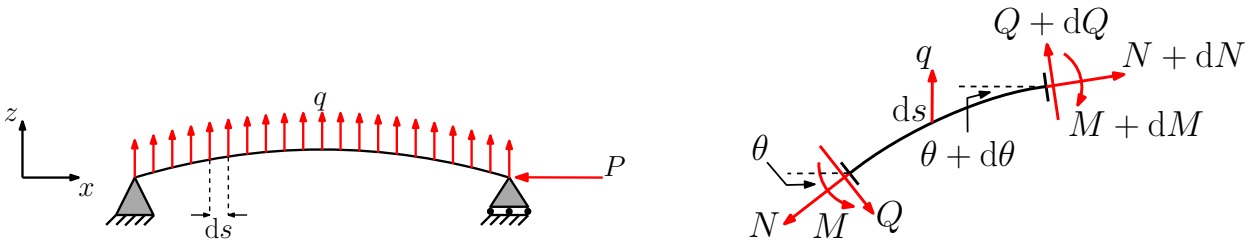

(a) *Illustration of a small part* ds *of the beam.*

(b) *Forces and moments acting on a small part* ds *of the beam.*

Figure 2.4: *Forces and moments acting on a small part* ds *of deformed the beam.*

Here s is the arc length of the deflected beam, and the global forces N, M and Q are considered as functions of s. The following global equilibrium equations refer to the buckled state and are non-linear and exact for this state. This formulation can be used for *post-buckling* analysis. For

our purpose, we shall only use a partly linearized version (i.e. maintaining the non-linear term $Nw_{,x}$) in which we assume, according to Eq. 2.3, the angle of deflection $\theta \ll 1$, with $\tan(\theta) = w_{,x}$. Force equilibrium in horizontal and vertical direction, and moment equilibrium of an infinitesimal small piece ds, results in (here $\mathrm{d}N = N_{,s}\mathrm{d}s$, etc. and terms of $\mathcal{O}(\mathrm{d}s^2)$ are neglected)

$$\begin{aligned}
\text{Hor}: \quad & (N + \mathrm{d}N)\cos(\theta + \mathrm{d}\theta) - N\cos(\theta) + Q\sin(\theta) - (Q + \mathrm{d}Q)\sin(\theta + \mathrm{d}\theta) && = 0, \\
\text{Ver}: \quad & (N + \mathrm{d}N)\sin(\theta + d\theta) - N\sin(\theta) + (Q + \mathrm{d}Q)\cos(\theta + \mathrm{d}\theta) - Q\cos(\theta) + q\mathrm{d}s && = 0, \\
\text{Mom}: \quad & M + \mathrm{d}M - M - Q\mathrm{d}s && = 0.
\end{aligned}$$

Linearizing the above equations by the use of $\theta \ll 1$, implying that $\mathrm{d}x = \cos(\theta)\mathrm{d}s \approx \mathrm{d}s$ and $\theta = w_{,x}(x)$, we obtain

$$\begin{aligned}
N_{,x} - (Qw_{,x})_{,x} &= 0, \\
(Nw_{,x})_{,x} + Q_{,x} + q &= 0, \\
M_{,x} - Q &= 0.
\end{aligned} \tag{2.8}$$

As we will show further on in Sec. 2.3, the term $Qw_{,x} = M_{,x}w_{,x}$ is $\mathcal{O}(\varepsilon^2)$ with respect to N, and hence must be neglected in the first equation of Eq. 2.8, whereas the term $Nw_{,x}$ is maintained. Moreover, we eliminate Q from the last two equations. This results in

$$\begin{aligned}
N_{,x} &= 0, \\
M_{,xx} + (Nw_{,x})_{,x} + q &= 0.
\end{aligned} \tag{2.9}$$

The first equation implies that N must be equal to the applied compressive load in the right support of the beam, so $N = -P$. Moreover, we need constitutive equations for N and M, which follow from Eq. 2.7 after substitution of Eq. 2.4 and Eq. 2.5:

$$\begin{aligned}
N &= EA\varepsilon^{(0)}_{xx} = EA\left(u_{,x} + \frac{1}{2}(w_{,x})^2\right), \\
M &= EI\varepsilon^{(1)}_{xx} = -EIw_{,xx}.
\end{aligned} \tag{2.10}$$

Substituting these relations in Eq. 2.9, we arrive at

$$\begin{aligned}
EA\left(u_{,x} + \frac{1}{2}(w_{,x})^2\right)_{,x} &= 0, \\
EIw_{,xxxx} + Pw_{,xx} &= q.
\end{aligned} \tag{2.11}$$

The differential equations in Eq. 2.11 govern axial equilibrium and transverse equilibrium, respectively, and are well known in literature, see e.g. [7,8]. The system of Eq. 2.11 forms a set of coupled differential equations, and we will solve them simultaneously using (non-linear) finite element technology, as this is also done in Marc & Mentat. It is also possible to solve the transverse equilibrium equation first and substitute the solution in the axial equilibrium equation, to solve for the axial displacement u. But we will not follow this way here because Marc & Mentat interprets it as a non-linear model too. The strong form is obtained by supplementing the differential equations with kinematic and dynamic (or natural) boundary conditions given by

$$u(0) = 0, \qquad w(0) = w(L) = 0, \tag{2.12}$$

and

$$N(L) = -P, \qquad M(0) = M(L) = 0. \tag{2.13}$$

Recapitulation of the previous results can be written in the strong form problem:

$$(\mathbf{S})\begin{cases} \text{Given constants } E, A, I, L, q, P, \\ \text{find } (u, w) \in C^1(\mathcal{D}) \times C^4(\mathcal{D}), \text{ such that,} \\ (u_{,x} + \dfrac{1}{2}(w_{,x})^2)_{,x} = 0, \\ EIw_{,xxxx} + Pw_{,xx} = q, \\ u|_{x=0} = w|_{\partial\mathcal{D}} = 0, \\ (u_{,x} + \dfrac{1}{2}(w_{,x})^2)\Big|_{x=L} = -P, \quad w_{,xx}|_{\partial\mathcal{D}} = 0. \end{cases} \tag{2.14}$$

2.3 Dimensionless form

The pre-assumption of our non-dimensionalization process is that $w/L = \mathcal{O}(\varepsilon)$, $w/R = \mathcal{O}(1)$ and $u/R = \mathcal{O}(\varepsilon)$. We introduce the dimensionless variables:

$$x^* = \frac{x}{L}, \qquad u^* = \frac{u}{U}, \qquad w^* = \frac{w}{W}, \tag{2.15}$$

with the characteristic displacements U and W still unknown (to be determined further on). This transforms the domain of the central line of the beam to

$$\Omega := \{\underline{\boldsymbol{x}} \mid x \in (0, 1), y = z = 0\}. \tag{2.16}$$

After some algebraic manipulations, we arrive at the dimensionless version of Eq. 2.11 (unless stated otherwise we consider from now on only dimensionless quantities, and therefore the $*$ in the superscript is omitted)

$$\left(u_{,x} + \frac{1}{2}\left(\frac{W^2}{UL}\right)(w_{,x})^2\right)_{,x} = 0, \tag{2.17}$$

$$w_{,xxxx} + P^* w_{,xx} = q^*, \tag{2.18}$$

with

$$P^* := \frac{PL^2}{EI}, \qquad q^* := \frac{qL^4}{EIW}, \tag{2.19}$$

where P^* is assumed to be of $\mathcal{O}(1)$. We see that $q^* = 1$, if we choose $W = qL^4/EI$. Hence, the pre-assumption $W/R = \mathcal{O}(1)$ is satisfied if q is such that $qL^4/EIR = \mathcal{O}(1)$, which is true if we choose $W = R$. With choices $W = R$ and $U = R^2/L = \varepsilon R$, in conformity with the pre-assumption, we get for Eq. 2.17:

$$\left(u_{,x} + \frac{1}{2}(w_{,x})^2\right)_{,x} = 0. \tag{2.20}$$

NOTE, in Eq. 2.8 we assumed that $M_{,x}w_{,x} \ll N$ or P, which is true as

$$M_{,x}w_{,x} \sim EIw_{,xxx}w_{,x} \sim \frac{PL^2}{P^*}\frac{R^2}{L^4} \sim \frac{\varepsilon^2}{P^*}P \ll N.$$

Using these assumptions and omitting the $*$ in the superscript of P^* and q^* (given in Eq. 2.19)

results in the dimensionless strong form:

$$(\mathbf{S_d})\begin{cases}\text{Given constants } P, q,\\ \text{Find } (u,w)\in C^1(\Omega)\times C^4(\Omega),\ \text{such that,}\\ (u_{,x}+\dfrac{1}{2}w_{,x}^2)_{,x}=0,\\ w_{,xxxx}+Pw_{,xx}=q,\\ u|_{x=0}=w|_{\partial\Omega}=0,\\ (u_{,x}+\dfrac{1}{2}(w_{,x})^2)\Big|_{x=1}=-P,\quad w_{,xx}|_{\partial\Omega}=0.\end{cases} \tag{2.21}$$

2.4 Weak form

Derivation of the weak form is governed by multiplying the axial and transverse equilibrium equations with test functions possessing certain properties, and integrating them over the domain. Following the *Bubnov-Galerkin* approach we choose the same spaces for the test functions and the solutions. We define the following test/solution spaces

$$\begin{aligned}\mathcal{S}_u(\Omega) &:= \{u\in H^1(\Omega)\mid u|_{x=0}=0\},\\ \mathcal{S}_w(\Omega) &:= \{w\in H^2(\Omega)\mid w|_{\partial\Omega}=0\},\end{aligned} \tag{2.22}$$

and introduce $\psi=\psi(x)$, $\phi=\phi(x)$ as test functions and require $(\psi,\phi)\in\mathcal{S}_u(\Omega)\times\mathcal{S}_w(\Omega)$. The equilibrium equations are transformed to their weak form by multiplying them with the corresponding test functions, integrating them over the domain, and using integration by parts:

$$\begin{aligned}-\int_\Omega(u_{,x}+\frac{1}{2}w_{,x}^2)_{,x}\psi\mathrm{d}x+\Big[(u_{,x}+\frac{1}{2}w_{,x}^2+P)\psi\Big]_{x=1}&=\int_\Omega(u_{,x}+\frac{1}{2}w_{,x}^2)\psi_{,x}\mathrm{d}x+[P\psi]_{x=1}=0,\\ \int_\Omega(w_{,xxxx}+Pw_{,xx})\phi\mathrm{d}x=-[w_{,xx}\phi_{,x}]_{\partial\Omega}+\int_\Omega(w_{,xx}\phi_{,xx}-Pw_{,x}\phi_{,x})\mathrm{d}x&=\int_\Omega q\phi\mathrm{d}x,\end{aligned} \tag{2.23}$$

which should hold $\forall(\psi,\phi)\in\mathcal{S}_u(\Omega)\times\mathcal{S}_w(\Omega)$. Moreover we have $[w_{,xx}]_{\partial\Omega}=0$, such that the corresponding weak form is given by

$$(\mathbf{W})\begin{cases}\text{Given constants } P, q,\\ \text{Find } (u,w)\in\mathcal{S}_u(\Omega)\times\mathcal{S}_w(\Omega),\ \text{such that,}\\ \displaystyle\int_\Omega(u_{,x}+\frac{1}{2}w_{,x}^2)\psi_{,x}\mathrm{d}x=-\left[P\psi\right]_{x=1},\\ \displaystyle\int_\Omega(w_{,xx}\phi_{,xx})\mathrm{d}x=\int_\Omega(Pw_{,x}\phi_{,x}+q\phi)\mathrm{d}x,\\ \forall(\psi,\phi)\in\mathcal{S}_u(\Omega)\times\mathcal{S}_w(\Omega).\end{cases} \tag{2.24}$$

Besides starting from the equilibrium equations we could also use the energy of the system to obtain the weak form (**W**) [9].

2.5 Discretization

Discretization of the domain and displacement field is necessary to obtain an approximate solution using finite element technology. The domain is partitioned according to

$$\Omega = \bigcup_{e=1}^{N_e} \Omega^e, \tag{2.25}$$

with $\{\Omega^e\}_{e=1}^{N_e}$ the elements (Eq. 2.26), and N_e the number of elements.

$$\Omega^e := (x_1, x_2), \qquad e \in \{k \mid 1 \leq k \leq N_e\}. \tag{2.26}$$

Here x_1 and x_2 represent the first and second node of the element, respectively. In total we have $N := N_e + 1$ nodes in the partitioned domain. The shape functions are defined on the isoparametric domain

$$\mathcal{I} := [-1, 1]. \tag{2.27}$$

The mapping between the element domain and isoparametric domain is characterized by the bijection $\xi : \overline{\Omega}^e \to \mathcal{I}$, defined as

$$\xi(x) := \frac{2}{|\Omega^e|} x - \frac{x_1 + x_2}{|\Omega^e|}, \tag{2.28}$$

with $|\Omega^e| := x_2 - x_1$ the length of the element. The weak form (Eq. 2.24) demands C^0-continuity on ψ and u, and C^1-continuity on ϕ and w. Therefore we use different shape functions to interpolate the transverse displacement field, compared to the shape functions used to interpolate the axial displacement field. For notational convenience we use the same symbols for the test functions and shape functions, i.e. the test functions (ψ, ϕ) are turned into shape functions (ψ_i, ϕ_{ij}) in the next section.

2.5.1 Axial displacement field

Linear Lagrange polynomials are used to satisfy the C^0-continuity requirement on ψ and u. The linear Lagrange polynomials $\psi_i : \mathcal{I} \to \mathbb{R}$, $i \in \{1, 2\}$ are defined as

$$\underline{\boldsymbol{\psi}}^e(\xi) := \begin{bmatrix} \psi_1(\xi) \\ \psi_2(\xi) \end{bmatrix} := \frac{1}{2} \begin{bmatrix} 1 - \xi \\ 1 + \xi \end{bmatrix}. \tag{2.29}$$

At each finite element Ω^e the axial displacement u_e is approximated by u_e^h, given by

$$u_e(x) \approx u_e^h(x) = \sum_{i=1}^{2} \left((\psi_i u_i) \circ \xi \right)(x) = \langle (\underline{\boldsymbol{\psi}}^e \circ \xi)(x), \underline{\boldsymbol{u}}^e \rangle. \tag{2.30}$$

The unknowns u_i, $i \in \{1, 2\}$ are the approximate axial displacement values at nodes i of Ω^e, $\underline{\boldsymbol{u}}^e := (u_1, u_2)^T$, and $\langle \cdot, \cdot \rangle$ represents the Euclidean inner product. The total discretized axial displacement is obtained via $u^h(x) = \sum_{e=1}^{N_e} u_e^h(x)$.

2.5.2 Transverse displacement field

Different shape functions are necessary to satisfy the C^1-continuity requirement on ϕ and w. Cubic Hermite polynomials are used, which satisfy this demand. Besides the displacement field they also

interpolate the derivative of the displacement field $w_{,x}$. These shape functions $\phi_{ij} : \mathcal{I} \to \mathbb{R}$, $(i,j) \in \{1,2\} \times \{0,1\}$ are defined as

$$\begin{bmatrix} \phi_{10}(\xi) \\ \phi_{11}(\xi) \\ \phi_{20}(\xi) \\ \phi_{21}(\xi) \end{bmatrix} := \frac{1}{4} \begin{bmatrix} (\xi-1)^2(\xi+2) \\ (\xi-1)^2(\xi+1) \\ (\xi+1)^2(2-\xi) \\ (\xi+1)^2(\xi-1) \end{bmatrix}. \tag{2.31}$$

The ϕ_{10}, ϕ_{20} shape functions are used to interpolate the transverse displacement field. The ϕ_{11}, ϕ_{21} shape functions are used to interpolate the derivative of the transverse displacement field. Fig. 2.5a shows the four shape functions on $\mathcal{I}$, and Fig. 2.5b shows the derivatives of the four shape function on $\mathcal{I}$.

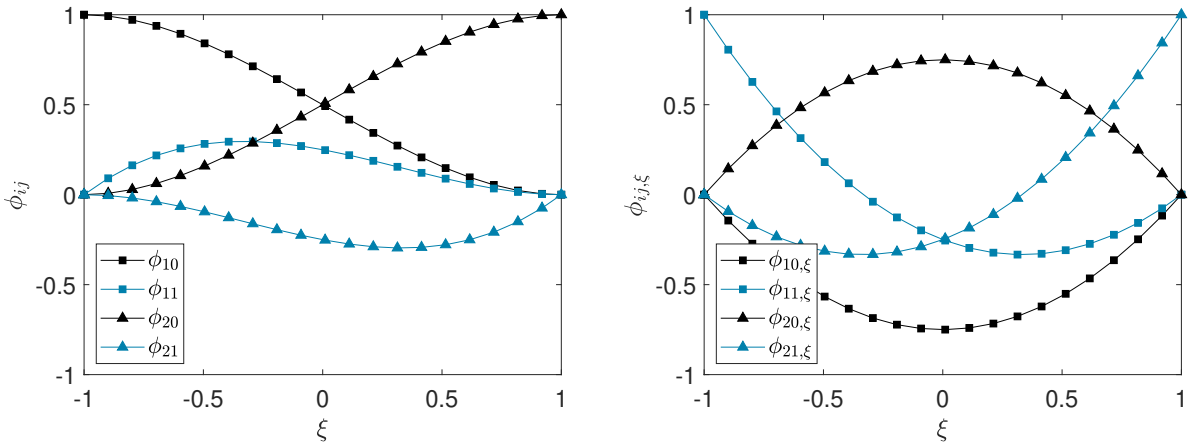

(a) ϕ_{10}, ϕ_{11}, ϕ_{20}, ϕ_{21} *on* $\mathcal{I}$. **(b)** $\phi_{10,\xi}$, $\phi_{11,\xi}$, $\phi_{20,\xi}$, $\phi_{21,\xi}$ *on* $\mathcal{I}$.

Figure 2.5: *Visualization of cubic Hermite polynomials and their derivatives on* $\mathcal{I}$.

Within each finite element Ω^e the transverse displacement field w_e is approximated by w_e^h, given by

$$w_e(x) \approx w_e^h(x) = \sum_{i=1}^{2} \left((\phi_{i0} w_i + \frac{|\Omega^e|}{2} \phi_{i1} w_{i,x}) \circ \xi \right)(x) = \langle (\underline{\boldsymbol{\phi}}^e \circ \xi)(x), \underline{\boldsymbol{d}}^e \rangle. \tag{2.32}$$

The unknowns w_i, $i \in \{1,2\}$ are the approximate transverse displacement values at node i of Ω^e. The unknowns $w_{i,x}$, $i \in \{1,2\}$ are the approximate derivatives of the transverse displacement values at node i of Ω^e. The vectors are defined as $\underline{\boldsymbol{\phi}}^e := (\phi_{10}, (|\Omega^e|/2)\phi_{11}, \phi_{20}, (|\Omega^e|/2)\phi_{21})^T$, and $\underline{\boldsymbol{d}}^e := (w_1, w_{1,x}, w_2, w_{2,x})^T$. The total discretized transverse displacement is obtained via $w^h(x) = \sum_{e=1}^{N_e} w_e^h(x)$.

Combining these discretized approximations with the weak form, we obtain the following vectors:

$$\begin{aligned}
\underline{\boldsymbol{f}}^e_{in1} &:= \int_{\Omega^e} \left(u^h_{e,x} + \frac{1}{2} w^2_{e,x} \right) \underline{\boldsymbol{\psi}}^e_{,x} \mathrm{d}x, \\
\underline{\boldsymbol{f}}^e_{in2} &:= \int_{\Omega^e} w^h_{e,xx} \underline{\boldsymbol{\phi}}^e_{,xx} \mathrm{d}x, \\
\underline{\boldsymbol{f}}^e_{ex1} &:= \begin{cases} \underline{\mathbf{0}}_2 & \text{if } e \in \{1,2,...,N_e-1\}, \\ (0,-P)^T & \text{if } e = N_e, \end{cases} \\
\underline{\boldsymbol{f}}^e_{ex2} &:= \int_{\Omega^e} (P w_{e,x} \underline{\boldsymbol{\phi}}^e_{,x} + q \underline{\boldsymbol{\phi}}^e) \mathrm{d}x,
\end{aligned} \tag{2.33}$$

with $\underline{\mathbf{0}}_d \in \mathbb{R}^d$ the zero vector. Moreover we have $\underline{\boldsymbol{f}}^e_{in1} \in \mathbb{R}^2$, $\underline{\boldsymbol{f}}^e_{ex1} \in \mathbb{R}^2$, $\underline{\boldsymbol{f}}^e_{in2} \in \mathbb{R}^4$, and $\underline{\boldsymbol{f}}^e_{ex2} \in \mathbb{R}^4$. The solution vector at element level is defined as $\underline{\boldsymbol{\Upsilon}}^e := (u_1, u_2, w_1, w_{1,x}, w_2, w_{2,x})^T \in \mathbb{R}^6$. The total system is obtained by using the assembly operator

$$\underline{\boldsymbol{f}}_{in} = \mathop{\mathrm{A}}_{e=1}^{N_e} \begin{bmatrix} \underline{\boldsymbol{f}}^e_{in1} \\ \underline{\boldsymbol{f}}^e_{in2} \end{bmatrix}, \qquad \underline{\boldsymbol{f}}_{ex} = \mathop{\mathrm{A}}_{e=1}^{N_e} \begin{bmatrix} \underline{\boldsymbol{f}}^e_{ex1} \\ \underline{\boldsymbol{f}}^e_{ex2} \end{bmatrix}. \tag{2.34}$$

After reordering we obtain the following non-linear system:

$$\underline{\boldsymbol{f}}_{in}(\underline{\boldsymbol{\Upsilon}}) = \underline{\boldsymbol{f}}_{ex}(\underline{\boldsymbol{\Upsilon}}), \tag{2.35}$$

that we have to solve for the nodal solution vector

$$\underline{\boldsymbol{\Upsilon}} = (\underline{\boldsymbol{u}}, \underline{\boldsymbol{w}}, \underline{\boldsymbol{w}}_{,x})^T = (u_1, u_2, ..., u_N, w_1, w_2, ..., w_N, w_{1,x}, w_{2,x}, ..., w_{N,x})^T, \tag{2.36}$$

with $\underline{\boldsymbol{f}}_{in} \in \mathbb{R}^{3N}$, $\underline{\boldsymbol{f}}_{ex} \in \mathbb{R}^{3N}$, $\underline{\boldsymbol{\Upsilon}} \in \mathbb{R}^{3N}$. *NOTE*, this nodal solution vector and therefore the discretized solutions $(u^h, w^h) \notin \mathcal{S}_u(\Omega) \times \mathcal{S}_w(\Omega)$, because they do not satisfy the boundary conditions. We define $\mathcal{S}^h_u(\Omega) \subset \mathcal{S}_u(\Omega)$ and $\mathcal{S}^h_w(\Omega) \subset \mathcal{S}_w(\Omega)$ as the span of all the globally defined shape functions, without the span of the global shape functions corresponding to the boundary conditions. Details on the definition of the global shape functions and discrete solution spaces is given in App. A. The set of equations corresponding to the nodal values u_1, w_1 and w_N is removed[1] from the full non-linear system resulting in a system of dimension $3N - 3$:

$$\begin{aligned} \tilde{\underline{\boldsymbol{u}}} &= (u_2, u_3, ..., u_N)^T, \\ \tilde{\underline{\boldsymbol{w}}} &= (w_2, w_3, ..., w_{N-1})^T, \\ \tilde{\underline{\boldsymbol{w}}}_{,x} &= (w_{1,x}, w_{2,x}, ..., w_{N,x})^T, \\ \tilde{\underline{\boldsymbol{\Upsilon}}} &= \begin{bmatrix} \tilde{\underline{\boldsymbol{u}}} \\ \tilde{\underline{\boldsymbol{w}}} \\ \tilde{\underline{\boldsymbol{w}}}_{,x} \end{bmatrix}, \end{aligned} \tag{2.37}$$

with $\tilde{\underline{\boldsymbol{u}}} \in \mathbb{R}^r$, $\tilde{\underline{\boldsymbol{w}}} \in \mathbb{R}^m$ and $\tilde{\underline{\boldsymbol{w}}}_{,x} \in \mathbb{R}^n$, and $r = N - 1$, $m = N - 2$, and $n = N$. From now on we omit the $\sim$ and only consider the system of dimension $r + m + n$.

2.6 Numerical Implementation

The system of equations is solved incrementally, and per increment it is solved using an iterative method. In particular Newton's method and the arc-length method are used as iterative methods.

2.6.1 Newton's method

The non-linear system is solved incrementally:

$$\underline{\boldsymbol{f}}_{in}(\underline{\boldsymbol{\Upsilon}}) = \Lambda^{(t)} \underline{\boldsymbol{f}}_{ex}(\underline{\boldsymbol{\Upsilon}}), \tag{2.38}$$

for the solution vector $\underline{\boldsymbol{\Upsilon}}$ per increment t. The incremental parameter $\Lambda^{(t)} \in [0, 1]$ is updated according to

$$\Lambda^{(t+1)} = \Lambda^{(t)} + \Delta\Lambda, \tag{2.39}$$

[1] Due to homogeneous boundary conditions we are allowed to simply remove these equations.

with $\Lambda^{(0)} = 0$, and $\Delta\Lambda$ a chosen incremental update. Newton's iterative method is used per increment to calculate the solution. For Newton's method we define the residual vector as

$$\underline{\boldsymbol{R}}(\underline{\boldsymbol{\Upsilon}}) := \underline{\boldsymbol{f}}_{in}(\underline{\boldsymbol{\Upsilon}}) - \underline{\boldsymbol{f}}_{ex}(\underline{\boldsymbol{\Upsilon}}), \tag{2.40}$$

and the tangent stiffness matrix as

$$\underline{\underline{\boldsymbol{T}}}(\underline{\boldsymbol{\Upsilon}}) := \frac{\partial \underline{\boldsymbol{R}}(\underline{\boldsymbol{\Upsilon}})}{\partial \underline{\boldsymbol{\Upsilon}}}. \tag{2.41}$$

Newton's iterative procedure is given by

$$\begin{aligned} \underline{\underline{\boldsymbol{T}}}_k \Delta\underline{\boldsymbol{\Upsilon}} &= -\underline{\boldsymbol{R}}_k, \\ \underline{\boldsymbol{\Upsilon}}_{k+1} &= \underline{\boldsymbol{\Upsilon}}_k + \Delta\underline{\boldsymbol{\Upsilon}}, \end{aligned} \tag{2.42}$$

where the abbreviations $\underline{\underline{\boldsymbol{T}}}_k = \underline{\underline{\boldsymbol{T}}}(\underline{\boldsymbol{\Upsilon}}_k)$ and $\underline{\boldsymbol{R}}_k = \underline{\boldsymbol{R}}(\underline{\boldsymbol{\Upsilon}}_k)$ are used, and $k \in \mathbb{N}$ an iterative counter. We say that Newton's method has converged if

$$\|\underline{\boldsymbol{R}}_k\|_2 \leq \epsilon, \tag{2.43}$$

with ϵ a chosen small parameter, and $\|\cdot\|_2$ the standard 2-norm on $\mathbb{R}^d$. In Sec. 3 we investigate buckling using eigenvalue analysis techniques. These eigenvalue analysis techniques are performed on the tangent stiffness matrix $\underline{\underline{\boldsymbol{T}}}$. We use

$$\underline{\underline{\boldsymbol{T}}} = \underline{\underline{\boldsymbol{T}}}_0 - \underline{\underline{\boldsymbol{T}}}_g(P), \tag{2.44}$$

where $\underline{\underline{\boldsymbol{T}}}_0$ correlates with the terms of Eq. 2.33 independent of P, and $\underline{\underline{\boldsymbol{T}}}_g(P)$ correlates with the part of $\underline{\boldsymbol{f}}^e_{ex2}$ depending on P. The term $\underline{\boldsymbol{f}}^e_{ex1}$ also depends on P, but is independent of u^h_e and w^h_e, resulting in no contribution to the tangent stiffness matrix. In Sec. 3 we use Eq. 2.44, which allows us to determine the critical load at which buckling occurs via an eigenvalue analysis.
During several simulations throughout this report we encounter buckling. In a few of these simulations we follow a part of the post-buckling solution path. Newton's method is not able to follow the correct solution path after passing the point at which buckling occurs. Therefore the arc-length method is implemented, which is able to follow the correct solution path. For details on the arc-length method we refer to App. B.

2.6.2 Numerical integration

Numerical integration is achieved using a certain quadrature rule. Here the Gauss-Legendre quadrature rule is used. For any $f : \mathcal{I} \to \mathbb{R}$ this rule is given by

$$\int_{\mathcal{I}} f(\xi)\mathrm{d}\xi \approx \sum_{i=1}^{N_{gauss}} \omega_i f(\xi_i), \tag{2.45}$$

with N_{gauss} the number of Gauss points, $\{\omega_i\}_{i=1}^{N_{gauss}}$ the weights and $\{\xi_i\}_{i=1}^{N_{gauss}}$ the points of integration. The Gauss-Legendre quadrature rule is exact if the function $f(x)$ in Eq. 2.45 is a polynomial of degree $2N_{gauss} - 1$ or less. The shape functions that are used in the discretized weak form are polynomials and therefore exact integration is possible using this Gauss-Legendre quadrature rule. Applying the Gauss-Legendre quadrature rule to the vectors given in Eq. 2.33 results in

$$\int_{\mathcal{I}} (\cdot)\frac{|\Omega^e|}{2}\mathrm{d}\xi \approx \sum_{i=1}^{N_{gauss}} (\cdot)_{x=x(\xi_i)}\omega_i\frac{|\Omega^e|}{2}, \tag{2.46}$$

where $(\cdot)$ corresponds to the integrands of the element vectors, and the factor $|\Omega^e|/2$ is a result of changing the domain of integration. The highest polynomial degree present in our model is three, coming from the cubic Hermite polynomial shape functions. For exact integration it suffices to use 2 Gauss points, which is used throughout the rest of the report, unless stated otherwise.

2.7 Validation

The numerical approach of the previous sections for the beam model presented in Sec. 2 is implemented in MATLAB, and validated here through a mesh convergence study and a comparison with Marc & Mentat[1]. Besides a compressive (dimensionless) axial force P, the beam is loaded by a constant transverse load q, inducing an initial (before buckling) deflection of the beam. This transverse displacement is necessary to discard the initial undeformed configuration as possible solution, and it is used to trigger buckling. Including this transverse load q mollifies the pure buckling concept, in so far that, although it resembles a buckling process, no sharp buckling is observed. The finite element solution is validated through a mesh convergence study by comparison with an analytical solution for the deflection w, which is valid in the pre-buckling regime. For convenience, we neglect the axial displacement ($u = 0$). Hence, the mesh convergence study is fully based on the transverse displacement field $w(x)$. As we consider the pre-buckling regime and because the Euler buckling force is at $P = P_{cr} = \pi^2$, we take $P \in [0, \pi^2)$. An unique analytical solution for $w(x)$ exists according to Kundu & Ganguli [10], and Komkov [11], and is given by

$$w^{an}(x) = \frac{q}{2P^2}\left(Px^2 - Px + 2\cos(\sqrt{P}x) - 2\frac{\sin(\sqrt{P}x)}{\tan(\sqrt{P})} + 2\frac{\sin(\sqrt{P}x)}{\sin(\sqrt{P})} - 2\right). \tag{2.47}$$

The parameters for the mesh convergence study are $q = 0.01$, $P = 8$ and 1 increment is used. For the mesh convergence study we use the L^2-error estimate[2] $\|w^h - w^{an}\|_{L^2(\Omega)}$, with $w^h(x)$ the finite element solution and $w^{an}(x)$ the analytical solution. The error vs the amount of elements is depicted in Fig. 2.6a.

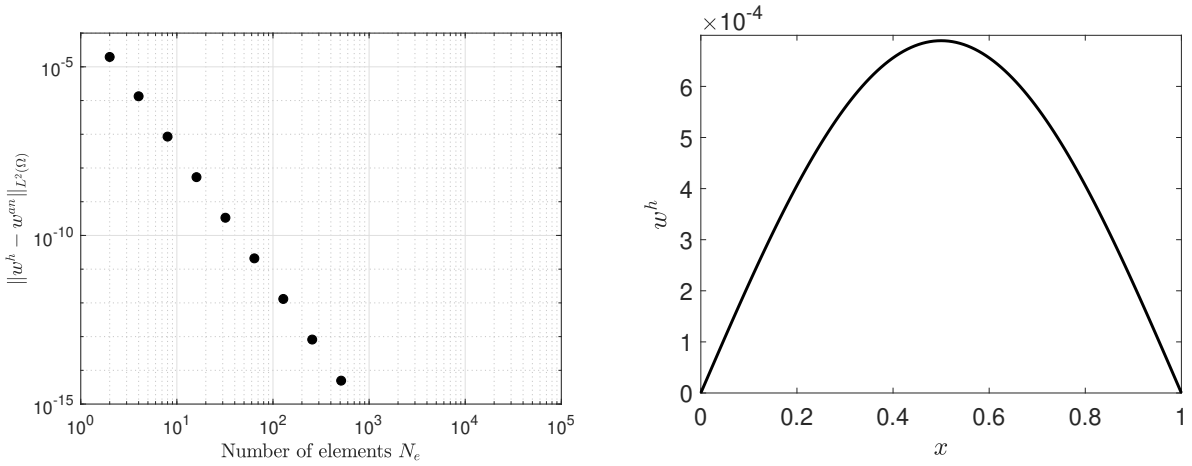

(a) *Error vs number of elements.* **(b)** *Corresponding deformed configuration for $N_e = 128$.*

Figure 2.6: *Validation of our model through mesh convergence study and an example of the deformed configuration.*

[1] Marc & Mentat is a commercially available finite element package. Comparing our model with Marc & Mentat does not prove that our model is correct, but it gives a certain validation.

[2] On $\mathbb{R}^d$ all norms are equivalent. The L^2-norm itself is independent of N_e, and therefore chosen here.

Fig. 2.6a shows that increasing one decade on the horizontal axis corresponds approximately to decreasing four decades on the vertical axis, i.e. $\|w^h - w^{an}\|_{L^2(\Omega)} \propto (1/N_e)^4$, which corresponds to the a priori error estimate of Ganesan and Tobiska [12]. Increasing the amount of elements even more is useless because of computer precision ($1 \cdot 10^{-16}$). Fig. 2.6b shows the corresponding deformed configuration for $N_e = 128$. The transverse displacement is small compared to unity since we only consider the pre-buckling regime. The deformed shape visible in Fig. 2.6b is due to the applied transverse load q, which is used to initiate buckling. This result validates that the finite element model is implemented correctly.
Validity of our computations for (a restricted part of) the post-buckling regime is achieved by comparison with Marc & Mentat. The parameters used during these simulations are given by $P = \Lambda P_0$, with $P_0 = 12$, $q = 0.1$, $N_e = 100$ and $\epsilon = 1 \cdot 10^{-8}$, with ϵ the error used for Newton's method and the arc-length method. During the comparison with Marc & Mentat we use different values of q, to see the influence of the initial deflection on the post-buckling regime. To be able to follow the correct solution path in the post-buckling regime, we have to use the arc-length method as Newton's method is not able to follow the correct solution path. The reason for this is elaborated in more detail further on in Sec. 3.1. *Von-Kármán* strains are used in our model, which account for moderately large rotations, but neglect large deformations. Fig. 2.7 shows the comparison of our model with the model of Marc & Mentat, for different values of q. Fig. 2.7a shows the load parameter $\Lambda = P/P_0$ vs the maximum transverse displacement w^h_{max}. In Fig. 2.7b a close-up around the transition from the pre-buckling regime to the post-buckling regime of Fig. 2.7a is given. Fig. 2.7c shows the deformed configurations from our (MATLAB) model for $q = 1 \cdot 10^{-2}$ and $q = 1$ at different incremental values.

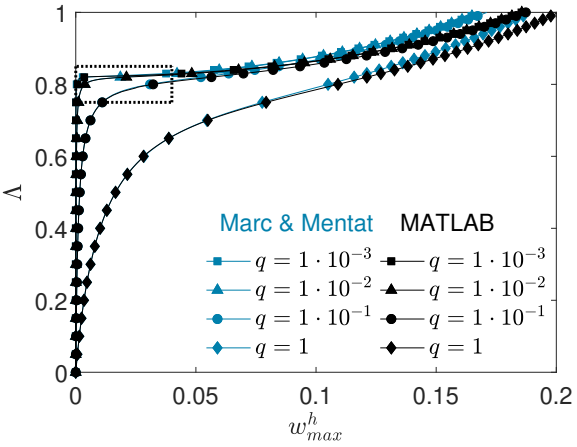

(a) *Load factor Λ vs w^h_{max} using Marc & Mentat, and MATLAB.*

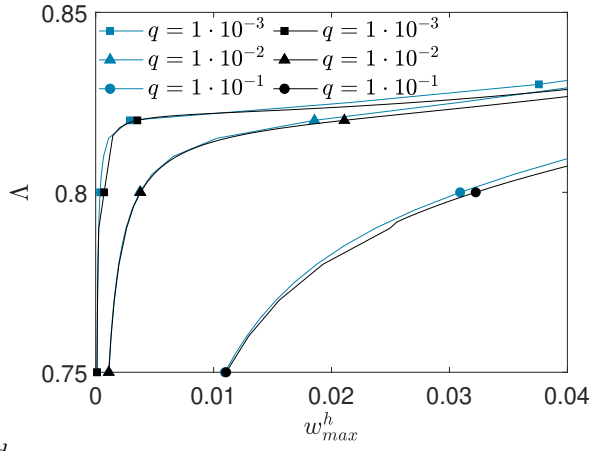

(b) *Close-up of marked rectangle of Fig. 2.7a.*

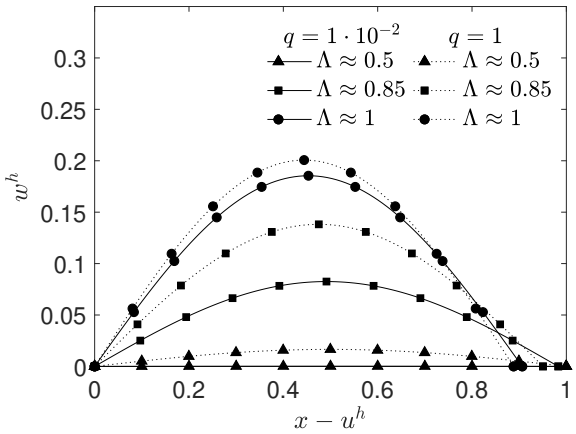

(c) *Illustration of deformed configurations from our model, for $q = 1 \cdot 10^{-2}$ and $q = 1$, for different values of Λ.*

Figure 2.7: *Validation of our (MATLAB) model through comparison of w^h_{max} vs Λ with results from Marc & Mentat, for different values of q.*

The results in Fig. 2.7a show that our model and the Marc & Mentat model are equivalent for small deformations. When deformations become too large our solutions start to deviate from those of Marc & Mentat. In Marc & Mentat the option "large deformations" is used, which probably distinguishes between the initial and deformed configuration. Our model does not do this, which is the reason for the deviation between our results and those of Marc & Mentat. We see that increasing the load q, i.e. making the initial deformation larger, mollifies the buckling behaviour. The results of Fig. 2.7 show that we are able to perform a post-buckling simulation with an initial disturbance, which is the same type of simulation Océ-Technologies B.V. currently uses to model the cockling process of a paper sheet. However, we are interested in modeling buckling without an initial disturbance since the deformed configuration depends on the choice of the initial disturbance. The limiting case $q \to 0$ corresponds to a pure buckling simulation (i.e. no initial disturbance), with a critical (Euler buckling) load parameter $\pi^2/12 \approx 0.82$, see Fig. 2.7b. Taking $q = 0$, corresponding to the pure Euler buckling case, yields here only the trivial solution $w = 0$. A non-trivial solution for the pure buckling case may be found by an eigenvalue analysis as will be discussed in the next section.

3 Buckling & contact

The finite element beam model derived and validated in Sec. 2 is used to investigate the buckling and contact phenomena. Eigenvalue analysis is used to model pure buckling, where the term pure refers to a simulation without any initial disturbance. For our model this corresponds to omission of the transverse load ($q = 0$). This eigenvalue analysis results in an eigenpair representing the critical buckling load and corresponding buckling pattern. Furthermore, a small part of the post-buckling regime is evaluated using the arc-length method.
Contact is non-linear, because the contact area is initially unknown, and can numerically be incorporated using different techniques [13, 14]. We incorporate contact conditions by means of a penalty method [13, 14].
Buckling and contact are eventually combined together and investigated via a so-called cone constrained eigenvalue analysis.

3.1 Buckling

Buckling occurs in general when a small change to a certain parameter results in a large quantitative change of the system. For the considered pinned-hinged beam this corresponds to transverse bending if the load parameter Λ is increased above a certain critical value. Assuming we are located on the solution path, we have a solution $\underline{\boldsymbol{\Upsilon}}$, just before the bifurcation point, that satisfies $\underline{\boldsymbol{R}}(\underline{\boldsymbol{\Upsilon}}) = \underline{\mathbf{0}}$. Surpassing the bifurcation point should result in transverse bending, with origination of bending in the bifurcation point. We assume there exists a non-zero update $\Delta\underline{\boldsymbol{\Upsilon}}$, such that $\underline{\boldsymbol{\Upsilon}} + \Delta\underline{\boldsymbol{\Upsilon}}$ is the solution in the bifurcation point, yielding $\underline{\boldsymbol{R}}(\underline{\boldsymbol{\Upsilon}} + \Delta\underline{\boldsymbol{\Upsilon}}) = \underline{\mathbf{0}}$. We approximate

$$\underline{\boldsymbol{R}}(\underline{\boldsymbol{\Upsilon}} + \Delta\underline{\boldsymbol{\Upsilon}}) \approx \underline{\boldsymbol{R}}(\underline{\boldsymbol{\Upsilon}}) + \underline{\underline{\boldsymbol{T}}}\Delta\underline{\boldsymbol{\Upsilon}} \qquad \Rightarrow \qquad \underline{\underline{\boldsymbol{T}}}\Delta\underline{\boldsymbol{\Upsilon}} = \underline{\mathbf{0}}, \qquad \text{with } \Delta\underline{\boldsymbol{\Upsilon}} \neq \underline{\mathbf{0}}, \tag{3.1}$$

with $\underline{\underline{\boldsymbol{T}}}$ the tangent stiffness matrix from Eq. 2.41 (For readability we omit the iteration and incremental counters). Using Eq. 2.44, we have

$$\underline{\underline{\boldsymbol{T}}}\Delta\underline{\boldsymbol{\Upsilon}} = (\underline{\underline{\boldsymbol{T}}}_0 - \underline{\underline{\boldsymbol{T}}}_g(P))\Delta\underline{\boldsymbol{\Upsilon}} = \underline{\mathbf{0}}, \qquad \Delta\underline{\boldsymbol{\Upsilon}} \neq \underline{\mathbf{0}}. \tag{3.2}$$

In general we increase the applied load P incrementally using $P = \Lambda P_0$ with $\Lambda \in [0, 1]$ the load parameter. We are interested in the critical load parameter Λ at which buckling occurs. Moreover, the matrix $\underline{\underline{\boldsymbol{T}}}_g(P)$ is linear in P (see Eq. 2.33), implying that

$$\begin{aligned} (\underline{\underline{\boldsymbol{T}}}_0 - \underline{\underline{\boldsymbol{T}}}_g(\Lambda P_0))\Delta\underline{\boldsymbol{\Upsilon}} = 0, \qquad \Delta\underline{\boldsymbol{\Upsilon}} \neq \underline{\mathbf{0}}, \\ (\underline{\underline{\boldsymbol{T}}}_0 - \Lambda\underline{\underline{\boldsymbol{T}}}_g(P_0))\Delta\underline{\boldsymbol{\Upsilon}} = 0, \qquad \Delta\underline{\boldsymbol{\Upsilon}} \neq \underline{\mathbf{0}}. \end{aligned} \tag{3.3}$$

Instead of increasing the load parameter in Eq. 3.3, we consider the load parameter as an unknown too, turning Eq. 3.3 into an eigenvalue problem. For notational convenience we use

$$(T_0 - \lambda\underline{\underline{\boldsymbol{T}}}_g)\Delta\underline{\boldsymbol{\Upsilon}} \neq \underline{\mathbf{0}}, \qquad \Delta\underline{\boldsymbol{\Upsilon}} \neq \underline{\mathbf{0}}, \tag{3.4}$$

with λ the critical load parameter at which buckling occurs (eigenvalue), and $\underline{\underline{\boldsymbol{T}}}_g = \underline{\underline{\boldsymbol{T}}}_g(P_0)$.
Considering Eq. 3.4 as an eigenvalue problem allows us to solve for the eigenpair $(\Delta\underline{\boldsymbol{\Upsilon}}, \lambda)$, with λ the eigenvalue corresponding to the critical load parameter at which buckling occurs, and $\Delta\underline{\boldsymbol{\Upsilon}}$ the eigenvector which represents the buckled deformed configuration. Eq. 3.4 has no unique solution because an eigenvector is determined up to a scaling constant, and a system of equations consists of multiple eigenpairs $(\Delta\underline{\boldsymbol{\Upsilon}}, \lambda)$ that satisfy Eq. 3.4. However, in reality buckling occurs at the lowest eigenvalue, and the buckled shape is the corresponding eigenvector. For convenience we refer to

λ_c as the lowest eigenvalue or **c**ritical value at which buckling occurs.

Eq. 3.4 is solved at the first increment to determine the critical eigenpair $(\lambda_c, \Delta\underline{\boldsymbol{\Upsilon}})$. There is no displacement in the pre-buckling phase, and therefore it is not necessary to do an eigenvalue analysis at any successive increment. After obtaining $(\lambda_c, \Delta\underline{\boldsymbol{\Upsilon}})$ at the first increment in the pre-buckling phase we increase the load parameter, and check if $\Lambda > \lambda_c$. If this condition is satisfied buckling occurs and the eigenvector $\Delta\underline{\boldsymbol{\Upsilon}}$ is used as input for the post-buckling process, i.e. solving $\underline{\underline{\boldsymbol{T}}}\Delta\underline{\boldsymbol{\Upsilon}} = -\underline{\boldsymbol{R}}$ incrementally after surpassing the bifurcation point. MATLAB returns eigenvectors with Euclidean norm 1. Because the eigenvector is determined up to a scaling constant we multiply it with a small constant to make sure it is small compared to unity resulting in a smooth transition to the post-buckling regime. The transition from the pre-buckling regime to the post-buckling regime corresponds numerically to a sign change of the determinant of the tangent stiffness matrix $\underline{\underline{\boldsymbol{T}}}$, where the exact bifurcation point corresponds to a zero determinant of the tangent stiffness matrix $\underline{\underline{\boldsymbol{T}}}$. Newton's method is not able to follow the correct solution path. The arc-length method considers the load parameter as unknown variable too, which makes it possible to switch sign of the load parameter, resulting in a physical possible solution path. For this reason the arc-length method is used in the post-buckling regime. For more details on the arc-length method we refer to App. B. The eigenvalue analysis is performed on the axially loaded beam, where the transverse load q is omitted, i.e. a pure buckling simulation. The parameters used during the simulation are given by $P_0 = 12$, $P = \Lambda P_0$, $N_e = 100$, and $\epsilon = 1 \cdot 10^{-8}$ as convergence criteria. The load vs the transverse displacement curve resulting from the post-buckling simulation is shown in Fig. 3.1a. The eigenvalue analysis is used to determine the critical load parameter and corresponding buckling pattern. An example of the deformed configuration for the positive load displacement curve is shown in Fig. 3.1b.

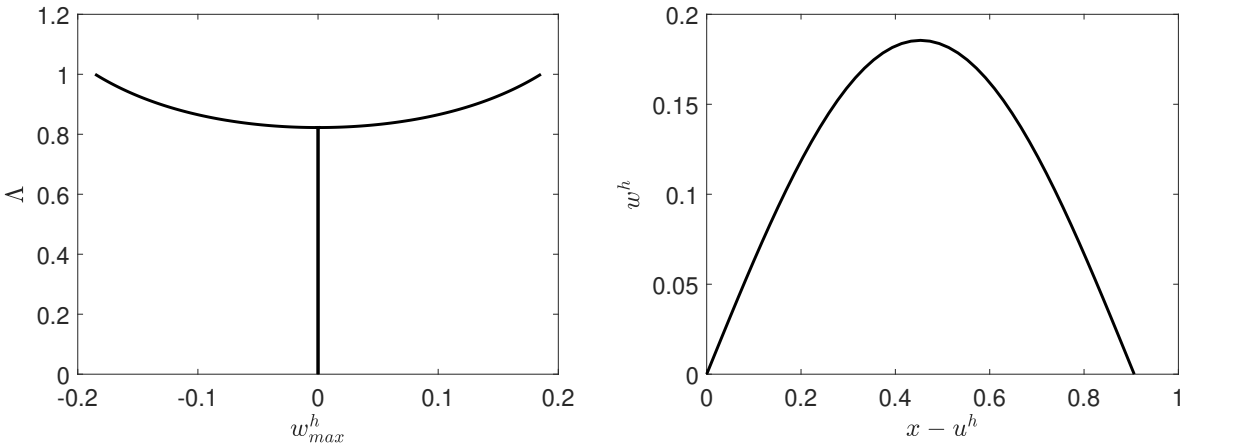

(a) *Load displacement curve.*

(b) *Illustration of deformed configuration, corresponding to positive load displacement curve.*

Figure 3.1: *Bifurcation diagram and corresponding deformed configuration.*

During a post-buckling simulation in combination with an eigenvalue analysis there is no preferred direction for buckling, i.e. the resulting eigenvector can either be $\Delta\underline{\boldsymbol{\Upsilon}}$ or $-\Delta\underline{\boldsymbol{\Upsilon}}$. Therefore, both solution paths are shown in Fig. 3.1. Comparing Fig. 3.1a with Fig. 2.7a, we see that the eigenvalue analysis is the limiting case of the beam including an initial transverse displacement, i.e. $q \to 0$. We observe that the axial and transverse displacement fields are zero in the pre-buckling regime. This implies that the tangent stiffnes matrix is constant in the pre-buckling regime, and that it suffices to perform the eigenvalue analysis in the first increment instead of an increment close to

the bifurcation point. Moreover, buckling is fully governed by the transverse equilibrium equation, implying that the eigenvalue analysis can be performed on the discretized transverse equilibrium equation only, which is a system of dimension $m + n$, instead of $r + m + n$. Further on in Sec. 3.3 we use this system of dimension $m + n$, and the property that the tangent stiffness matrix is constant in the pre-buckling regime.

The current simulations at Océ-Technologies B.V. use a small initial random displacement to induce buckling. We use the beam model to see the influence of this random initial transverse displacement on the buckling behaviour. Moreover, we compare it with the result from an eigenvalue analysis. A small initial displacement w_{in} is added to right-hand side of the strong form ($\mathbf{S_d}$) as $w_{in,xxxx}$ [15]. This results in an additional term to $\underline{\boldsymbol{f}}^e_{ex2}$ of Eq. 2.33, i.e.

$$\underline{\boldsymbol{f}}^e_{ex2} = \int_{\Omega^e} (P w_{e,x} \underline{\boldsymbol{\phi}}^e_{,x} + q \underline{\boldsymbol{\phi}}^e) \mathrm{d}x + \int_{\Omega^e} \langle \underline{\boldsymbol{\phi}}^e_{,xx}, \underline{\boldsymbol{d}}^e_0 \rangle \underline{\boldsymbol{\phi}}^e_{,xx} \mathrm{d}x, \tag{3.5}$$

with the initial displacement vector $\underline{\boldsymbol{d}}^e_0$ for a finite element defined as $\underline{\boldsymbol{d}}^e_0 := (w_{in1}, w_{in1,x}, w_{in2}, w_{in2,x})^T$. To mimic the current simulations at Océ-Technologies B.V. we pick a random value in the interval $[-0.001, 0.001]$, and assign it to each entry of $\underline{\boldsymbol{d}}^e_0$, for all elements.
The term "random beam" is used for a beam with a small initial random transverse displacement. We again use $P_0 = 12$, $P = \Lambda P_0$, $N_e = 100$, and $\epsilon = 1 \cdot 10^{-8}$ as convergence criteria. The load vs maximum transverse displacement curves of ten random beams are compared with the result from the eigenvalue analysis, see Fig. 3.2.

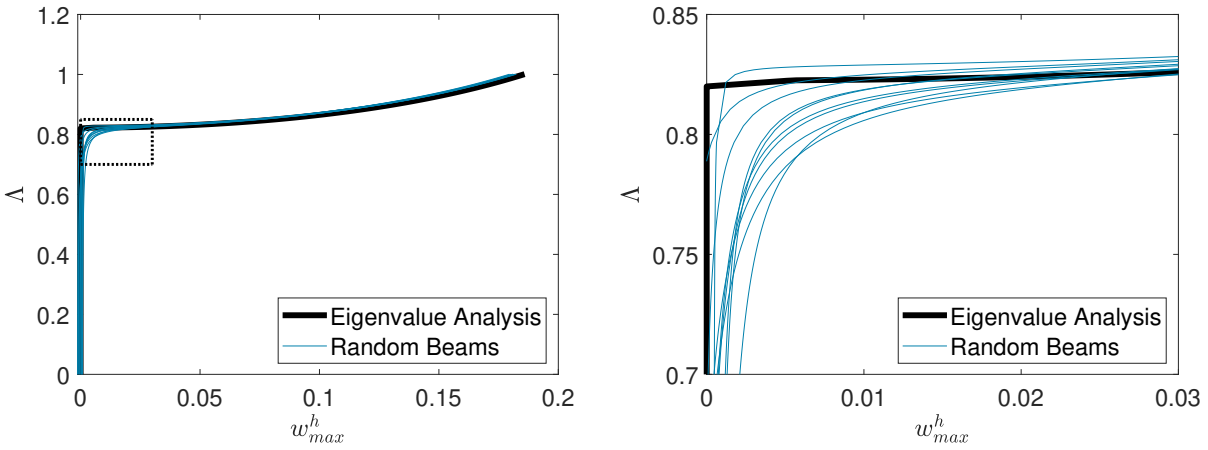

(a) *Load vs maximum transverse displacement.* **(b)** *Close-up of marked rectangle of Fig. 3.2a.*

Figure 3.2: *Comparison of eigenvalue analysis and ten random beams using post-buckling simulation.*

Fig. 3.2a shows the load parameter vs the maximum transverse displacement for ten random beams, and for the eigenvalue analysis. Fig. 3.2a shows that the result from the eigenvalue analysis is similar compared to the ten random beams. The same holds for the critical load parameter λ_c at which buckling occurs. Fig. 3.2b shows a close-up of the *bifurcation* point, and we observe that λ_c for the eigenvalue analysis is similar to the load parameter at which buckling occurs for the ten random beams. An eigenvalue analysis on the perfect beam has multiple advantages compared to a "random beam". Consider first of all the critical buckling parameter λ_c. The theoretical buckling load is located at the Euler buckling load $\Lambda = \pi^2/12 \approx 0.82$. The close-up shows that the critical load parameter λ_c is different for different random beams, i.e. they fluctuate around the critical Euler buckling load parameter. Using eigenvalue analysis we obtain the critical buckling

load parameter $\pi^2/12$. This shows that an eigenvalue analysis is capable of determining the critical load parameter similar to the critical load parameter of random beams. In reality beams are not perfect, and this example shows that an eigenvalue analysis is able to determine the critical load parameter at which a random beam buckles. A pitfall using random beams is their discontinuous gradient. Numerical issues might occur due to these discontinuous gradients. Moreover, if the interval of the random values $[-0.001, 0.001]$ is enlarged to $[-0.01, 0.01]$, we obtain no convergence for some random beams. This convergence issue was also obtained by Océ-Technologies B.V. in their post-buckling simulations for some random small initial out-of-plane configurations of the paper sheet.
If we are only interested in the critical load parameter λ_c and corresponding buckling pattern we only have to perform an eigenvalue analysis, instead of a incremental post-buckling simulation. Considering simulation time we observe for our results of Fig. 3.2 that an eigenvalue analysis is more than ten times faster compared to a post-buckling simulation.
We have shown that eigenvalue analysis offers perspective for a buckling problem. Performing an eigenvalue analysis results in the critical load parameter λ_c and in the corresponding buckling pattern. Moreover, it is a fast and robust method compared to post-buckling simulations using random beams.

3.2 Contact

During the printing process the sheet of paper is laying on a printing table, i.e. in contact with a rigid foundation. The two-dimensional model in Marc & Mentat contains these contact conditions. In this section we examine how contact is implemented numerically, and how it influences the eigenvalue analysis from the buckling simulation. Both the theory and numerical examples are based on the one-dimensional beam model from Sec. 2.

3.2.1 Theory

Implementation of contact conditions can be done using several techniques [13]. We choose the penalty method as this is the most widely used method to implement contact conditions [14]. The basis for any contact method is a so called gap function $g : \mathbb{R} \to \mathbb{R}$. This gap function measures the distance between two bodies that might be in contact and is defined for our model as

$$(g \circ w)(x) = h(x) - W(x) = h(x) + w(x) \geq 0, \tag{3.6}$$

with $h : \Omega \to \mathbb{R}$ the distance (height) between the initial undeformed configuration and the rigid foundation, $w : \Omega \to \mathbb{R}$ the transverse displacement, and $W(x) = -w(x)$ the deflection in negative $z-$direction, see Fig. 3.3.

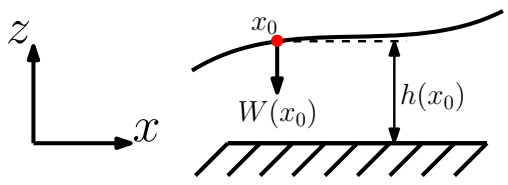

Figure 3.3: *Illustration of distance function $h(x)$, and $W(x)$ $(= -w(x))$ at a certain point $x = x_0$, on a part of a one-dimensional object*

For convenience we write from now on $g(w) = (g \circ w)(x)$.
In case of contact $(g(w) = 0)$ a reaction force $R(w) \geq 0$ appears. If there is no contact $(g(w) > 0)$,

there is no reaction force ($R(w) = 0$). Therefore we have

$$g(w) \geq 0, \qquad R(w) \geq 0, \qquad g(w)R(w) = 0, \tag{3.7}$$

which are known as the *Hertz-Signorini-Moreau* conditions [14]. In optimization these conditions are known as the *Karush-Kuhn-Tucker* conditions [13]. Adding contact conditions to the strong form results in

$$(\mathbf{S_c}) \begin{cases} \text{Given constants } P, q, \epsilon_p, \text{ and } h(x), \\ \text{find } (u, w) \in C^1(\Omega) \times C^4(\Omega), \text{ such that,} \\ (u_{,x} + \dfrac{1}{2} w_{,x}^2)_{,x} = 0, \\ w_{,xxxx} + P w_{,xx} = q + R(w), \\ u|_{x=0} = w|_{\partial\Omega} = 0, \\ (u_{,x} + \dfrac{1}{2}(w_{,x})^2)\Big|_{x=1} = -P, \quad w_{,xx}|_{\partial\Omega} = 0, \\ R(w) = -H(-g(w))\epsilon_p g(w), \end{cases} \tag{3.8}$$

which is the strong form including contact conditions. The constant $\epsilon_p > 0$ represents the penalty parameter, $g(w)$ the gap function (Eq. 3.6), and $H : \mathbb{R} \to \{0, 1\}$ the heaviside function expressing that there is only a contact reaction force if penetration occurs, which is defined as

$$H(-g(w)) := \begin{cases} 0 & \text{if } g(w) > 0 \\ 1 & \text{if } g(w) \leq 0 \end{cases}. \tag{3.9}$$

If contact occurs we have $R(w) = -\epsilon_p g(w)$, which can be interpreted as a spring force, with ϵ_p the spring constant and $g(w)$ the displacement. In case of no contact we have $R(w) = 0$.
Turning to the weak form we supplement it with an additional term given by

$$\int_\Omega -H(-g(w))\epsilon_p g(w)\phi \mathrm{d}x \tag{3.10}$$

The amount of penetration depends on the penalty parameter ϵ_p. If $\epsilon_p \to \infty$ no penetration is allowed, but this results in an ill-conditioned discretized system [13, 14]. If $\epsilon_p \to 0$ we omit contact and the integral in Eq. 3.10 becomes zero. Therefore, ϵ_p should be chosen carefully [13]. The weak form including contact is given by

$$(\mathbf{W_c}) \begin{cases} \text{Given constants } P, q, \epsilon_p, \text{ and } h(x), \\ \text{find } (u, w) \in \mathcal{S}_u(\Omega) \times \mathcal{S}_w(\Omega), \text{ such that,} \\ \displaystyle\int_\Omega (u_{,x} + \frac{1}{2} w_{,x}^2)\psi_{,x} \mathrm{d}x = [-P\psi]_{x=1}, \\ \displaystyle\int_\Omega w_{,xx}\phi_{,xx} \mathrm{d}x + \int_\Omega H(-g(w))\epsilon_p g(w)\phi \mathrm{d}x = \int_\Omega (P w_{,x}\phi_{,x} + q\phi)\mathrm{d}x, \\ \forall (\psi, \phi) \in \mathcal{S}_u(\Omega) \times \mathcal{S}_w(\Omega). \end{cases} \tag{3.11}$$

Discretization of the weak form including contact results in additional terms to $\underline{\boldsymbol{f}}^e_{in2}$ and $\underline{\boldsymbol{f}}^e_{ex2}$ of Eq. 2.33. More specifically we have [13, 14]

$$\begin{aligned} \underline{\boldsymbol{f}}^e_{in2p} &= \underline{\boldsymbol{f}}^e_{in2} + \int_{\Omega^e} \epsilon_p \underline{\underline{\boldsymbol{C}}}^e (\underline{\underline{\boldsymbol{C}}}^e)^T \underline{\boldsymbol{\Upsilon}}^e \mathrm{d}x, \\ \underline{\boldsymbol{f}}^e_{ex2p} &= \underline{\boldsymbol{f}}^e_{ex2} - \int_{\Omega^e} \epsilon_p \underline{\underline{\boldsymbol{C}}}^e \underline{\boldsymbol{h}}^e \mathrm{d}x, \end{aligned} \tag{3.12}$$

where $\underline{\underline{\boldsymbol{C}}}^e$ is given by

$$\left(\underline{\underline{\boldsymbol{C}}}^e\right)^T = \underline{\underline{\boldsymbol{C}}}^e(\underline{\boldsymbol{\Upsilon}}^e)^T = \begin{bmatrix} 0 & 0 & a_1 & 0 & 0 & 0 \\ 0 & 0 & 0 & 0 & a_2 & 0 \end{bmatrix}. \tag{3.13}$$

Supplementing the element vectors with the additional contact terms also influences the tangent stiffness matrix $\underline{\underline{\boldsymbol{T}}}$.
If node one of element e is in contact we have $a_1 = 1$, and if node two of element e is in contact we have $a_2 = 1$. If there is no contact $\underline{\underline{\boldsymbol{C}}}^e(\underline{\boldsymbol{\Upsilon}}^e) = \underline{\underline{\boldsymbol{O}}}_{6\times 2}$, with $\underline{\underline{\boldsymbol{O}}}_{i\times j}$ the zero matrix of corresponding dimensions. The vector $\underline{\boldsymbol{h}}^e = (h_1, h_2)^T \in \mathbb{R}^2$ represents the distance of node one and two of element e to the rigid foundation, respectively. The contact algorithm is based on the discrete gap function per element given by

$$g_i^e = h_i^e + w_i, \qquad i \in \{1, 2\}, \qquad e \in \{1, ..., N_e\}. \tag{3.14}$$

Node i of element e is in contact if $g_i^e \leq 0$. The pseudo-algorithm for a non-linear finite element code with contact conditions is given by [13]

Initialize solution vector $\underline{\boldsymbol{\Upsilon}}_0$

LOOP over increments: $t = 1, ...$

- LOOP over iterations: $k = 1, ...$
  - LOOP over elements: $e = 1, ...$
    - Check for contact $g_i^e \leq 0 \rightarrow$ active node $\rightarrow$ set a_1 and/or a_2 equal to 1
    - Assemble system of equations
  - END LOOP
  - Solve: $(\underline{\boldsymbol{f}}_{in1}, \underline{\boldsymbol{f}}_{in2p})^T - (\underline{\boldsymbol{f}}_{ex1}, \underline{\boldsymbol{f}}_{ex2p})^T = \underline{\boldsymbol{0}}$
  - Check for convergence $\|\underline{\boldsymbol{R}}\|_2 \leq \epsilon \Rightarrow$ STOP
- END LOOP

END LOOP

3.2.2 Results

The contact conditions are implemented in MATLAB, and validated through a comparison with Marc & Mentat. We again consider the beam shown in Fig. 2.3, and include contact conditions. In particular the beam is located at a constant distance of $h = h(x) = 0.1$ above a rigid foundation. We want to investigate the contact conditions solely, i.e. without buckling, and therefore we omit the axial load P. We use a transverse load $q_0 = -100$ (negative sign to push the beam towards the rigid foundation), $q = \Lambda q_0$, and the beam consists of 100 elements. Conducting several test simulations revealed that $\epsilon_p = 1 \cdot 10^8$ is a good penalty parameter. The result of the simulation is shown in Fig. 3.4.

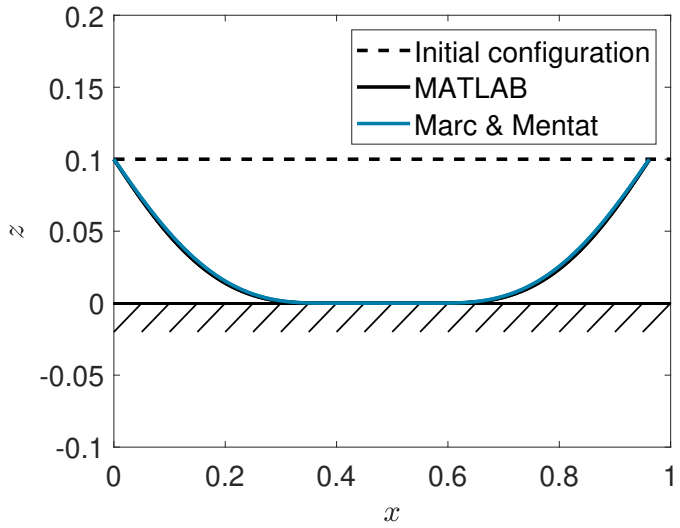

Figure 3.4: *Contact example; Initial configuration and deformed configuration for our (MATLAB) model and the Marc & Mentat model*

Fig. 3.4 shows the initial configuration of the beam and the deformed configuration after applying the transverse load q for our model and the Marc & Mentat model. Both solutions look similar, even though the models are different. The model in Marc & Mentat distinguishes between the initial and the deformed configuration (i.e. large deformations). This is neglected in our model. Nevertheless, according to Fig. 3.4 we conclude that the "small strain moderately large rotation" assumption is sufficient for this example. Moreover, a direct constraint elimination method is used for contact implementation in Marc & Mentat, whereas a penalty method is used in our model. This shows that different methods for contact implementation result in similar solutions. For more details on the direct constraint elimination method we refer to Wriggers [13]. In our model we use the penalty method which always allows for some penetration. The maximum amount of penetration in this example is $5.5 \cdot 10^{-6}$, which is small compared to the length of the beam. Based on the results shown in Fig. 3.4 we conclude that the contact conditions are implemented correctly in our model by means of the penalty method.
The next step is a post-buckling simulation involving contact conditions. To do so we consider a beam initially in contact with a rigid foundation, and apply a transverse load q on it, see Fig. 3.5.

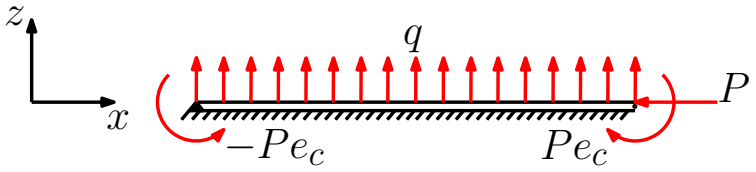

Figure 3.5: *Beam initially in contact with a rigid foundation and subjected to axial load P, transverse load q, and boundary moments $\pm Pe_c$.*

This model can be interpreted as a simplification of the paper sheet sucked to the printing table, and subjected to buckling. To mimic the buckling process we apply an axial load P. A certain initial disturbance is necessary to initiate buckling, which is achieved by means of eccentric loading boundary conditions, resulting in two boundary moments. We apply an axial load P at a distance $e_c \ll 1$ from its central line, resulting in two boundary moments, see Fig. 3.5. The distance e_c is referred to as the *eccentricity*. Supplementing the weak form with the contact conditions and the

eccentric loading boundary conditions, results in

$$(\mathbf{W_c^e})\begin{cases}\text{Given constants } P, q, e_c, \epsilon_p, \text{ and } h(x),\\ \text{find } (u,w) \in \mathcal{S}_u(\Omega)\times\mathcal{S}_w(\Omega), \text{ such that,}\\ \int_\Omega (u_{,x}+\frac{1}{2}w_{,x}^2)\psi_{,x}\mathrm{d}x = [-P\psi]_{x=1},\\ \int_\Omega w_{,xx}\phi_{,xx}\mathrm{d}x + \int_\Omega \epsilon_p H(-g(w))g(w)\phi\mathrm{d}x = \int_\Omega (Pw_{,x}\phi_{,x}+q\phi)\mathrm{d}x + [Pe_c\phi_{,x}]_{\partial\Omega},\\ \forall(\psi,\phi)\in\mathcal{S}_u(\Omega)\times\mathcal{S}_w(\Omega).\end{cases} \tag{3.15}$$

Both our model and the Marc & Mentat model experience convergence issues during simulations. We use $q=-0.1$, $P_0=12$, $P=\Lambda P_0$, $e_c=1\cdot10^{-4}$, $\epsilon_p=1\cdot10^{8}$, and as iterative solver the arc-length method having a variable load parameter. To compare the deformed configuration of our model with the deformed configuration of the Marc & Mentat model we normalize the transverse displacement by its maximum, i.e. $w^h(x)/w^h_{max}$. The resulting normalized deformed configurations are shown in Fig. 3.6b. The load parameter Λ vs maximum transverse displacement curve is shown in Fig. 3.6a. *NOTE*, no normalization is used for the results of Fig. 3.6a.

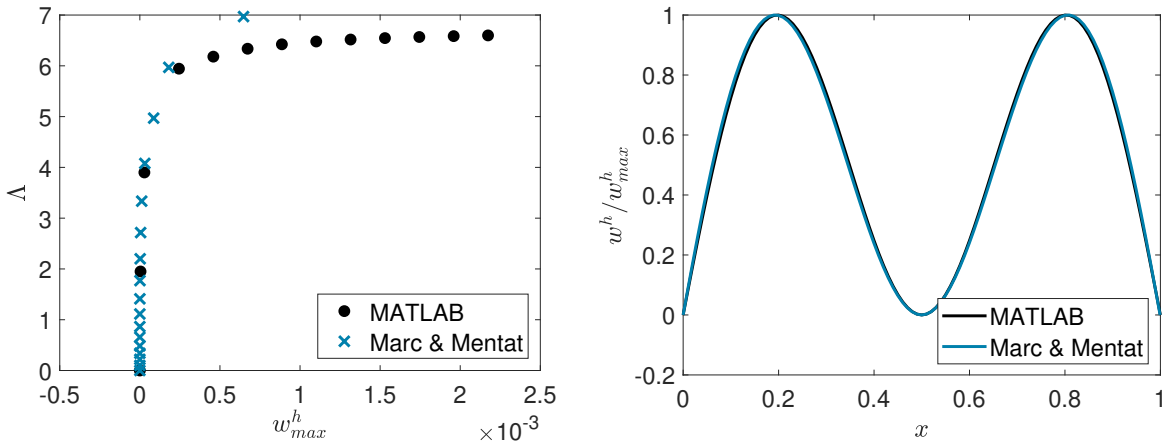

(a) *Load vs maximum transverse displacement curve.* **(b)** *Deformed configuration.*

Figure 3.6: *Deformed configuration and load vs maximum transverse displacement curve of beam subject to contact conditions and a transverse load.*

Both our model and the Marc & Mentat model have convergence issues at the moment of buckling and in the post-buckling regime. Fig. 3.6a shows a similar result between our model and the Marc & Mentat model in the pre-buckling regime. At the point of buckling the solutions deviate. Nevertheless we can see that the critical load parameter is approximately $\lambda_c \approx 6.8$. Fig. 3.6b shows that the normalized deformed configurations are similar. Next we compare the result of Fig. 3.6 including contact conditions and a transverse load with the result of Fig. 3.1, which does not include contact and a transverse load. First of all we see that the transverse load q and contact conditions have a major effect on the critical buckling load parameter and the corresponding buckling pattern. The deformed configuration of Fig. 3.6b is different compared to the deformed configuration of Fig. 3.1b. The critical buckling load parameter in Fig. 3.6a is approximately 6.8, whereas Fig. 3.1a shows that it is approximately 0.82. This implies that including contact conditions and a transverse load $q=-0.1$ results in a more than eight times larger critical load parameter compared to the model without transverse load and contact. If we omit the axial load P, eccentric

moment boundary conditions and contact conditions such that we only consider the transverse load $q = -0.1$ we obtain a maximum absolute transverse displacement of $|w^h_{max}| \approx 1.3 \cdot 10^{-3} \ll 1$, which is small. All together this small transverse load $q = -0.1$, eccentric moment boundary conditions and contact conditions, result in a more than eight times larger critical load parameter compared to the model without contact, eccentric boundary moments and contact conditions. This strong effect on the critical load parameter, and the convergence issues make the results of Fig. 3.6 unreliable.
According to Sec. 3.1 eigenvalue analysis offers perspective for buckling simulations. Performing an ordinary eigenvalue analysis on the model including contact conditions is not possible as the contact conditions are not updated during the eigenvalue analysis: nodes that are defined to be in contact before performing the eigenvalue analysis remain in contact. Nodes which are not in contact before performing the eigenvalue analysis are free to move and might penetrate in the rigid foundation during the simulation. To overcome this problem, but to nevertheless perform an eigenvalue analysis we consider a so-called *cone constrained eigenvalue problem*.

3.3 Cone constrained eigenvalue problem

A *cone constrained eigenvalue problem* supplements the ordinary eigenvalue problem with an additional constraint [16, 17]. Sio et al. [18] formulated elastic buckling of a slender column with unilateral support as a cone constrained eigenvalue problem. Since our problem is closely related to buckling of a column with unilateral support we also formulate it as a cone constrained eigenvalue problem. The cone constrained eigenvalue problem is solved by a non-smooth Newton-type algorithm [16].

3.3.1 Preliminaries

Via the cone constrained eigenvalue problem we want to obtain the critical load parameter λ at which buckling occurs, and the corresponding buckling pattern, without penetration of the rigid foundation. In Sec. 3.1 we concluded that the tangent stiffness matrix is constant in the pre-buckling regime and that the critical buckling load is fully determined by the transverse equilibrium equation. Considering only the transverse equilibrium equation allows us to write its discretized form as a linear system of equations; $(\underline{\underline{\boldsymbol{K}}} - \lambda \underline{\underline{\boldsymbol{G}}})\underline{\boldsymbol{d}} = \underline{\boldsymbol{f}}_q$, where the matrices and vector at element level are given by

$$\begin{aligned} \underline{\underline{\boldsymbol{K}}}^e &= \int_{\Omega^e} \underline{\boldsymbol{\phi}}^e_{,xx} (\underline{\boldsymbol{\phi}}^e_{,xx})^T \mathrm{d}x, \\ \underline{\underline{\boldsymbol{G}}}^e &= \int_{\Omega^e} P_0 \underline{\boldsymbol{\phi}}^e_{,x} (\underline{\boldsymbol{\phi}}^e_{,x})^T \mathrm{d}x, \\ \underline{\boldsymbol{f}}^e_q &= \int_{\Omega e} q \underline{\boldsymbol{\phi}}^e \mathrm{d}x, \end{aligned} \tag{3.16}$$

with λ a critical load parameter. The displacement vector $\underline{\boldsymbol{d}} = (\underline{\boldsymbol{w}}, \underline{\boldsymbol{w}}_{,x})^T$ is only partially constrained by contact conditions, i.e. only the displacement field $\underline{\boldsymbol{w}}$ should be non-negative. Therefore we partition the system according to

$$\underline{\boldsymbol{d}} = \begin{bmatrix} \underline{\boldsymbol{w}}_c \\ \underline{\boldsymbol{w}}_f \end{bmatrix}, \qquad \underline{\underline{\boldsymbol{K}}} = \begin{bmatrix} \underline{\underline{\boldsymbol{K}}}_{cc} & \underline{\underline{\boldsymbol{K}}}_{cf} \\ \underline{\underline{\boldsymbol{K}}}_{fc} & \underline{\underline{\boldsymbol{K}}}_{ff} \end{bmatrix}, \qquad \underline{\underline{\boldsymbol{G}}} = \begin{bmatrix} \underline{\underline{\boldsymbol{G}}}_{cc} & \underline{\underline{\boldsymbol{G}}}_{cf} \\ \underline{\underline{\boldsymbol{G}}}_{fc} & \underline{\underline{\boldsymbol{G}}}_{ff} \end{bmatrix}, \tag{3.17}$$

where the subscript c corresponds to **c**onstrained and f to **f**ree. For notational convenience we use $\underline{\boldsymbol{w}}_c = \underline{\boldsymbol{w}} \in \mathbb{R}^m$ and $\underline{\boldsymbol{w}}_f = \underline{\boldsymbol{w}}_{,x} \in \mathbb{R}^n$, with $m = N - 2$ and $n = N$, as defined in Sec. 2.5. The partitioned matrices have corresponding dimensions. During the theoretical derivation of the

cone constrained eigenvalue problem we omit the transverse load q, and therefore the external load vector $\underline{\boldsymbol{f}}_q$. At a later stadium it is introduced again.

3.3.2 Theory

The general definition of a cone constrained eigenvalue problem is given by finding a $\lambda \in \mathbb{R}$, and nonzero vector $\underline{\boldsymbol{x}} \in \mathbb{R}^d$ such that

$$K \ni \underline{\boldsymbol{x}} \perp (\underline{\underline{\boldsymbol{A}}} - \lambda \underline{\underline{\boldsymbol{B}}})\underline{\boldsymbol{x}} \in K^+. \tag{3.18}$$

With $\perp$ indicating orthogonality with respect to the standard inner product on $\mathbb{R}^d$, $\underline{\underline{\boldsymbol{A}}}$ and $\underline{\underline{\boldsymbol{B}}}$ are real square matrices, K a closed convex cone, and K^+ the positive dual cone of K defined as

$$K^+ := \{\underline{\boldsymbol{b}} \in \mathbb{R}^d \mid \langle \underline{\boldsymbol{b}}, \underline{\boldsymbol{a}} \rangle \geq 0, \quad \forall \underline{\boldsymbol{a}} \in K\}. \tag{3.19}$$

We always assume that $\langle \underline{\boldsymbol{x}}, \underline{\underline{\boldsymbol{B}}}\underline{\boldsymbol{x}} \rangle \neq 0$, for all $\underline{\boldsymbol{x}} \in K$. The orthogonality condition in Eq. 3.18 implies that

$$\lambda = \frac{\langle \underline{\boldsymbol{x}}, \underline{\underline{\boldsymbol{A}}}\underline{\boldsymbol{x}} \rangle}{\langle \underline{\boldsymbol{x}}, \underline{\underline{\boldsymbol{B}}}\underline{\boldsymbol{x}} \rangle}, \tag{3.20}$$

as in a classical generalized eigenvalue problem, but $\underline{\underline{\boldsymbol{A}}}x - \lambda \underline{\underline{\boldsymbol{B}}}x$ may be different from zero. In many applications the convex cone K is chosen to be the non-negative orthant. For this specific choice of the cone, Eq. 3.18 takes the form

$$\underline{\boldsymbol{x}} \geq \underline{\boldsymbol{0}}, \qquad (\underline{\underline{\boldsymbol{A}}} - \lambda \underline{\underline{\boldsymbol{B}}})\underline{\boldsymbol{x}} \geq \underline{\boldsymbol{0}}, \qquad \langle \underline{\boldsymbol{x}}, (\underline{\underline{\boldsymbol{A}}} - \lambda \underline{\underline{\boldsymbol{B}}})\underline{\boldsymbol{x}} \rangle = 0, \tag{3.21}$$

which is a so-called *Pareto* eigenvalue problem [16, 17]. The quantity $\underline{\boldsymbol{x}}$ is the so-called *Pareto* eigenvector, λ the *Pareto* eigenvalue, and together they form the *Pareto* eigenpair $(\underline{\boldsymbol{x}}, \lambda)$.
We consider our beam to be cone-constrained, such that we can write it in the form of a *Pareto* eigenvalue problem (Eq. 3.21). We use $\underline{\underline{\boldsymbol{A}}} = \underline{\underline{\boldsymbol{K}}}$, $\underline{\underline{\boldsymbol{B}}} = \underline{\underline{\boldsymbol{G}}}$, and $\underline{\boldsymbol{x}} = \underline{\boldsymbol{d}}$, given by Eq. 3.17. Since the displacement vector $\underline{\boldsymbol{d}}$ is only partially constrained we consider the convex cone, respectively dual cone, to be

$$\begin{aligned} K &= \mathbb{R}^m_+ \times \mathbb{R}^n, \\ K^+ &= \mathbb{R}^m_+ \times \{0\}^n, \end{aligned} \tag{3.22}$$

where $\mathbb{R}_+$ represents the non-negative orthant. As a first step towards reformulation of the *Pareto* eigenvalue problem (Eq. 3.21) as a system of equations in terms of the partitioned forms of $\underline{\underline{\boldsymbol{K}}}, \underline{\underline{\boldsymbol{G}}}, \underline{\boldsymbol{d}}$ given by Eq. 3.17, we write

$$\underline{\boldsymbol{w}}_c \geq 0, \qquad \underline{\boldsymbol{w}}_f \text{ free}, \qquad \text{Eigenvector feasibility,} \tag{3.23}$$

$$\underline{\boldsymbol{y}}_c \geq 0, \qquad \underline{\boldsymbol{y}}_f = 0, \qquad \text{dual feasibilitiy,} \tag{3.24}$$

$$\langle \underline{\boldsymbol{w}}_c, \underline{\boldsymbol{y}}_c \rangle + \langle \underline{\boldsymbol{w}}_f, \underline{\boldsymbol{y}}_f \rangle = 0, \qquad \text{complementarity slackness,} \tag{3.25}$$

$$\begin{bmatrix} \underline{\underline{\boldsymbol{K}}}_{cc} & \underline{\underline{\boldsymbol{K}}}_{cf} \\ \underline{\underline{\boldsymbol{K}}}_{fc} & \underline{\underline{\boldsymbol{K}}}_{ff} \end{bmatrix} \begin{bmatrix} \underline{\boldsymbol{w}}_c \\ \underline{\boldsymbol{w}}_f \end{bmatrix} - \lambda \begin{bmatrix} \underline{\underline{\boldsymbol{G}}}_{cc} & \underline{\underline{\boldsymbol{G}}}_{cf} \\ \underline{\underline{\boldsymbol{G}}}_{fc} & \underline{\underline{\boldsymbol{G}}}_{ff} \end{bmatrix} \begin{bmatrix} \underline{\boldsymbol{w}}_c \\ \underline{\boldsymbol{w}}_f \end{bmatrix} = \begin{bmatrix} \underline{\boldsymbol{y}}_c \\ \underline{\boldsymbol{y}}_f \end{bmatrix}, \qquad \text{equilibrium law,} \tag{3.26}$$

$$\langle \underline{\boldsymbol{1}}_m, \underline{\boldsymbol{w}}_c \rangle = c^*, \qquad \text{normalization}^1, \tag{3.27}$$

where the notation $\underline{\boldsymbol{w}}_c \geq 0$ indicates that each component of $\underline{\boldsymbol{w}}_c$ is nonnegative, and $\underline{\boldsymbol{1}}_m \in \mathbb{R}^m$ represents a vector of ones. The vector $\underline{\boldsymbol{y}}_c$ can be interpreted as a reaction force, which has only a

[1] Since $\underline{\boldsymbol{w}}_c \geq 0$ we may simplify $\|\underline{\boldsymbol{w}}_c\|_2$ to the linear function $\langle \underline{\boldsymbol{1}}_m, \underline{\boldsymbol{w}}_c \rangle$ [16].

non-zero value if contact occurs. The normalization condition ensures that $\underline{\boldsymbol{w}}_c$ is a nonzero vector, with $c^* > 0$ a constant. At first we follow Adly and Seeger [16], and use Eq. 3.27, with $c^* = 1$. *NOTE*, Eq. 3.27 is not mesh-independent, but since the choice of the normalization function does not change the solution substantially we use the linear function $\langle \underline{\mathbf{1}}_m, \cdot \rangle$ [16, 17]. The feasibility and complementarity slackness conditions (Eq. 3.23, Eq. 3.24, and Eq. 3.25) can be written in the succinct form $\underline{\boldsymbol{U}}_\varphi(\underline{\boldsymbol{w}}_c, \underline{\boldsymbol{y}}_c) = \underline{\mathbf{0}}$, with $\underline{\boldsymbol{U}}_\varphi : \mathbb{R}^m \times \mathbb{R}^m \to \mathbb{R}^m$ given by

$$\underline{\boldsymbol{U}}_\varphi(\underline{\boldsymbol{w}}_c, \underline{\boldsymbol{y}}_c) = \begin{bmatrix} \varphi(w_1, y_1) \\ \vdots \\ \varphi(w_m, y_m) \end{bmatrix}, \tag{3.28}$$

with $\varphi : \mathbb{R} \times \mathbb{R} \to \mathbb{R}$ a complementarity function, i.e.

$$\varphi(a, b) = 0 \qquad \Longleftrightarrow \qquad a \geq 0, \qquad b \geq 0, \qquad ab = 0. \tag{3.29}$$

With Eq. 3.28, the equilibrium law, the normalization condition, and some simplifications it is possible to introduce the vector function $\underline{\boldsymbol{\Phi}} : \mathbb{R}^m \times \mathbb{R}^n \times \mathbb{R}^m \times \mathbb{R} \to \mathbb{R}^{2m+n+1}$ as

$$\underline{\boldsymbol{\Phi}}(\underline{\boldsymbol{w}}_c, \underline{\boldsymbol{w}}_f, \underline{\boldsymbol{y}}_c, \lambda) = \begin{bmatrix} \underline{\boldsymbol{U}}_\varphi(\underline{\boldsymbol{w}}_c, \underline{\boldsymbol{y}}_c) \\ \underline{\underline{\boldsymbol{K}}}_{cc}\underline{\boldsymbol{w}}_c + \underline{\underline{\boldsymbol{K}}}_{cf}\underline{\boldsymbol{w}}_f - \lambda(\underline{\underline{\boldsymbol{G}}}_{cc}\underline{\boldsymbol{w}}_c + \underline{\underline{\boldsymbol{G}}}_{cf}\underline{\boldsymbol{w}}_f) - \underline{\boldsymbol{y}}_c \\ \underline{\underline{\boldsymbol{K}}}_{fc}\underline{\boldsymbol{w}}_c + \underline{\underline{\boldsymbol{K}}}_{ff}\underline{\boldsymbol{w}}_f - \lambda(\underline{\underline{\boldsymbol{G}}}_{fc}\underline{\boldsymbol{w}}_c + \underline{\underline{\boldsymbol{G}}}_{ff}\underline{\boldsymbol{w}}_f) \\ \langle \underline{\mathbf{1}}_m, \underline{\boldsymbol{w}}_c \rangle - c^* \end{bmatrix}. \tag{3.30}$$

The troublesome part of Eq. 3.30 is the vector function $\underline{\boldsymbol{U}}_\varphi$ as complementarity functions are in general nonsmooth [16]. Different options for complementarity functions are possible. Here the "lattice", Fischer-Burmeister, and Evtushenko-Purtov complementarity functions are used, and are given by [16]

$$\begin{aligned} \varphi_{min}(a, b) &= \min\{a, b\}, \\ \varphi_{FB}(a, b) &= \sqrt{a^2 + b^2} - a - b, \\ \varphi_{EP}(a, b) &= 2ab - (\min\{0, a + b\})^2. \end{aligned} \tag{3.31}$$

We observe that φ_{min} and φ_{FB} are nonsmooth, but φ_{EP} is a smooth complementarity function. The non-linear system $\underline{\boldsymbol{\Phi}} = \underline{\mathbf{0}}$ is solved for $\underline{\boldsymbol{z}} := (\underline{\boldsymbol{w}}_c, \underline{\boldsymbol{w}}_f, \underline{\boldsymbol{y}}_c, \lambda)^T$ using Newton's method, given by

$$\begin{aligned} \Delta\underline{\boldsymbol{z}} &= -\underline{\boldsymbol{\Phi}}_{,\underline{\boldsymbol{z}}}^{-1}(\underline{\boldsymbol{z}}_k)\underline{\boldsymbol{\Phi}}(\underline{\boldsymbol{z}}_k), \\ \underline{\boldsymbol{z}}_{k+1} &= \underline{\boldsymbol{z}}_k + \Delta\underline{\boldsymbol{z}}, \end{aligned} \tag{3.32}$$

with $\underline{\boldsymbol{\Phi}}_{,\underline{\boldsymbol{z}}}(\underline{\boldsymbol{z}}_k)$ the Jacobian matrix of Eq. 3.30 evaluated at iteration k. Due to the non-smooth complementarity functions we call Newton's method (Eq. 3.32) for the non-differentiable $\underline{\boldsymbol{\Phi}}$ in Eq. 3.32 a **s**emi-smooth **N**ewton **a**lgorithm (SNA). The Jacobian matrix is given by the following block representation

$$\underline{\boldsymbol{\Phi}}_{,\underline{\boldsymbol{z}}}(\underline{\boldsymbol{z}}_k) := \begin{bmatrix} \underline{\underline{\boldsymbol{E}}}_k & \underline{\underline{\boldsymbol{O}}}_{m\times n} & \underline{\underline{\boldsymbol{F}}}_k & \underline{\mathbf{0}}_m \\ \underline{\underline{\boldsymbol{K}}}_{cc} - \lambda_k\underline{\underline{\boldsymbol{G}}}_{cc} & \underline{\underline{\boldsymbol{K}}}_{cf} - \lambda_k\underline{\underline{\boldsymbol{G}}}_{cf} & -\underline{\underline{\boldsymbol{I}}}_{m\times m} & -\underline{\underline{\boldsymbol{G}}}_{cc}\underline{\boldsymbol{w}}_{c_k} - \underline{\underline{\boldsymbol{G}}}_{cf}\underline{\boldsymbol{w}}_{f_k} \\ \underline{\underline{\boldsymbol{K}}}_{fc} - \lambda_k\underline{\underline{\boldsymbol{G}}}_{fc} & \underline{\underline{\boldsymbol{K}}}_{ff} - \lambda_k\underline{\underline{\boldsymbol{G}}}_{ff} & \underline{\underline{\boldsymbol{O}}}_{n\times m} & -\underline{\underline{\boldsymbol{G}}}_{fc}\underline{\boldsymbol{w}}_{c_k} - \underline{\underline{\boldsymbol{G}}}_{ff}\underline{\boldsymbol{w}}_{f_k} \\ \underline{\mathbf{1}}_m^T & \underline{\mathbf{0}}_n^T & \underline{\mathbf{0}}_m^T & 0 \end{bmatrix}, \tag{3.33}$$

where a subscript k shows that it depends on the iteration. The vectors $\underline{\boldsymbol{w}}_{c_k}$ and $\underline{\boldsymbol{w}}_{f_k}$ represent the vectors $\underline{\boldsymbol{w}}_c$ and $\underline{\boldsymbol{w}}_f$ at iteration k, respectively. The matrices $\underline{\underline{\boldsymbol{E}}}_k$ and $\underline{\underline{\boldsymbol{F}}}_k$ are diagonal, given by

$\underline{\underline{\boldsymbol{E}}}_k = \text{diag}(r_k^1, r_k^2, ..., r_k^m)$ and $\underline{\underline{\boldsymbol{F}}}_k = \text{diag}(s_k^1, s_k^2, ..., s_k^m)$, where the diagonal components are given by

$$
r_k^i := \begin{cases} \begin{cases} 1 & \text{if } w_{c_k}^i \leq y_{c_k}^i \\ 0 & \text{otherwise} \end{cases}, & \text{if } \varphi = \varphi_{min}, \\ \dfrac{w_{c_k}^i}{\sqrt{\left(w_{c_k}^i\right)^2 + \left(y_{c_k}^i\right)^2}} - 1, & \text{if } \varphi = \varphi_{FB}, \\ \begin{cases} 2y_{c_k}^i & \text{if } w_{c_k}^i + y_{c_k}^i \geq 0 \\ -2w_{c_k}^i & \text{otherwise} \end{cases}, & \text{if } \varphi = \varphi_{EP}, \end{cases}
$$

$$
s_k^i := \begin{cases} \begin{cases} 0 & \text{if } w_{c_k}^i \leq y_{c_k}^i \\ 1 & \text{otherwise} \end{cases}, & \text{if } \varphi = \varphi_{min}, \\ \dfrac{y_{c_k}^i}{\sqrt{\left(w_{c_k}^i\right)^2 + \left(y_{c_k}^i\right)^2}} - 1, & \text{if } \varphi = \varphi_{FB}, \\ \begin{cases} 2w_{c_k}^i & \text{if } w_{c_k}^i + y_{c_k}^i \geq 0 \\ -2y_{c_k}^i & \text{otherwise} \end{cases}, & \text{if } \varphi = \varphi_{EP}, \end{cases}
$$

(3.34)

with $i \in \{1, 2, ..., m\}$. The convergence criterion chosen for the SNA is $\|\underline{\boldsymbol{\Phi}}(\underline{\boldsymbol{z}}_k)\|_2 \leq 1 \cdot 10^{-8}$. There are no theoretical results on the best way of selecting the initial point [16, 17]. Following Adly & Seeger [16] we generate a random vector $\underline{\boldsymbol{\xi}} \in \mathbb{R}^{m+n}$ with uniform distribution on $[-1, 1]^{m+n}$ and set

$$
\underline{\boldsymbol{d}}_0 = (\underline{\boldsymbol{w}}_{c_0}, \underline{\boldsymbol{w}}_{f_0})^T = \frac{\underline{\boldsymbol{\xi}}}{\langle \underline{\mathbf{1}}_{m+n}, \underline{\boldsymbol{\xi}} \rangle}, \qquad \lambda_0 = \frac{\langle \underline{\boldsymbol{d}}_0, \underline{\underline{\boldsymbol{K}}}\, \underline{\boldsymbol{d}}_0 \rangle}{\langle \underline{\boldsymbol{d}}_0, \underline{\underline{\boldsymbol{G}}}\, \underline{\boldsymbol{d}}_0 \rangle}, \qquad \underline{\boldsymbol{y}}_0 = \underline{\underline{\boldsymbol{K}}}\, \underline{\boldsymbol{d}}_0 - \lambda_0 \underline{\underline{\boldsymbol{G}}}\, \underline{\boldsymbol{d}}_0. \tag{3.35}
$$

We have different choices for the complementarity function used in the SNA. First of all we investigate the behaviour of the three complementarity functions defined in Eq. 3.31. For the model with $P_0 = 12$, without transverse load q we know that the solution is given by the half sine-wave function shown in Fig. 3.1b, with corresponding critical load parameter $\lambda = \pi^2/12 \approx 0.82$. Because we omit the transverse load q there is no reaction force $\boldsymbol{y}_c$, and therefore the only admissible solution is the half sine-wave solution of Fig. 3.1b with eigenvalue $\lambda = \pi^2/12$. We generate ten random initial vectors $\underline{\boldsymbol{\xi}}_i \in \mathbb{R}^{m+n}, i \in \{1, 2, ..., 10\}$, use $N_e = 100$ elements, perform the SNA Eq. 3.32, and look at the amount of iterations needed per complementarity function to converge to the half sine-wave solution. Tab. 3.1 shows the amount of iterations necessary to converge for the different complementarity functions. The maximum amount of iterations is set to 2000; if the SNA did not converge within these 2000 iterations we indicate it with a "-".

Table 3.1: *Number of iterations needed for the SNA to converge using different complementarity functions and different random initial vectors*

	$\underline{\boldsymbol{\xi}}_1$	$\underline{\boldsymbol{\xi}}_2$	$\underline{\boldsymbol{\xi}}_3$	$\underline{\boldsymbol{\xi}}_4$	$\underline{\boldsymbol{\xi}}_5$	$\underline{\boldsymbol{\xi}}_6$	$\underline{\boldsymbol{\xi}}_7$	$\underline{\boldsymbol{\xi}}_8$	$\underline{\boldsymbol{\xi}}_9$	$\underline{\boldsymbol{\xi}}_{10}$
φ_{min}	96	120	-	157	87	-	-	147	94	140
φ_{FB}	14	21	14	17	13	28	28	13	47	13
φ_{EP}	34	87	-	393	39	156	134	128	119	33

Tab. 3.1 shows that convergence is not guaranteed. It also shows that for the same initial vector $\underline{\boldsymbol{\xi}}_i$ the amount of iterations needed to converge is different for each complementarity function. Hence, the simulation time of the SNA depends on the choice of the complementarity function, even though the solution is the same. Furthermore Tab. 3.1 shows that for a chosen complementarity

function the initial vector $\underline{\boldsymbol{\xi}}_i$ influences the amount of iterations, and in some cases might not even result in convergence. Based on the results of Tab. 3.1 we can say that φ_{FB} is the best complementarity function in the sense that it requires the least amount of iterations and always converged. However, for a good judgement on which complementarity function is the best we need to test it on more random initial vectors $\underline{\boldsymbol{\xi}}_i$. Adly & Seeger [16] did this for 10^4 random initial vectors $\underline{\boldsymbol{\xi}}_i$, and conclude also that φ_{FB} has the best performance. This is an interesting result since the nonsmooth φ_{FB} outperforms the smooth φ_{EP} complementarity function, which was also found by Adly & Seeger [16]. We use φ_{FB} in the forthcoming example.

3.3.3 Results

Until now we omitted the transverse load q and therefore the external load vector $\underline{\boldsymbol{f}}_q$. The next step is to incorporate this external load vector in the SNA, which is done by extending the reaction force vector with

$$\underline{\boldsymbol{y}}_c^* = \underline{\boldsymbol{y}}_c + \underline{\boldsymbol{f}}_q. \tag{3.36}$$

Via this relation it is possible to incorporate the transverse load q in the SNA. Test simulations including a transverse load q have shown that a random initial vector $\underline{\boldsymbol{\xi}}$ results in bad[1] convergence behaviour. Therefore we choose $\underline{\boldsymbol{d}}_0$ to be an eigenvector of the ordinary eigenvalue problem $(\underline{\underline{\boldsymbol{K}}} - \lambda \underline{\underline{\boldsymbol{G}}})\underline{\boldsymbol{d}} = \underline{\boldsymbol{0}}_{m+n}$. The choice of the initial eigenvector is important for the resulting Pareto eigenvector. There are no theoretical results on which eigenvector should be chosen as initial guess. As an example we use the second eigenvector (EV2), and fifth eigenvector (EV5) as initial guess to the SNA. Furthermore we use an axial load of $P_0 = 12$, transverse load $q = -1$, convergence criterion $\|\underline{\boldsymbol{\Phi}}(\underline{\boldsymbol{z}}_k)\|_2 \leq 1 \cdot 10^{-8}$, and consider constant values of $c^* = 1$ and $c^* = 1/3$ in the normalization condition (Eq. 3.27).

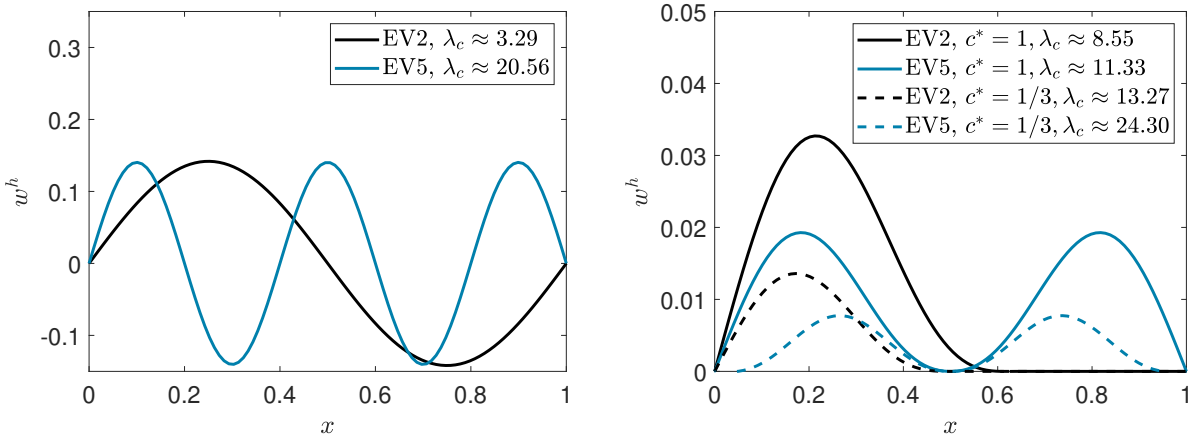

(a) *Eigenpairs used as initial guess.*

(b) *Resulting Pareto eigenpairs.*

Figure 3.7: *Eigenvectors and eigenvalues used as initial guess for the SNA and resulting Pareto eigenvectors and corresponding eigenvalues.*

Fig. 3.7a shows the eigenvectors and corresponding eigenvalues chosen as initial guess for the SNA. Fig. 3.7b shows the resulting Pareto eigenvectors and corresponding Pareto eigenvalues. We observe that all resulting Pareto eigenvectors satisfy the non-negativity constraint. Moreover the Pareto eigenvector corresponding to EV5 looks similar to the result of the post-buckling simulation of Fig.

[1] Bad refers to more iterations and more often no convergence compared to the results of Tab. 3.1.

3.6b. By looking at the Pareto eigenvalues we see that they depend on the choice of the constant c^* used in the normalization condition, which is considered to be incorrect. The normalization condition is mesh-dependent. If we choose $c^* = c^\dagger N_e$, with $c^\dagger > 0$ a constant we obtain a mesh-independent normalization condition but remain with the problem that it depends on the choice of $c^\dagger$. The reason for this is the combination of the normalization condition and $\underline{\boldsymbol{y}}_c^*$ of Eq. 3.36. In case of contact the reaction force at node i is equal to the applied transverse load (in opposite sign) at node i. If node i is not in contact we only have a contribution of the transverse load at node i. This implies that we have a jump condition in the external force vector:

$$(\underline{\boldsymbol{y}}_c^*)_i = \begin{cases} 0 & \text{if node } i \text{ is in contact} \\ (\underline{\boldsymbol{f}}_q)_i & \text{if node } i \text{ is not in contact} \end{cases}, \qquad i \in \{1, 2, ..., m\}, \tag{3.37}$$

where the subscript i represents component i of the vector. The jump condition in the components of the vector $\underline{\boldsymbol{y}}_c^*$ modify the eigenvalue problem into an ordinary determined system of equations $((\underline{\underline{\boldsymbol{K}}} - \lambda \underline{\underline{\boldsymbol{G}}})\underline{\boldsymbol{d}} = \underline{\boldsymbol{y}}_c^*)$. Since $\underline{\boldsymbol{y}}_c^*$ depends on $\underline{\boldsymbol{w}}_c$ (i.e. contact or no contact) and the jump condition (Eq. 3.37) is located between the reference configuration and a buckled configuration we are dealing with a non-linear non-smooth problem. As a consequence we are not allowed to use the normalization condition from Eq. 3.27 anymore, as $\underline{\boldsymbol{y}}_c^*$ determines the amplitude (infinity norm) of the solution. Simply removing the normalization condition from Eq. 3.30 is not an option as this results in an undetermined system, and this condition is necessary to ensure a non-trivial solution ($\underline{\boldsymbol{d}} \neq \underline{\boldsymbol{0}}_{m+n}$). To overcome the problem of an undetermined system it is possible to remove the normalization condition, solve the system for $(\underline{\boldsymbol{w}}_c, \underline{\boldsymbol{w}}_f, \underline{\boldsymbol{y}}_c)^T$, and choose a value for λ during the simulation, e.g. update it incrementally. The advantage of the cone constrained eigenvalue problem is that it returns both the deformed configuration (Pareto eigenvector), and corresponding critical load parameter (Pareto eigenvalue). Removing the normalization condition diminishes the advantage of the cone constrained eigenvalue problem, and is therefore not preferred. Another option is to find an alternative scalar condition for the normalization condition. The alternative condition should be chosen such that it ensures a non-trivial resulting Pareto eigenvector. Until now we did not manage to find such a condition.

We have shown that a cone constrained eigenvalue problem offers perspective to solve the beam model with buckling and contact. Including a transverse load q is possible, but an alternative condition should be found to replace the normalization condition. Furthermore, the initial guess to the SNA is of high importance for the resulting Pareto eigenpair. Until now there are no theoretical results on which eigenvector to choose as initial guess.

4 Two-dimensional plate model

In this section, we derive a thin-plate model subject to an increase in moisture content on (a part of) its domain. The derivation of the thin-plate model is similar to the derivation of the thin-beam model in Sec. 2. We extend the *Euler-Bernoulli beam theory* from Sec. 2 to *Kirchhoff-Love plate theory*, inluding *Von-Kármán strains*, and we use Sec. 2 as reference for the derivation of the plate model. We are only interested in the pre-buckling regime and the moment of buckling. First a strong form is derived from the global equilibrium equations, and after that it is transformed into a weak form. The weak form is discretized using the so-called *Bogner-Fox-Schmit* element. An analytical solution is used for validation of the finite element model.

4.1 Equilibrium equation

We consider a rectangular plate of constant thickness h, length a and width b with $\varepsilon = h/L \ll 1$, where $L = \sqrt{ab}$, a characteristic length for the in-plane dimensions of the plate. Let $\mathcal{B} = \Omega \times [-h/2, h/2] \subset \mathbb{R}^3$ be the undeformed reference configuration of the plate. The central plane of the plate is defined as

$$\Omega := \{\underline{\boldsymbol{x}} \mid x \in (0, a), y \in (0, b), z = 0\}. \tag{4.1}$$

The boundary of Ω is $\partial\Omega$. The plate is described by the Cartesian coordinates (x, y, z), with x and y the in-plane coordinates and z the out-of-plane coordinate, where $z = 0$ corresponds to the central plane of the plate. The *Kirchhoff-Love plate theory* is based on a set of assumptions:

1. The material of the plate is elastic and homogeneous.
2. The plate is initially flat.
3. Normals to the original configuration of the central plane of the plate remain straight and normal to this plane after deformation, i.e. the shear strains ε_{xz}, ε_{yz} are zero.
4. Pure bending keeps the central plane unstrained.
5. The stress normal to the central plane σ_{zz} is small compared to the other stress components and may be neglected.
6. To obtain the *Von-Kármán* strains, we make the extra assumption: the in-plane strains (due to stretching) are small, i.e. of $\mathcal{O}(\varepsilon^2)$, compared to the deformation and rotations due to bending ($\mathcal{O}(\varepsilon)$).

The displacements $u = u(x, y)$, and $v = v(x, y)$ represent the midplane displacements (stretches) of the central plane in $x-$ and $y-$direction, respectively, and $w = w(x, y)$ the deflection of this plane in the $z-$direction. Analogously to Sec. 2 we have the following displacement field

$$\underline{\boldsymbol{u}}(\underline{\boldsymbol{x}}) = \begin{bmatrix} u_1(\underline{\boldsymbol{x}}) \\ u_2(\underline{\boldsymbol{x}}) \\ u_3(\underline{\boldsymbol{x}}) \end{bmatrix} = \begin{bmatrix} u - zw_{,x} \\ v - zw_{,y} \\ w \end{bmatrix}. \tag{4.2}$$

The small strains, moderately large rotation assumption 6. results in the *Von-Kármán* strains:

$$\underline{\boldsymbol{\varepsilon}} = \underline{\boldsymbol{\varepsilon}}^{(0)} + z\underline{\boldsymbol{\varepsilon}}^{(1)}, \tag{4.3}$$

with

$$\underline{\boldsymbol{\varepsilon}}^{(0)} := \begin{bmatrix} \varepsilon_{xx}^{(0)} \\ \varepsilon_{yy}^{(0)} \\ \varepsilon_{xy}^{(0)} \end{bmatrix} := \begin{bmatrix} u_{,x} + w_{,x}^2/2 \\ v_{,y} + w_{,y}^2/2 \\ (u_{,y} + v_{,x} + w_{,x}w_{,y})/2 \end{bmatrix}, \qquad \underline{\boldsymbol{\varepsilon}}^{(1)} := \begin{bmatrix} \varepsilon_{xx}^{(1)} \\ \varepsilon_{yy}^{(1)} \\ \varepsilon_{xy}^{(1)} \end{bmatrix} := \begin{bmatrix} -w_{,xx} \\ -w_{,yy} \\ -w_{,xy} \end{bmatrix}. \tag{4.4}$$

Deformations resulting from a rise in temperature are often discussed in literature, see e.g. [19,20]. We consider deformations due to an increase in moisture content, which can be modeled in a similar way as a rise in temperature. The increase in moisture content is given by $\mathcal{H} : \Omega \to \mathbb{R}$ as the $z-$independent rise in moisture content. The moisture-induced strains are given by $\varepsilon_{xx}^h(x,y) = \beta_x \mathcal{H}(x,y)$ and $\varepsilon_{yy}^h = \beta_y \mathcal{H}(x,y)$, where β_x and β_y are the positive hygroexpansivity coefficients associated with their principal directions. The moisture-induced strains are given by

$$\underline{\boldsymbol{\varepsilon}}^{(h)} := \begin{bmatrix} \varepsilon_{xx}^{(h)} \\ \varepsilon_{yy}^{(h)} \\ \varepsilon_{xy}^{(h)} \end{bmatrix} := \begin{bmatrix} \beta_x \mathcal{H}(x,y) \\ \beta_y \mathcal{H}(x,y) \\ 0 \end{bmatrix}. \tag{4.5}$$

We consider the thin-plate to exhibit linear elastic behaviour, and to possess rectilinear orthotropic symmetry. The corresponding constitutive relation relating the total strain $\underline{\boldsymbol{\varepsilon}}$ to the stress and the moisture-induced strain is given by the extended Hooke's law as (compare with Hooke-Duhamel for thermo-elastic interactions)

$$\underline{\boldsymbol{\varepsilon}} = \underline{\boldsymbol{C}}^{-1}\underline{\boldsymbol{\sigma}} + \underline{\boldsymbol{\varepsilon}}^{(h)} \qquad \Rightarrow \qquad \underline{\boldsymbol{\sigma}} = \underline{\boldsymbol{C}}(\underline{\boldsymbol{\varepsilon}} - \underline{\boldsymbol{\varepsilon}}^{(h)}), \tag{4.6}$$

with

$$\underline{\boldsymbol{C}} := \begin{bmatrix} c_{11} & c_{12} & 0 \\ c_{21} & c_{22} & 0 \\ 0 & 0 & c_{66} \end{bmatrix} := \frac{1}{1-\nu_{xy}\nu_{yx}} \begin{bmatrix} E_x & E_x\nu_{yx} & 0 \\ E_y\nu_{xy} & E_y & 0 \\ 0 & 0 & 2G_{xy}(1-\nu_{xy}\nu_{yx}) \end{bmatrix}, \tag{4.7}$$

in which $E_x, E_y, \nu_{xy}, \nu_{yx}$, and G_{xy} are the Young's moduli, Poisson's ratios, and shear modulus, associated with the principal directions, respectively. Symmetry of the stress tensor[1] requires $c_{12} = c_{21} \Rightarrow E_x\nu_{yx} = E_y\nu_{xy}$.

Analogously to Sec. 2, we define the global in-plane forces (2 normal and 1 shear) $\underline{\boldsymbol{N}} := (N_{xx}, N_{yy}, N_{xy})^T$ [N/m] and bending and twisting moments $\underline{\boldsymbol{M}} := (M_{xx}, M_{yy}, M_{xy})^T$ [N], per unit of length, as

$$\underline{\boldsymbol{N}} = \int_{-h/2}^{h/2} \underline{\boldsymbol{\sigma}} \mathrm{d}z, \qquad \underline{\boldsymbol{M}} = \int_{-h/2}^{h/2} z\underline{\boldsymbol{\sigma}} \mathrm{d}z. \tag{4.8}$$

Substitution of Hooke's law (Eq. 4.6) in Eq. 4.9 results in

$$\underline{\boldsymbol{N}} = h\underline{\boldsymbol{C}}\left(\underline{\boldsymbol{\varepsilon}}^{(0)} - \underline{\boldsymbol{\varepsilon}}^{(h)}\right), \qquad \underline{\boldsymbol{M}} = \frac{h^3}{12}\underline{\boldsymbol{C}}\underline{\boldsymbol{\varepsilon}}^{(1)} = -\begin{bmatrix} D_{11}w_{xx} + D_{12}w_{yy} \\ D_{21}w_{xx} + D_{22}w_{yy} \\ D_{66}w_{xy} \end{bmatrix}, \tag{4.9}$$

with

$$\underline{\boldsymbol{D}} := \begin{bmatrix} D_{11} & D_{12} & 0 \\ D_{21} & D_{22} & 0 \\ 0 & 0 & D_{66} \end{bmatrix} = \frac{h^3}{12(1-\nu_{xy}\nu_{yx})} \begin{bmatrix} E_x & E_x\nu_{yx} & 0 \\ E_y\nu_{xy} & E_y & 0 \\ 0 & 0 & 2(1-\nu_{xy}\nu_{yx})G_{xy} \end{bmatrix}, \tag{4.10}$$

and $\underline{\boldsymbol{D}} = \underline{\boldsymbol{D}}^T$.

The derivation of the equilibrium equations is an extension of the derivation for the equilibrium

[1] The balance of angular momentum requires the Cauchy stress tensor to be symmetric.

equations described in Sec. 2, and therefore not given here. For details of this derivation we refer to App. C. The equilibrium equations are given by [1, 21]

$$M_{xx,xx} + 2M_{xy,xy} + M_{,yy} = -\left(q + N_{xx}w_{,xx} + 2N_{xy}w_{,xy} + N_{yy}w_{,yy}\right), \tag{4.11}$$

$$N_{xx,x} + N_{xy,y} + q_x = 0, \qquad N_{xy,x} + N_{yy,y} + q_y = 0, \tag{4.12}$$

where q_x and q_y are in-plane body forces [N/m^2] and $q_z = q(x, y)$ a transverse load [N/m^2]. As done in [1], it is possible to derive from these equations together with the constitutive equation Eq. 4.6 the *Föppl-Von-Kármán* equations ((9) and (10) in [1]). These *Föppl-Von-Kármán* equations describe the whole buckling process, including initial post-buckling. However, our first purpose is the determination of the critical moisture content at which buckling of the plate occurs. For this, we only need the second of the *Föppl-Von-Kármán* equations, which is derived from Eq. 4.11, by substituting the expressions for M_{xx}, M_{yy}, M_{xy} of Eq. 4.9 in it, resulting in

$$\frac{h^3}{12}\left(c_{11}w_{,xxxx} + (c_{12} + 2c_{66} + c_{21})w_{,xxyy} + c_{22}w_{,yyyy}\right) = N_{xx}w_{,xx} + N_{yy}w_{,yy} + 2N_{xy}w_{,xy} + q. \tag{4.13}$$

The $N-$forces in this equation refer to the forces in the pre-buckled state, where $w = 0$ (just before buckling). In this state, the plate is fixed to the table by suction, preventing in-plane displacements of the plate. Hence $u = v = 0$, and thus also $\underline{\boldsymbol{\varepsilon}} = \underline{\mathbf{0}}$, implying that $\underline{\boldsymbol{N}}$ is only due to the moisture, or

$$\underline{\boldsymbol{N}} = \underline{\boldsymbol{N}}^{(h)} = -h\underline{\underline{\boldsymbol{C}}}\,\underline{\boldsymbol{\varepsilon}}^{(h)} = \begin{bmatrix} N_{xx}^{(h)} \\ N_{yy}^{(h)} \\ N_{xy}^{(h)} \end{bmatrix} = -h \begin{bmatrix} c_{11}\beta_x + c_{12}\beta_y \\ c_{21}\beta_x + c_{22}\beta_y \\ 0 \end{bmatrix} \mathcal{H}(x, y). \tag{4.14}$$

We introduce $\Omega_M \subseteq \Omega$ as the moisture-affected area, and therewith $\chi_M : \Omega \to \{0, 1\}$ as the indicator function for Ω_M. Substituting the force resultants of Eq. 4.14 in the equilibrium equation (Eq. 4.11), and writing $\mathcal{H}(x, y) = \chi_M(x, y)\lambda$, with $\lambda \in \mathbb{R}$ a value representing the increase in moisture content, which is used later as critical eigenvalue, we obtain

$$\begin{aligned} &D_{11}w_{,xxxx} + (D_{12} + 2D_{66} + D_{21})w_{,xxyy} + D_{22}w_{,yyyy} = \\ &-\lambda\left[(A_{11} + A_{12})w_{,xx} + (A_{21} + A_{22})w_{,yy}\right]\chi_M + q, \end{aligned} \tag{4.15}$$

with $\underline{\underline{\boldsymbol{D}}}$ given by Eq. 4.10, and

$$\underline{\underline{\boldsymbol{A}}} := \begin{bmatrix} A_{11} & A_{12} \\ A_{21} & A_{22} \end{bmatrix} = \frac{h}{1 - \nu_{xy}\nu_{yx}} \begin{bmatrix} E_x\beta_x & E_x\nu_{yx}\beta_y \\ E_y\beta_x\nu_{xy} & E_y\beta_y \end{bmatrix}, \tag{4.16}$$

where $\underline{\underline{\boldsymbol{A}}}$ is in general not symmetric.
The differential equation Eq. 4.15 can be solved for $w(x, y)$ once it is supplemented with boundary conditions. Analogously to Sec. 2, we use simply supported boundary conditions for w, i.e.

$$\begin{aligned} w|_{\partial\Omega} &= 0 \\ (n_x M_{xx} n_x + 2n_x M_{xy} n_y + n_y M_{yy} n_y)|_{\partial\Omega} &= 0 \quad \Rightarrow \quad w_{,xx}n_x|_{\partial\Omega} = 0, \quad w_{,yy}n_y|_{\partial\Omega} = 0 \end{aligned} \tag{4.17}$$

with $\underline{\boldsymbol{n}} = (n_x, n_y)^T$ the outward pointing unit normal. The corresponding strong form is given by

$$(\mathbf{S}) \begin{cases} \text{Given constants } a, b, E_x, E_y, \nu_{xy}, \nu_{yx}, G_{xy}, \lambda, q, \text{ and } \chi_M(x, y), \\ \text{Find } w \in C^4(\Omega), \text{ such that,} \\ D_{11}w_{,xxxx} + (2D_{12} + 2D_{66})w_{,xxyy} + D_{22}w_{,yyyy} = \\ -\lambda[(A_{11} + A_{12})w_{,xx} + (A_{21} + A_{22})w_{,yy}]\chi_M + q, \\ w|_{\partial\Omega} = 0, \quad w_{,xx}n_x|_{\partial\Omega} = w_{,yy}n_y|_{\partial\Omega} = 0 \end{cases} \tag{4.18}$$

The strong form (**S**) possesses the form of an eigenvalue problem if q is zero, with λ the eigenvalue indicating the amount of moisture content that can be added before buckling occurs. The corresponding eigenvector represents the transverse displacement field w.

4.2 Weak form

The weak form is required to solve (**S**) by the finite element method. Analogously to Sec. 2.4 we derive the weak form for the thin-plate model. Let $\phi \in H_0^2(\Omega)$ be a test function. Integrating Eq. 4.11 multiplied by ϕ over the domain, using partial integration, and Gauss' divergence theorem, we obtain

$$\begin{aligned}
&\int_\Omega \left(M_{xx}\phi_{,xx} + 2M_{xy}\phi_{,xy} + M_{yy}\phi_{,yy}\right) \mathrm{d}\Omega - \\
&\int_{\partial\Omega} \left(M_{xx}\phi_{,x}n_x + M_{yy}\phi_{,y}n_y\right) \mathrm{d}\Gamma \;= \\
&\int_\Omega \left(-q\phi + N_{xx}\phi_{,x}w_{,x} + N_{xy}(\phi_{,y}w_{,x} + \phi_{,x}w_{,y}) + N_{yy}\phi_{,y}w_{,y}\right) \mathrm{d}\Omega + \\
&\int_\Omega \left(\left(N_{xx,x} + N_{xy,y}\right)\phi w_{,x} + \left(N_{yy,y} + N_{xy,x}\right)\phi w_{,y}\right) \mathrm{d}\Omega.
\end{aligned} \tag{4.19}$$

Imposing simply supported boundary conditions (Eq. 4.17), assuming the in-plane body forces to be small ($N_{xx,x} + N_{xy,y} \approx 0$, $N_{yy,y} + N_{xy,x} \approx 0$), and substitution of Eq. 4.9, with $\underline{\boldsymbol{N}} = \underline{\boldsymbol{N}}^{(h)}$, given by Eq. 4.14, results in

$$\begin{aligned}
&\int_\Omega \left[(D_{11}w_{,xx} + D_{12}w_{,yy})\phi_{,xx} + 2D_{66}w_{,xy}\phi_{,xy} + (D_{12}w_{,xx} + D_{22}w_{,yy})\phi_{,yy}\right] \mathrm{d}\Omega = \\
&\int_\Omega \left[\lambda\left((A_{11} + A_{12})w_{,x}\phi_{,x} + (A_{21} + A_{22})w_{,y}\phi_{,y}\right)\chi_M + q\phi\right] d\Omega, \quad \forall\phi \in H_0^2(\Omega).
\end{aligned} \tag{4.20}$$

The resulting weak form problem is given by

$$(\mathbf{W}) \begin{cases}
\text{Given constants } a, b, E_x, E_y, \nu_{xy}, \nu_{yx}, G_{xy}, \lambda, q, \text{ and } \chi_M(x,y), \\
\text{Find } w \in H_0^2(\Omega) \text{ such that,} \\
\displaystyle\int_\Omega [(D_{11}w_{,xx} + D_{12}w_{,yy})\phi_{,xx} + 2D_{66}w_{,xy}\phi_{,xy} + (D_{12}w_{,xx} + D_{22}w_{,yy})\phi_{,yy}]\mathrm{d}\Omega = \\
\displaystyle\int_\Omega \left[\lambda\left((A_{11} + A_{12})w_{,x}\phi_{,x} + (A_{21} + A_{22})w_{,y}\phi_{,y}\right)\chi_M + q\phi\right] \mathrm{d}\Omega, \qquad \forall\phi \in H_0^2(\Omega).
\end{cases} \tag{4.21}$$

Discretization of the weak form (**W**) is done in a similar way as in Sec. 2.4. The domain Ω is rectangular, and therefore partitioned according to Eq. 2.25 in $N_e^x \times N_e^y$ rectangular elements $\Omega^e = (x_1, x_2) \times (y_1, y_2)$, where N_e^x represents the amount of elements along the $x-$axis and N_e^y that along the $y-$axis. The bijection between the element domain and the isoparametric domain (Eq. 2.28) is extended to a rectangular domain $(\xi, \eta) : \overline{\Omega}^e \to \mathcal{I}^2$ according to

$$(\xi, \eta) = \left(\frac{2}{|\Omega_1^e|}x - \frac{x_1 + x_2}{|\Omega_1^e|}, \frac{2}{|\Omega_2^e|}y - \frac{y_1 + y_2}{|\Omega_2^e|}\right), \tag{4.22}$$

with $|\Omega_1^e| = x_2 - x_1$, and $|\Omega_2^e| = y_2 - y_1$. The *Bogner-Fox-Schmit* element is used to approximate the transverse displacement w. This element contains 16 degrees of freedom, which are the values

of w, $w_{,x}$, $w_{,y}$, and $w_{,xy}$ at each node of Ω^e [22]. The *Bogner-Fox-Schmit* element is characterized by the tensor product of the cubic Hermite polynomial shape functions, resulting in

$$\underline{\boldsymbol{\mathcal{N}}}(\xi,\eta) = \begin{bmatrix} \mathcal{N}_{11}(\xi,\eta) \\ \mathcal{N}_{12}(\xi,\eta) \\ \mathcal{N}_{13}(\xi,\eta) \\ \mathcal{N}_{14}(\xi,\eta) \\ \mathcal{N}_{21}(\xi,\eta) \\ \mathcal{N}_{22}(\xi,\eta) \\ \mathcal{N}_{23}(\xi,\eta) \\ \mathcal{N}_{24}(\xi,\eta) \\ \mathcal{N}_{31}(\xi,\eta) \\ \mathcal{N}_{32}(\xi,\eta) \\ \mathcal{N}_{33}(\xi,\eta) \\ \mathcal{N}_{34}(\xi,\eta) \\ \mathcal{N}_{41}(\xi,\eta) \\ \mathcal{N}_{42}(\xi,\eta) \\ \mathcal{N}_{43}(\xi,\eta) \\ \mathcal{N}_{44}(\xi,\eta) \end{bmatrix} = \begin{bmatrix} \phi_{10}(\xi)\phi_{10}(\eta) \\ \phi_{11}(\xi)\phi_{10}(\eta) \\ \phi_{10}(\xi)\phi_{11}(\eta) \\ \phi_{11}(\xi)\phi_{11}(\eta) \\ \phi_{20}(\xi)\phi_{10}(\eta) \\ \phi_{21}(\xi)\phi_{10}(\eta) \\ \phi_{20}(\xi)\phi_{11}(\eta) \\ \phi_{21}(\xi)\phi_{11}(\eta) \\ \phi_{20}(\xi)\phi_{20}(\eta) \\ \phi_{21}(\xi)\phi_{20}(\eta) \\ \phi_{20}(\xi)\phi_{21}(\eta) \\ \phi_{21}(\xi)\phi_{21}(\eta) \\ \phi_{10}(\xi)\phi_{20}(\eta) \\ \phi_{11}(\xi)\phi_{20}(\eta) \\ \phi_{10}(\xi)\phi_{21}(\eta) \\ \phi_{11}(\xi)\phi_{21}(\eta) \end{bmatrix}, \tag{4.23}$$

with ϕ_{ij} given by Eq. 2.31. On each finite element Ω^e the transverse displacement field w_e is approximated by w_e^h, given by

$$\begin{aligned} w_e^h(x,y) &= \sum_{i=1}^{4} \left((\mathcal{N}_{i1} w_i + \frac{|\Omega_1^e|}{2}\mathcal{N}_{i2} w_{i,x} + \frac{|\Omega_2^e|}{2}\mathcal{N}_{i3} w_{i,y} + \frac{|\Omega_1^e||\Omega_2^e|}{4}\mathcal{N}_{i4} w_{i,xy}) \circ (\xi,\eta) \right)(x,y) \\ &= \langle (\underline{\boldsymbol{\mathcal{N}}}^e \circ (\xi,\eta))(x,y), \underline{\boldsymbol{W}}^e \rangle, \end{aligned} \tag{4.24}$$

with

$$\begin{aligned} \underline{\boldsymbol{\mathcal{N}}}^e &:= (\underline{\boldsymbol{\mathcal{N}}}_1^e, \underline{\boldsymbol{\mathcal{N}}}_2^e, \underline{\boldsymbol{\mathcal{N}}}_3^e, \underline{\boldsymbol{\mathcal{N}}}_4^e)^T, \\ \underline{\boldsymbol{\mathcal{N}}}_i^e &:= \left(\mathcal{N}_{i1}, (|\Omega_1^e|/2)\mathcal{N}_{i2}, (|\Omega_e^2|/2)\mathcal{N}_{i3}, (|\Omega_1^e||\Omega_2^e|/4)\mathcal{N}_{i4}\right)^T, \\ \underline{\boldsymbol{W}}^e &:= (\underline{\boldsymbol{W}}_1^e, \underline{\boldsymbol{W}}_2^e, \underline{\boldsymbol{W}}_3^e, \underline{\boldsymbol{W}}_4^e)^T, \\ \underline{\boldsymbol{W}}_i^e &:= (w_i, w_{i,x}, w_{i,y}, w_{i,xy})^T, \end{aligned} \tag{4.25}$$

$i \in \{1,2,3,4\}$. Using the *Bogner-Fox-Schmit* element in the weak form results in the following discretized system of equations

$$(\underline{\underline{\boldsymbol{K}}} - \lambda \underline{\underline{\boldsymbol{G}}})\underline{\boldsymbol{W}} = \underline{\boldsymbol{f}}, \tag{4.26}$$

of dimension $\tilde{N} = 4(N_e^x + 1)(N_e^y + 1)$. The constant λ represents a critical load parameter at which buckling occurs. It can be interpreted as the value of the increase in moisture content necessary to initiate buckling. The individual components at the element level of Eq. 4.26 are given by

$$
\begin{aligned}
\underline{\underline{\boldsymbol{K}}}^e &= \frac{|\Omega_1^e||\Omega_2^e|}{4}\int_{\mathcal{I}^2} \underline{\underline{\boldsymbol{S}}}^e \underline{\underline{\boldsymbol{D}}} (\underline{\underline{\boldsymbol{S}}}^e)^T \mathrm{d}\Omega \in \mathbb{R}^{16\times 16},\\
\underline{\underline{\boldsymbol{G}}}^e &= \begin{cases} \dfrac{|\Omega_1^e||\Omega_2^e|}{4}\displaystyle\int_{\mathcal{I}^2} \underline{\underline{\boldsymbol{L}}}^e \underline{\underline{\boldsymbol{A}}} (\underline{\underline{\boldsymbol{L}}}^e)^T \mathrm{d}\Omega \in \mathbb{R}^{16\times 16}, & \text{if } \Omega^e \in \Omega_M \\ \underline{\underline{\boldsymbol{O}}}_{16\times 16} & \text{otherwise} \end{cases}\\
\underline{\boldsymbol{f}}^e &= \frac{|\Omega_1^e||\Omega_2^e|}{4}\int_{\mathcal{I}^2} q\boldsymbol{\mathcal{N}}^e \mathrm{d}\Omega \in \mathbb{R}^{16},\\
\underline{\underline{\boldsymbol{S}}}^e &= \left(\frac{4}{|\Omega_1^e|^2}\boldsymbol{\mathcal{N}}^e_{,\xi\xi}, \frac{4}{|\Omega_2^e|^2}\boldsymbol{\mathcal{N}}^e_{,\eta\eta}, \frac{4}{|\Omega_1^e||\Omega_2^e|}\boldsymbol{\mathcal{N}}^e_{,\xi\eta}\right) \in \mathbb{R}^{16\times 3},\\
\underline{\underline{\boldsymbol{L}}}^e &= \left(\frac{2}{|\Omega_1^e|}\boldsymbol{\mathcal{N}}^e_{,\xi}, \frac{2}{|\Omega_2^e|}\boldsymbol{\mathcal{N}}^e_{,\eta}\right) \in \mathbb{R}^{16\times 2}.
\end{aligned}
\tag{4.27}
$$

The total system is obtained using the assembly operator

$$
\underline{\underline{\boldsymbol{K}}} = \mathop{\mathrm{A}}_{e=1}^{N_e^x\times N_e^y} \underline{\underline{\boldsymbol{K}}}^e, \qquad \underline{\underline{\boldsymbol{G}}} = \mathop{\mathrm{A}}_{e=1}^{N_e^x\times N_e^y} \underline{\underline{\boldsymbol{G}}}^e, \qquad \underline{\boldsymbol{f}} = \mathop{\mathrm{A}}_{e=1}^{N_e^x\times N_e^y} \underline{\boldsymbol{f}}^e, \qquad \underline{\boldsymbol{W}} = \mathop{\mathrm{A}}_{e=1}^{N_e^x\times N_e^y} \boldsymbol{W}^e. \tag{4.28}
$$

NOTE Eq. 4.24 does not satisfy the simply-supported boundary conditions. We follow the same strategy as in Sec. 2.4 and introduce $\mathcal{S}_w^h(\Omega) \subset H_0^2(\Omega)$ as the span of all globally defined basis functions without the span of the basis functions corresponding to the nodes located at the boundary. Numerically we partition the system and remove the equations that correspond to the nodes on $\partial\Omega$. Integration is achieved using the Gauss quadrature rule, explained in Sec. 2.6.2, to both in-plane directions. We use two Gauss points in both directions resulting in four Gauss points in total.

4.3 Validation

To validate the derived thin-plate finite element model we simplify the problem and compare the finite element solution with an analytical solution. Simplification is obtained by omitting the moisture-induced part, yielding

$$
D_{11}w_{,xxxx} + (2D_{12} + 2D_{66})w_{,xxyy} + D_{22}w_{,yyyy} = q. \tag{4.29}
$$

The analytical solution to Eq. 4.29 is given by the following Fourier series representation

$$
\begin{aligned}
w^{an}(x,y) &= \sum_{r\in\mathbb{O}}\sum_{s\in\mathbb{O}} w_{rs}\sin\left(\frac{r\pi x}{a}\right)\sin\left(\frac{s\pi y}{b}\right),\\
w_{rs} &= \frac{16q}{\pi^2 rs\left[D_{11}\left(\frac{r\pi}{a}\right)^4 + (2D_{12}+2D_{66})\left(\frac{r\pi}{a}\right)^2\left(\frac{s\pi}{b}\right)^2 + D_{22}\left(\frac{s\pi}{b}\right)^4\right]},
\end{aligned}
\tag{4.30}
$$

with $\mathbb{O}$ the set of all odd positive integers. For the validation of the model and the forthcoming results in Sec. 5 we use the fictive parameters given in Tab. 4.1:

Table 4.1: *Parameters used in validation process and during forthcoming simulations in Sec. 5.*

a [m]	b [m]	h [m]	q [N/m^2]	E_x [N/m^2]	E_y [N/m^2]	G_{xy} [N/m^2]
3	2	$5\cdot10^{-3}$	100	$8\cdot10^9$	$2\cdot10^9$	$2\cdot10^9$
ν_{xy} [-]	ν_{yx} [-]	β_x [-]	β_y [-]	N_e^x	N_e^y	N_{gauss}
0.3	0.075	$1\cdot10^{-4}$	$5\cdot10^{-4}$	30	30	4

For the mesh convergence study we use different mesh sizes. We neglect the moisture-induced contribution during the validation process, i.e. $\beta_x = \beta_y = 0$. The model is validated through a mesh convergence study based on the error $\|w^h - w^{an}\|_{L^2(\Omega)}$, with w^h the transverse displacement resulting from the finite element model, and w^{an} the analytical solution[1] given in Eq. 4.30. We use a square mesh of $N_e \times N_e$ elements in x and y direction, respectively, with $N_e = N_e^x = N_e^y$. Fig. 4.1 shows the error vs the amount of elements, and the corresponding deformed configuration using 32×32 elements.

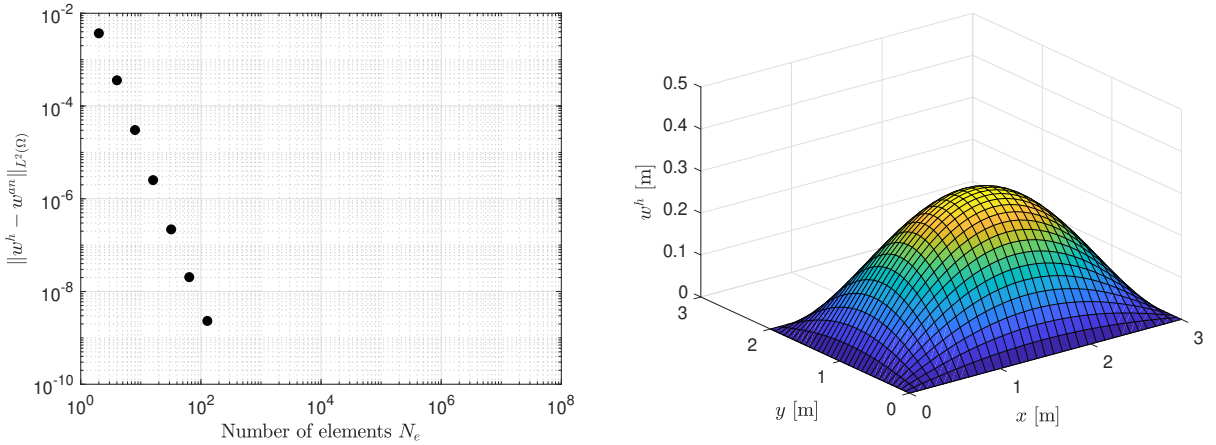

(a) *Error vs number of elements.*

(b) *Corresponding deformed configuration of a* 32×32 *mesh.*

Figure 4.1: *Validation of our model through mesh convergence study and an example of the deformed configuration.*

Fig. 4.1a shows the error vs number of elements in $x-$ or $y-$ direction. Fig. 4.1a shows that increasing one decade on the horizontal axis corresponds to approximately decreasing four decades on the vertical axis, i.e. $\|w^h - w^{an}\|_{L^2(\Omega)} \propto (1/N_e)^4$, which corresponds to the a priori error estimate of Ganesan and Tobiska [12]. Fig. 4.1b shows the corresponding deformed configuration of the finite element model for a mesh of 32×32. This mesh convergence study validates that the finite element model is working properly.

[1] For the analytical solution we use $r, s \in \{i \in \mathbb{O} \mid i \leq 1000\}$.

5 Results two-dimensional plate model

In this section we present some results of the two-dimensional plate model. First of all we show a typical result from a post-buckling simulation in Marc & Mentat. The detailed finite element implementation in Marc & Mentat is unknown, but it is based on a discretized form of the full *Föppl-Von-Kármán* equations (Eq. 4.11 and Eq. 4.12), according to de Böck et al. [1]. We present a typical result of an ordinary buckling analysis, or eigenvalue analysis, based on a thermomechanical analysis in Marc & Mentat. This ordinary eigenvalue analysis is not able to incorporate the transverse load and contact conditions. We show that the contact conditions and applied load affect the critical buckling load parameter, and hence must be accounted for during the eigenvalue analysis. The ordinary eigenvalue analysis should be extended such that it is capable of dealing with contact and applied pressure. This is achieved by considering the model as a cone constrained eigenvalue problem, and solve it using the SNA. We use the parameters given in Tab. 4.1 for all examples in this section.

5.1 Post-buckling simulation

We start with a typical result from a post-buckling simulation in Marc & Mentat. This simululation is performed with the current pre- and post-buckling model from Océ-Technologies B.V. in Marc & Mentat. This model initiates buckling via a small[1] random initial out-of-plane displacement. The post-buckling simulation uses free boundary conditions. The paper sheet is pushed to the printing surface (rigid foundation) using an applied pressure (transverse load), and rigid-body movements are suppressed via friction between the rigid foundation and the paper sheet. This post-buckling model is considered as an illustrative example only. Fig. 5.1a shows the initial configuration and the area having a change in moisture content, which is indicated with red dots. Fig. 5.1b shows the deformed configuration after performing a post-buckling simulation in Marc & Mentat.

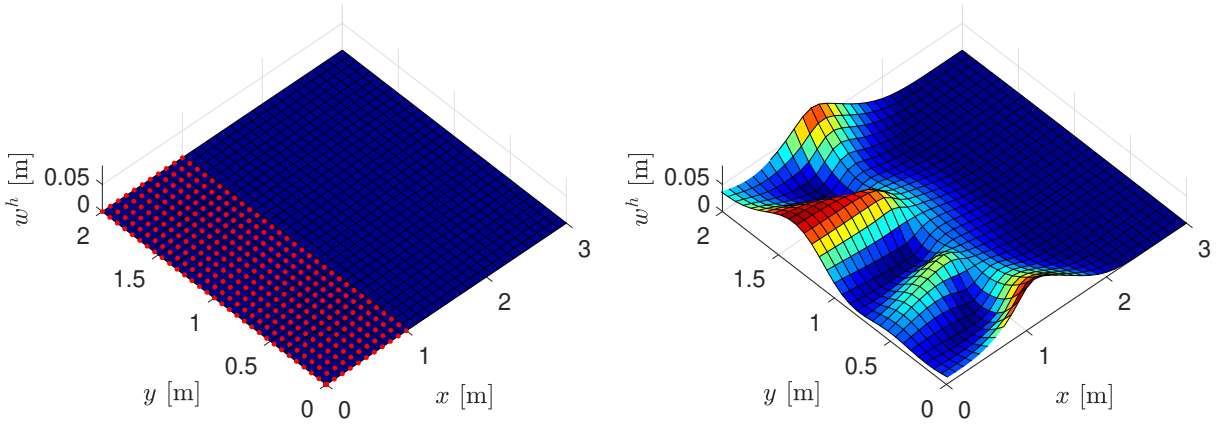

(a) *Initial configuration with moisture-affected area.* **(b)** *Deformed configuration.*

Figure 5.1: *Initial configuration with moisture-affected area, and corresponding deformed configuration after performing a post-buckling simulation in Marc & Mentat.*

The moisture-affected area tends to expand in the in-plane directions, but this expansion is restricted by the adjacent non-expanding area. This situation results in in-plane stresses, and from a certain threshold moisture content onwards the stresses become so large that it is energetically

[1] Small refers to random nodal values in the interval $[-1 \cdot 10^{-5}, 1 \cdot 10^{-5}]$.

more favourable to buckle in the out-of-plane direction. The deformed configuration of Fig. 5.1b shows that the cockling deformations mainly occur in the moisture-affected area. The major part of the area of the paper sheet without increase in moisture content remains undeformed. Only the strip next to the wetted region shows deformation (and even out-of-plane displacements). This post-buckling simulation is able to mimic the cockling process of a paper sheet subject to a moisture-affected area. The solution and simulation time depend strongly on the random initial out-of-plane displacement. The simulation time of this example is approximately 1200 seconds. Different techniques are sought to improve the robustness and simulation time of the currently available plate model in Marc & Mentat. In Sec. 3 we have shown that an ordinary eigenvalue analysis is a good method to tackle buckling problems. In the upcoming example we omit the contact conditions and the applied load and perform an eigenvalue analysis.

5.2 Eigenvalue analysis

In Sec. 3 we have shown that buckling can be modeled using an eigenvalue analysis. In this section we apply this technique to the two-dimensional plate model. The advantage of an eigenvalue analysis over the currently available post-buckling simulations in Marc & Mentat is that it does not need an initial disturbance, and no incremental approach. It can be performed in one increment, which reduces the simulation time. For this example we use the initial configuration and moisture-affected area shown in Fig. 5.1a. To suppress rigid body movements we fix all three displacement and rotational degrees of freedom of the corner node located at $(x, y) = (3, 0)$. We specify Marc & Mentat to return the first 100 eigenpairs as output of the simulation. The first and 28^{th} eigenvector are shown in Fig. 5.2.

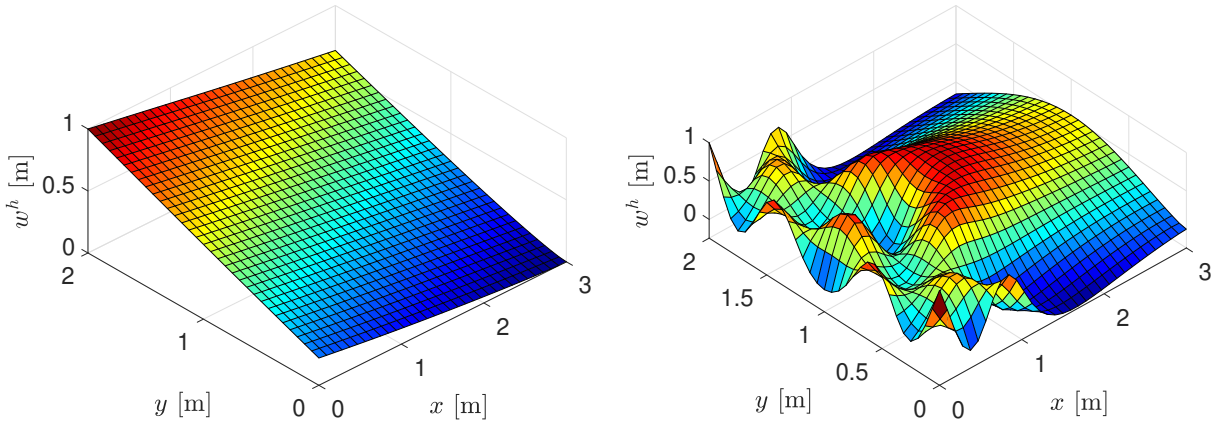

(a) *First eigenvector.* **(b)** *28^{th} eigenvector.*

Figure 5.2: *Example of two resulting eigenvectors from an eigenvalue analysis in Marc & Mentat for the initial configuration and moisture-affected area of Fig. 5.1a.*

Marc & Mentat orders the eigenpairs according to their eigenvalues in ascending order, i.e. the first eigenpair corresponds to the critical buckling load and buckling pattern. The simulation of the eigenvalue analysis resulting in 100 eigenpairs took approximately 4 seconds, which is approximately 150 times faster than the post-buckling simulation of Fig. 5.1. This is one of the advantages of an eigenvalue analysis compared to a post-buckling simulation. It also improves robustness, because the eigenvalue analysis does not require any initial disturbance to initiate the cockling process. When we examine the resulting eigenvectors we see no strong similarities between the eigenvectors of Fig. 5.2 and the post-buckling solution of Fig. 5.1.

Fig. 5.2a shows the resulting first eigenvector. We observe that this solution is different compared to the solution from a post-buckling simulation shown in Fig. 5.1b. One reason may be that the eigenpairs depend on the deformed pre-buckled state itself. The tangent stiffness matrix of a non-linear simulation (used for the eigenvalue analysis) changes if in-plane displacements occur in the pre-buckling regime. We performed multiple buckling analysis in successive increments (implying that the moisture content increases) to exclude this being the reason for the difference between Fig. 5.1b and Fig. 5.2a. The resulting eigenpairs in these successive increments were all the same. From this we can conclude that the in-plane displacements are sufficiently small in the pre-buckling regime, resulting in a constant tangent stiffness matrix in the pre-buckling regime, implying that the buckling analysis can be performed in the first increment.
Another reason for the difference between Fig. 5.2a and Fig. 5.1b may be the omission of contact and the transverse load.
Besides the first eigenpair we also obtain multiple higher-order eigenpairs. These eigenpairs are physically meaningless as the configuration will always buckle according to the first eigenpair. We take a look at the 28^{th} eigenvector shown in Fig. 5.2b to illustrate that an eigenvalue analysis is able to return a waviness pattern that resembles (in some way) the cockling process. We observe that this matches more closely to the post-buckling solution of Fig. 5.1b. It shows a waviness pattern which is also visible in the post-buckling simulation in Fig. 5.1b. Moreover, the location of the waviness pattern is in the moisture-affected area and the strip of non-wetted region next to it, as in Fig. 5.1b. The eigenvalues corresponding to the first and 28^{th} eigenvector are given by $\lambda \approx 1 \cdot 10^{-3}$ and $\lambda \approx 8.98 \cdot 10^{-1}$, respectively. An eigenvalue $\lambda = 1$ (100%) corresponds to an area only consisting of water (which is physically not possible). The resulting eigenvalues imply that if the moisture-affected area consists of 0.1% water we obtain the deformed configuration of Fig. 5.2a, and if 89.8% of the moisture-affected area consists of water we obtain the deformed configuration of Fig. 5.2b. Based on the results of Fig. 5.2 we conclude that performing an ordinary eigenvalue analysis is inadequate to mimic the cockling process. Nevertheless, performing an eigenvalue analysis improves the simulation time significantly. Therefore we further explore the idea of an eigenvalue analysis.

5.3 Influence of transverse load and contact

In this section we show that the critical load parameter varies for different applied transverse loads (pressures) in combination with contact boundary conditions. To do so we consider the current post-buckling simulations in Marc & Mentat. For these simulations we use the same parameters, random initial out-of-plane displacement, and moisture-affected area as is used for the result of Fig. 5.1b. We perform ten times a post-buckling simulation with a different applied pressure, but keep the other parameters the same. The critical load parameter is determined approximately for each simulation, as a post-buckling simulation does not explicitely return the critical load parameter. We also want to show that the simulation times vary in an arbitrary way for different applied pressures. For comparison of the results we normalize the simulation time and critical load parameter. We divide the simulation time of each simulation by the maximum simulation time of all simulations. The critical load parameter of each simulation is divided by the maximum critical load parameter of all simulations. The results are shown in Fig. 5.3.

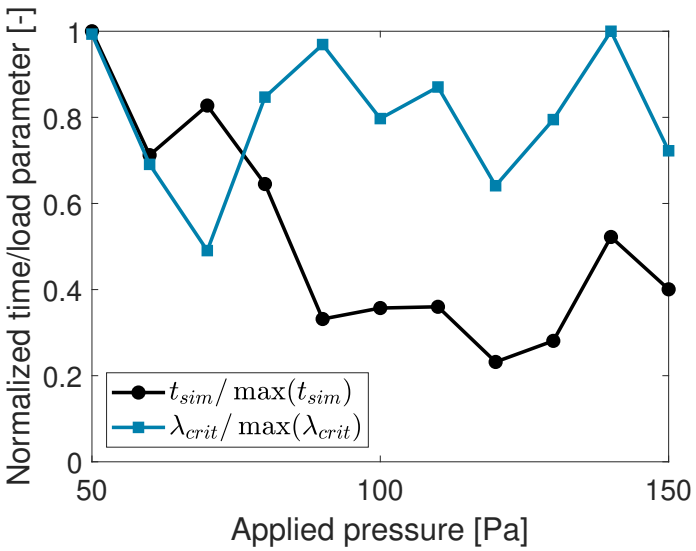

Figure 5.3: *Influence of applied pressure on critical load parameter, and corresponding normalized simulation times.*

Fig. 5.3 shows that the maximum simulation time is reached for the simulation with 50 Pa. The maximum critical load parameter is reached for the simulation with 140 Pa. Océ-Technologies B.V. already experienced that simulation time varies arbitrarily for different initial parameters. The results of Fig. 5.3 confirm this for different initial applied loads. We would expect that the critical load parameter increases with increasing applied pressure, which is contradictory to the results of Fig. 5.3, since it varies arbitrarily for increasing applied pressure. A reason for this may be the combination of contact, applied pressure and initial random out-of-plane displacement. More nodes are in contact when the pressure increases, which affects the contact conditions, and eventually the critical load parameter. If the applied pressure is drastically increased to 2000 Pa we observe no cockling deformations at all.
If the applied pressure is increased from 70 Pa to 80 Pa (which is assumed to be small) it results in an increase in critical load parameter of approximately 22% percent, which is considered to be large. Moreover, the critical load parameter for an applied pressure of 50 Pa is approximately the same as the critical load parameter for an applied pressure of 140 Pa. This implies that the buckling threshold value is the same for both simulations, even if the applied pressure is almost three times larger, which is questionable. Due to these observations we should not take the results of the post-buckling simulations for granted. Since the applied transverse load is the only input parameter that changes in the results of Fig. 5.3 we may conclude that it affects the critical load parameter. This implies that an ordinary eigenvalue analysis is not sufficient to determine the critical eigenpair.

5.4 Cone constrained eigenvalue problem

The theory of a cone constrained eigenvalue problem from Sec. 3.3 is applied to the two-dimensional plate model. The discretized weak form used for the SNA[1] is given by Eq. 4.26. We concluded in Sec. 3.3.3 that the SNA for a cone constrained eigenvalue problem with transverse load is plausible, yet not correct due to the combination of the transverse load and normalization condition. For more details we refer to Sec. 3.3.
Nevertheless we apply the SNA to the two-dimensional plate model. We follow the same strategy as

[1]The same theory on the cone constrained eigenvalue problem holds, but with corresponding dimensions.

in Sec. 3.3 by using an eigenvector of the ordinary eigenvalue problem $(\underline{\underline{\boldsymbol{K}}} - \lambda \underline{\underline{\boldsymbol{G}}})\underline{\boldsymbol{W}} = \underline{\mathbf{0}}_{\tilde{N}}$. Because no theoretical results are available on which eigenvector to choose as initial guess we just choose at random the 7^{th} eigenvector. Fig. 5.4a shows the eigenvector with corresponding eigenvalue and moisture-affected area. Fig. 5.4b shows the same eigenvector in three dimensional space.

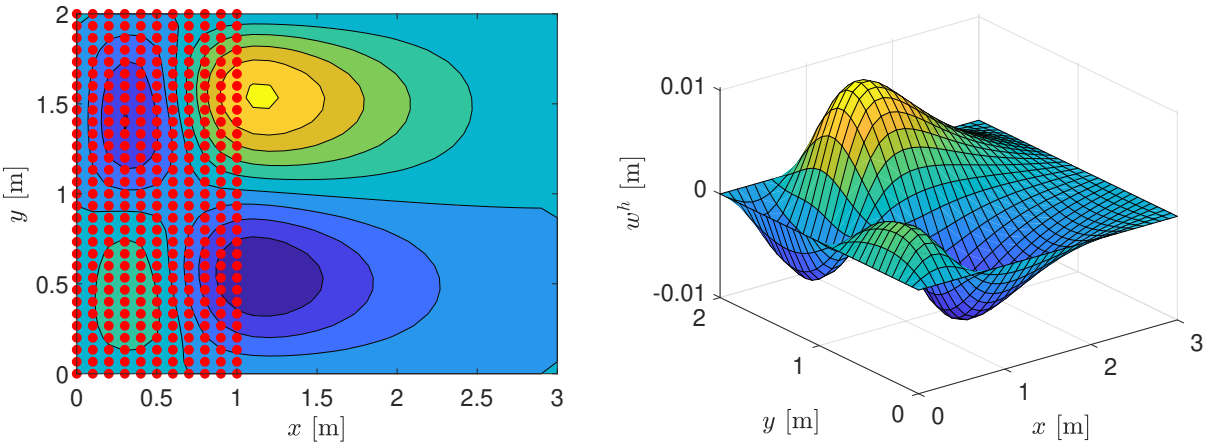

(a) *7^{th} eigenvector with $\lambda = 4.74 \cdot 10^{-1}$, and moisture-affected area.*

(b) *7^{th} eigenvector with $\lambda = 4.74 \cdot 10^{-1}$.*

Figure 5.4: *The 7^{th} eigenvector corresponding to the moisture-affected area (indicated with red dots), used as input to the SNA.*

The eigenvalue $\lambda = 4.74 \cdot 10^{-1}$ indicates that if the moisture-affected area consists of 47.4% water it buckles into the deformed configuration of Fig. 5.4b. The eigenvector and corresponding eigenvalue from Fig. 5.4 are used as initial guess to the SNA. In Sec. 3 we concluded that the Fischer-Burnmeister complementarity function possesses the best performance, and therefore we use it as complementarity function in the SNA for the two-dimensional plate model. Fig. 5.5 shows the resulting Pareto eigenvector.

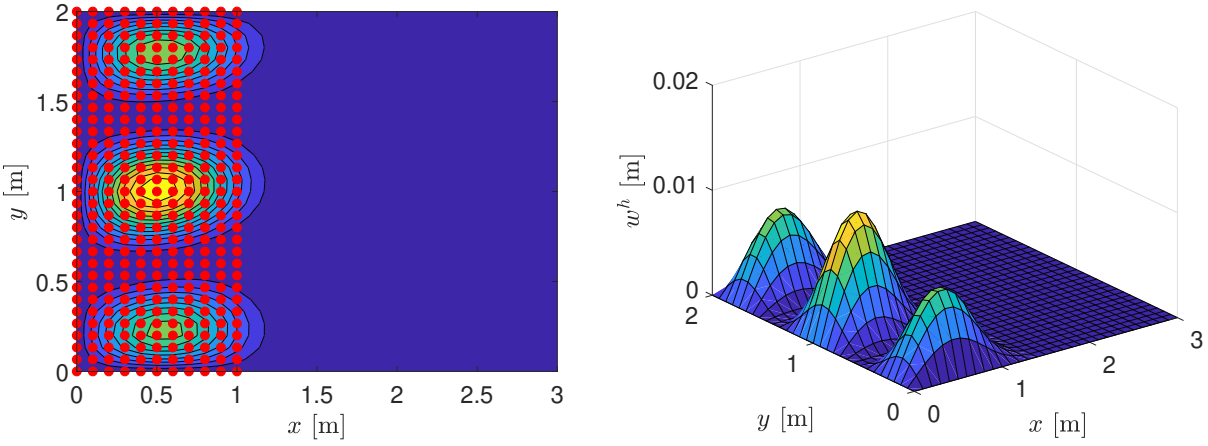

(a) *Resulting Pareto eigenvector.*

(b) *Resulting Pareto eigenvector.*

Figure 5.5: *The resulting Pareto eigenvector from the SNA supplemented with the Fischer-Burnmeister complementarity function, with Pareto eigenvalue $\lambda = 4.72 \cdot 10^{-1}$*

First of all we observe that the resulting Pareto eigenvector satisfies the contact boundary condi-

tions as it only contains non-negative components, see Fig. 5.5. We see a certain cockling pattern in the moisture-affected area, just as in the post-buckling simulation in Fig. 5.1b. We observe that the cockling pattern does not look similar to the cockling pattern of the post-buckling simulation. One reason is that our model assumes simply-supported boundary conditions[1], whereas the paper sheet in the post-buckling simulations is free. In Sec. 3 we concluded that a new scalar condition is necessary as a replacement for the normalizaton condition due to the applied transverse load. This also holds if we apply the SNA to the plate model. The solution depends on the normalization condition. At the moment we normalize the solution with $\langle \underline{\mathbf{1}}_m, \underline{\boldsymbol{w}}_c \rangle = c^*$, with $c^* = 1$. Upon changing the constant c^*, we find a different eigenpair. This shows that the SNA is not working properly yet. Nevertheless we obtained a solution that satisfies the non-penetration constraint and the corresponding buckling pattern could be a plausible solution.
The SNA requires an initial guess, which can be interpreted as an initial disturbance necessary for the post-buckling simulations. Both the SNA and the post-buckling simulations show that the resulting deformed configuration strongly depends on the initial guess/disturbance. Besides the initial guess to the SNA we also have different options available for the choice of the complementarity function. The choice of the complementarity function influences the solution. This is illustrated by performing the same simulation as was used for the results of Fig. 5.5, but with the lattice complementarity function instead of the Fischer-Burnmeister complementarity function. The resulting Pareto eigenvector is shown in Fig. 5.6.

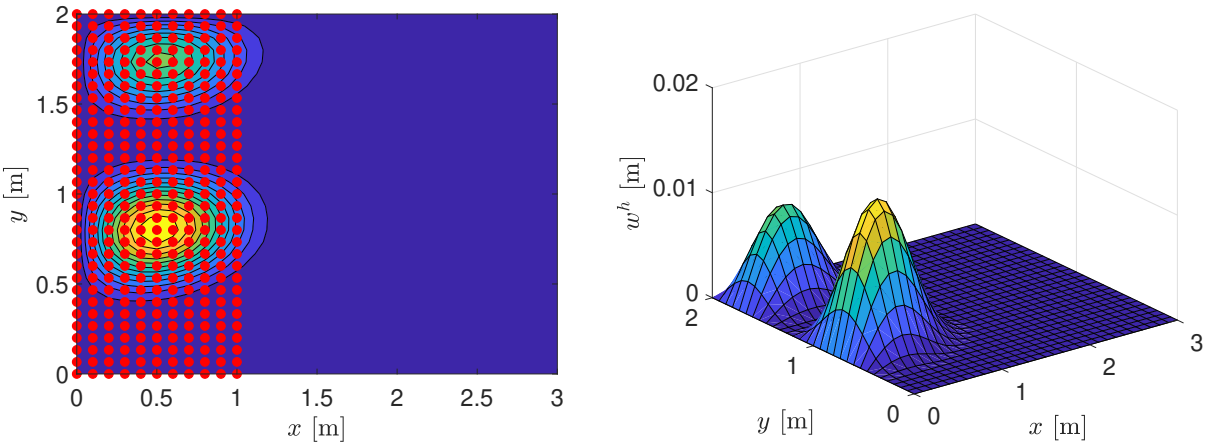

(a) *Resulting Pareto eigenvector.*

(b) *Resulting Pareto eigenvector.*

Figure 5.6: *The resulting Pareto eigenvector from the SNA with the lattice complementarity function, with Pareto eigenvalue* $\lambda = 4.23 \cdot 10^{-1}$

Comparing Fig. 5.5 with Fig. 5.6 shows that a different complementarity function results in a different Pareto eigenpair. Moreover, the same simulation with the Evtushenko-Purtov complementarity function resulted in no convergence after 2000 iterations. We conclude that robustness is not necessarily improved by performing the SNA to the plate model compared to the post-buckling simulations.
Besides robustness we are also interested in simulation time. The post-buckling simulations with different applied pressures from Fig. 5.3 have an average simulation time of 1763 seconds. Since the simulation time for the results of Fig. 5.5 and Fig. 5.6 is 8 seconds and 7 seconds, we conclude that if the SNA converges it performs better than the post-buckling simulations, regarding simulation time.

[1]Since our model serves as illustrative example of a Pareto eigenvalue problem we use analogously to Sec. 2 simply-supported boundary conditions.

6 Concluding remarks

Océ-Technologies B.V. developed a finite element model in Marc & Mentat, which is able to mimic the cockling process of a (partially) wetted paper sheet that is fixed to the printing table using suction. They use a small random initial out-of-plane displacement to trigger the cockling process. This random initial out-of-plane displacement induces some correlation between the initial and final sheet shape, which is a disadvantage. Moreover, it affected the robustness and simulation time of the model.

One of the goals of this thesis was to improve robustness and simulation time of the model created by Océ-Technologies B.V.. Another question was how to qualify the paper sheet subjected to contact conditions and applied pressure (suction) as a buckling simulation, since a buckling simulations allows us to determine the critical amount of moisture at which buckling occurs. Océ-Technologies B.V. was particularly interested in this value. To answer these questions we extracted the difficult parts of the two-dimensional plate model from Marc & Mentat. These difficult parts refer to buckling and contact.

A simplified one-dimensional finite element beam model is developed in MATLAB. This model was used to investigate the buckling and contact phenomena solely as well as jointly.
Buckling is governed by an eigenvalue problem, and therefore solved using an eigenvalue analysis. An eigenvalue analysis is preferred over a post-buckling simulation, since it does not need an initial disturbance to trigger buckling. Moreover, it gave similar results as post-buckling simulations of beams with a random initial transverse displacement. It is a robust method to find the buckling load parameter and buckling pattern.

Contact is a non-linear condition since the contact area is unknown beforehand. Contact can be implemented using different techniques. We chose the penalty method, as this is the most widely used technique to implement contact conditions. A post-buckling simulation of the one-dimensional beam model subjected to contact conditions and a transverse load resulted in convergence problems, both in our model and in the Marc & Mentat model. From this we concluded that a post-buckling simulation subject to contact conditions must be considered as difficult. We searched for another method that is capable of incorporating contact and buckling. Since we wanted to stick to the idea of an eigenvalue problem we came up with a so-called *cone constrained eigenvalue problem*.

The cone is considered to be the non-negative orthant, which turned the cone constrained eigenvalue problem into a *Pareto* eigenvalue problem. With the *Pareto* eigenvalue problem formulation we where able to include the contact constraint. A semi-smooth Newton algorithm (SNA) was used to solve the cone constrained eigenvalue problem. However, incorporating the transverse load (applied pressure) in the cone constrained eigenvalue problem description resulted in problems. The normalization condition, present in the SNA, is invalid if a transverse load is present because it affects the solution. Nevertheless, we saw that the results satisfied the non-negativity constraint, and that the deformed configurations were plausible solutions. Due to this we considered the SNA applied to a cone constrained eigenvalue problem as a plausible, yet so far incorrect replacement for the post-buckling model subject to contact conditions.

For the two-dimensional plate model we derived a simplified equilibrium equation, which describes the out-of-plane displacements in the pre-buckling regime. The equilibrium equation was discretized and implemented in MATLAB.
Then we turned to the results for the two-dimensional plate model. We first analyzed a post-buckling simulation from the current model in Marc & Mentat. The post-buckling model in Marc

& Mentat is based on the full *Föppl-Von-Kármán* equations. The result was a configuration with a possible cockling pattern, but needed a long simulation time. We followed the same approach as we did with the one-dimensional beam model and performed an eigenvalue analysis in Marc & Mentat on the plate model without applied pressure and contact. The simulation time of the eigenvalue analysis was significantly lower compared to a post-buckling simulation. The resulting eigenvectors were not similar to the solution of a post-buckling simulation, which was probably caused by omission of the applied pressure and contact conditions. We investigated the influence of the applied pressure in combination with contact conditions and a random initial out-of-plane displacement on the critical load parameter. We concluded that the applied pressure in combination with contact and an initial random out-of-plane displacement affects the critical load parameter. This result also shows the lack of robustness of the post-buckling model in Marc & Mentat.

Eventually, we considered the simplified MATLAB model as a cone constrained eigenvalue problem. The examples showed plausible deformed configurations resulting from the SNA. These results are incorrect because of the issue with the normalization condition in combination with the transverse load. Performing the SNA did not improve robustness significantly as it strongly depends on the initial guess and the choice of complementarity function. The simulation time of the SNA is significantly improved (if it converges) compared to the simulation time of a post-buckling simulation.

7 Recommendations

Due to time constraints we still have some unanswered questions. The most important topic for further research is how to make the SNA applicable. One possible option is to follow Shahwan and Waas [23], who replaced the contact conditions by a non-linear spring. This idea could be exploited, such that the non-linear spring term also incorporates the transverse load in it. Using a (non-linear) spring does not generate an external vector as it is incorporated in the (tangent) stiffness matrix itself. Eigenvalue analysis techniques can be used on a linearized version of this non-linear system to obtain the critical eigenpair. Following this route brings also disadvantages. First of all a (non-linear) spring relation should be found between the applied pressure, the transverse displacement and the contact conditions. The non-linear spring term possibly contains a jump between the contact and no contact condition, which results in a non-smooth spring term. This may result in numerical issues when the non-linear system is solved.

The problem with the normalization condition should be resolved if we want to remain to the SNA for the Pareto eigenvalue problem. The normalization condition should be replaced by a scalar condition that demands a non-zero solution and is capable of incorporating the transverse load in it. The first question is if such a condition even exists.
If such a condition may be found it is recommended to look in more detail at the choice of the initial guess of the SNA. Until now we used an eigenvector of the ordinary eigenvalue problem, because no theoretical results are available on how to choose the initial guess.
Furthermore, we have shown that the choice of the complementarity function affects the result of the SNA. We also recommend to find theoretical results on how to choose the complementarity function.

Our beam model is valid for small displacements and moderately large rotations. If one wants to explore the post-buckling regime in more detail we recommend to follow Vaz and Silva [6]. They include higher order terms, which are necessary to correctly describe the post-buckling regime. This idea can be extended to the two-dimensional plate model, implying that the full *Föppl-Von-Kármán* equations should be solved for, as in [1].
Finally we assume in our research that in-plane body forces (Eq. 4.12) are negligibly small, but this assumption might not be justified. For further research we recommend to include the in-plane displacement field in the equilibrium equations, and eventually solve the full *Föppl-Von-Kármán* equations.

References

[1] de Böck, R., van de Ven, A.A.F., Saes, L.H., Maubach, J.M.L., Koren, B. (2017). Moisture-induced buckling of paper sheets, analysis and simulation. In *International Journal of Solids and Structures*, **128**, 296-308, doi:10.1016/j.ijsolstr.2017.08.038

[2] Cerda, E., Mahadevan, L. (2003). Geometry and Physics of Wrinkling. In *Physical Review Letters*, **90**(7), doi:10.1103/PhysRevLett.90.074302

[3] Leppänen, T., Sorvari, J., Erkkilä, A-L., and Hämäläinen, J. (2005). Mathematical modelling of moisture induced out-of-plane deformation of a paper sheet. In *Modelling and Simulation in Materials Science and Engineering*, **13**(6), 841-850, doi:10.1088/0965-0393/13/6/004

[4] Crawford, J. D. (1991). Introduction to bifurcation theory. In *Reviews of Modern Physics*, **63**(4), 991-1037, doi:10.1103/RevModPhys.63.991

[5] Şimşek, M., Yurtcu, H. H. (2013). Analytical solutions for bending and buckling of functionally graded nanobeams based on the nonlocal Timoshenko beam theory. In *Composite Structures*, **97**, 378-386, doi:10.1016/j.compstruct.2012.10.038

[6] Vaz, M. A., Silva, D. F. C. (2003). Post-buckling analysis of slender elastic rods subjected to terminal forces. In *International Journal of Non-Linear Mechanics*, **38**(4), 483-492, doi:10.1016/S0020-7462(01)00072-5

[7] Menzala, P.G., Zuazua, E. (1999). The beam equation as a limit of a 1-D nonlinear von Kármán model. In *Applied Mathematics Letters*, **12**(1), 47-52, doi:10.1016/S0893-9659(98)00125-6

[8] Howell, J. S., Toundykov, D., Webster, J. T. (2018). A Cantilevered Extensible Beam in Axial Flow: Semigroup Well-posedness and Postflutter Regimes. In *SIAM Journal on Mathematical Analysis*, **50**(2), 2048 - 2085, doi:10.1137/17M1140261

[9] Jam, J. E., Noorabadi, M., Namdaran, N. (2017). Nonlinear free vibration analysis of microbeams resting on viscoelastic foundation based on the modified couple stress theory. In *Archive of Mechanical Engineering*, **64**(2), 239-256, doi:10.1515/meceng-2017-0015

[10] Kundu, B. Ganguli, R. (2017). Analysis of weak solution of Euler-Bernoulli beam with axial force. In *Applied Mathematics and Computation*, **298**, 247-260, doi:10.1016/j.amc.2016.11.019

[11] Komkov, V. (1983) Euler's buckling formula and Wirtinger's inequality. In *International Journal of Mathematical Education in Science and Technology*, **14**(6), 661-668, doi:10.1080/0020739830140601

[12] Ganesan, S., Tobiska, L. (2017). *Finite Elements: Theory and Algorithms.* Cambridge University Press

[13] Wriggers, P. (2006). *Computational Contact Mechanics.* Second Edition, Springer-Verlag Berlin Heidelberg

[14] Konyukhov, A. Izi, R. (2015). *Introduction to Computational Contact Mechanics: A Geometrical Approach.* John Wiley & Sons

[15] Brunk, D.H., Mitchell, L. D. (1983). An analysis of an Euler-Bernoulli beam-column with arbitrary initial crookedness by transfer matrix methods. In *Computers & Structures*, **16**(1-4), 415 - 421, doi:10.1016/0045-7949(83)90180-3

[16] Adly, S. Seeger, A. (2011). A nonsmooth algorithm for cone-constrained eigenvalue problems. In *Computational Optimization and Applications*, **49**(2), 299-318, doi:10.1007/s10589-009-9297-7

[17] Changfeng, M. (2012). The semismooth and smoothing Newton methods for solving Pareto eigenvalue problem. In *Applied Mathematical Modelling*, **36**(1), 279–287, doi:10.1016/j.apm.2011.05.045

[18] Sio, J. F. A. Pinto da Costa, A., Simões, F. M. F. (2016). Buckling of unilaterally constrained columns by complementarity eigenvalue analyses. In *International Journal of Solids and Structures*, **106-107**, 46-55, doi:10.1016/j.ijsolstr.2016.11.032

[19] Thornton, E.A. (1993). Thermal Buckling of Plates and Shells. In *Applied Mechanics Reviews*, **46**(10), 485-506, doi:10.1115/1.3120310

[20] Murphy, K. D., Ferreira, D. (2001). Thermal buckling of rectangular plates. In *International Journal of Solids and Structures*, **38**, 3979-3994, doi:10.1016/S0020-7683(00)00240-7

[21] Timoshenko, S. Gere J.S. (1961). *Theory of Elastic Stability.* Second edition, McGraw-Hill.

[22] Chien, C.-S., Shih, Y.-T. (2009). A cubic Hermite finite element-continuation method for numerical solutions of the von Kármán equations. In *Applied Mathematics and Computation*, **209**(2), 356-368, doi:10.1016/j.amc.2008.12.054

[23] Shahwan, K. W., Waas, A. M. (1994). A mechanical model for the buckling of unilaterally constrained rectangular plates. In *International Journal of Solids and Structures*, **31**(1), 75-87, doi:10.1016/0020-7683(94)90176-7

[24] de Souza Neto, E.A., Feng Y.T. (1999). On the determination of the path direction for arc-length methods in the presence of bifurcations and 'snap-backs'. In *Computer Methods in Applied Mechanics and Engineering*, **179**(1-2), 81-89, doi:10.1016/S0045-7825(99)00042-0

[25] Feng, Y.T., Perić, D., Owen, D.R.J. (1995). Determination of travel directions in path-following methods. In *Mathematical and Computer Modelling*, **21**(7), 43-59, doi:10.1016/0895-7177(95)00030-6

[26] Feng, Y.T., Perić D., Owen D.R.J. (1996). A new criterion for determination of initial loading parameter in arc-length methods. In *Computers & structures*, **58**(3), 479-485, doi:10.1016/0045-7949(95)00168-G

[27] Fafard, M., Massicotte, B. (1993). Geometrical interpretation of the arc-length method. In *Computers & Structures*, **46**(4), 603-615, doi:10.1016/0045-7949(93)90389-U

[28] de Böck, R. (2015). *Moisture-induced buckling of paper sheets.* (Master's thesis), Retrieved from: https://pure.tue.nl/ws/portalfiles/portal/46923200/840210-1.pdf

A Global shape functions

Global shape functions refer to shape functions defined over the global domain Ω. The linear Lagrange polynomial shape functions of Eq. 2.29 are extended to the global domain, using $\Psi_i : \Omega \to \mathbb{R}$, defined as

$$\begin{aligned}
\Psi_1 &= \begin{cases} (\psi_1 \circ \xi)(x) & \text{if } x \in \Omega^1, \\ 0 & \text{otherwise,} \end{cases} \\
\Psi_i &= \begin{cases} (\psi_2 \circ \xi)(x) & \text{if } x \in \Omega^{i-1}, \\ (\psi_1 \circ \xi)(x) & \text{if } x \in \Omega^i, \\ 0 & \text{otherwise,} \end{cases} \qquad \forall i \in \{2, 3, ..., N-1\}, \\
\Psi_N &= \begin{cases} (\psi_2 \circ \xi)(x) & \text{if } x \in \Omega^{N-1}, \\ 0 & \text{otherwise.} \end{cases}
\end{aligned} \tag{A.1}$$

To satisfy the boundary condition $u|_{x=0} = 0$ we define the discrete test/solution space as

$$\mathcal{S}_u^h(\Omega) := \text{span}\{\Psi_i\}_{i=1}^N \setminus \text{span}\{\Psi_1\} \subset \mathcal{S}_u(\Omega). \tag{A.2}$$

The cubic Hermite polynomial shape functions of Eq. 2.31 are also extended to the global domain, using $\Phi_i : \Omega \to \mathbb{R}$, defined as

$$\begin{aligned}
\Phi_1 &= \begin{cases} (\phi_{10} \circ \xi)(x) & \text{if } x \in \Omega^1, \\ 0 & \text{otherwise,} \end{cases} \\
\Phi_2 &= \begin{cases} (\phi_{11} \circ \xi)(x) & \text{if } x \in \Omega^1, \\ 0 & \text{otherwise,} \end{cases} \\
\Phi_{2i-1} &= \begin{cases} (\phi_{20} \circ \xi)(x) & \text{if } x \in \Omega^{i-1}, \\ (\phi_{10} \circ \xi)(x) & \text{if } x \in \Omega^i, \\ 0 & \text{otherwise,} \end{cases} \qquad \forall i \in \{2, 3, ..., N-1\}, \\
\Phi_{2i} &= \begin{cases} (\phi_{21} \circ \xi)(x) & \text{if } x \in \Omega^{i-1}, \\ (\phi_{11} \circ \xi)(x) & \text{if } x \in \Omega^i, \\ 0 & \text{otherwise,} \end{cases} \qquad \forall i \in \{2, 3, ..., N-1\}, \\
\Phi_{2N-1} &= \begin{cases} (\phi_{21} \circ \xi)(x) & \text{if } x \in \Omega^{N-1}, \\ 0 & \text{otherwise,} \end{cases} \\
\Phi_{2N} &= \begin{cases} (\phi_{20} \circ \xi)(x) & \text{if } x \in \Omega^{N-1}, \\ 0 & \text{otherwise.} \end{cases}
\end{aligned} \tag{A.3}$$

To satisfy the boundary condition $w|_{\partial\Omega} = 0$ we define the discrete test/solution space as

$$\mathcal{S}_w^h(\Omega) := \text{span}\{\Phi_i\}_{i=1}^{2N} \setminus \text{span}\{\Phi_1, \Phi_{2N-1}\} \subset \mathcal{S}_w(\Omega). \tag{A.4}$$

B Arc-length method

Newton's method solves the non-linear system given an incremental load $\Lambda^{(t)}$, but fails in following the correct solution path at and beyond the bifurcation point. Using Newton's method it is not possible to decrease the load parameter $\Lambda^{(t)}$, because $\Lambda^{(t)}$ is given. Therefore the arc-length method is used, which introduces an unknown update to the load factor:

$$\Delta\Lambda_{k+1} = \Delta\Lambda_k + \delta\Lambda_k \tag{B.1}$$

The $\Delta\Lambda_k$ term in Eq. B.1 is the incremental load factor at iteration k and $\delta\Lambda$ is the unknown update to this incremental load factor. The arc-length method solves the same system of equations as Newton's method, but introduces one additional constraint [24]:

$$\langle \Delta\underline{\boldsymbol{\Upsilon}}, \Delta\underline{\boldsymbol{\Upsilon}} \rangle = \ell^2, \tag{B.2}$$

with ℓ^2 a prescribed arc-length. This constraint requires the Euclidean norm of $\Delta\underline{\boldsymbol{\Upsilon}}$ to be equal to the arc-length ℓ, i.e. the converged incremental update lies at the intersection between the solution path and a ball of radius ℓ. An illustration of this for a one degree-of-freedom system is shown in Fig. B.1.

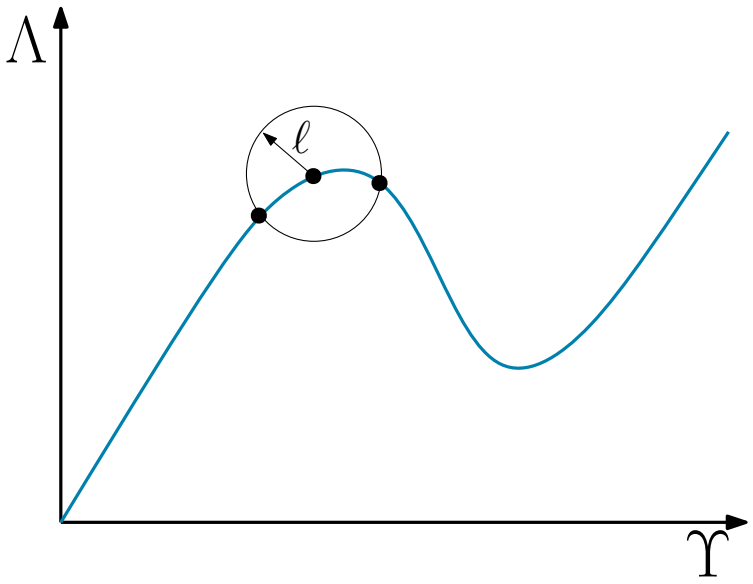

Figure B.1: *Illustration of the arc-length method via an example of an one degree-of-freedom system*

Combining the additional constraint of Eq. B.2 with Newton's method results in the following system of equations:

$$\begin{bmatrix} \underline{\underline{\boldsymbol{T}}}(\underline{\boldsymbol{\Upsilon}}_k, \Delta\Lambda_k) & -\underline{\boldsymbol{f}}_{ex}(\underline{\boldsymbol{\Upsilon}}_k, \Delta\Lambda_k) \end{bmatrix} \begin{bmatrix} \delta\underline{\boldsymbol{\Upsilon}}_k \\ \delta\Lambda_k \end{bmatrix} = -\underline{\boldsymbol{R}}(\underline{\boldsymbol{\Upsilon}}_k, \Delta\Lambda_k), \tag{B.3}$$

$$\langle \Delta\underline{\boldsymbol{\Upsilon}}_{k+1}, \Delta\underline{\boldsymbol{\Upsilon}}_{k+1} \rangle = \ell^2, \tag{B.4}$$

where the incremental superscript is omitted for readability. *NOTE*, the residual is now a function of $\underline{\boldsymbol{\Upsilon}}_k$ and $\Delta\Lambda_k$. Using Eq. B.3 makes it possible to derive an expression for the updated incremental solution vector:

$$\delta\underline{\boldsymbol{\Upsilon}}_k = \delta\underline{\boldsymbol{\Upsilon}}_k^I + \delta\Lambda_k \delta\underline{\boldsymbol{\Upsilon}}_k^{II}, \tag{B.5}$$

with $\delta\underline{\boldsymbol{\Upsilon}}_k^I$ the iterative displacement resulting from Newton's method, and $\delta\underline{\boldsymbol{\Upsilon}}_k^{II}$ the so-called *tangential solution*, given by [24]

$$\begin{aligned}\delta\underline{\boldsymbol{\Upsilon}}_k^I &= -\underline{\underline{\boldsymbol{T}}}^{-1}(\underline{\boldsymbol{\Upsilon}}_k, \Delta\Lambda_k)\underline{\boldsymbol{R}}(\underline{\boldsymbol{\Upsilon}}_k, \Delta\Lambda_k),\\ \delta\underline{\boldsymbol{\Upsilon}}_k^{II} &= \underline{\underline{\boldsymbol{T}}}(\underline{\boldsymbol{\Upsilon}}_k, \Delta\Lambda_k)^{-1}\underline{\boldsymbol{f}}_{ex}(\underline{\boldsymbol{\Upsilon}}_k, \Delta\Lambda_k).\end{aligned} \tag{B.6}$$

Different arc-length methods are available to determine the corresponding correct solution path and obtain the correct solution. Here we consider in particular *Crisfield's* arc-length method, and the *modified Riks-Wempner* arc-length method.

B.1 Crisfield's arc-length method

Crisfield's arc-length method is based upon solving a quadratic equation in $\delta\Lambda$ to obtain the correct solution. Substitution of Eq. B.5 in the relation $\Delta\underline{\boldsymbol{\Upsilon}}_{k+1} = \Delta\underline{\boldsymbol{\Upsilon}}_k + \delta\underline{\boldsymbol{\Upsilon}}_k$, and including the constraint of Eq. B.4 results in the quadratic equation

$$c_1\delta\Lambda_k^2 + c_2\delta\Lambda_k + c_3 = 0 \tag{B.7}$$

with

$$\begin{aligned}c_1 &= \langle\delta\underline{\boldsymbol{\Upsilon}}_k^{II}, \delta\underline{\boldsymbol{\Upsilon}}_k^{II}\rangle,\\ c_2 &= 2\langle\Delta\underline{\boldsymbol{\Upsilon}}_k + \delta\underline{\boldsymbol{\Upsilon}}_k^I, \delta\underline{\boldsymbol{\Upsilon}}_k^{II}\rangle,\\ c_3 &= \langle\Delta\underline{\boldsymbol{\Upsilon}}_k + \delta\underline{\boldsymbol{\Upsilon}}_k^I, \Delta\underline{\boldsymbol{\Upsilon}}_k + \delta\underline{\boldsymbol{\Upsilon}}_k^I\rangle - \ell^2.\end{aligned}$$

Eq. B.7 is a quadratic polynomial in $\delta\Lambda_k$, and consists of two solutions $\delta\Lambda_k$. The solution is normally chosen such that the angle between $\Delta\underline{\boldsymbol{\Upsilon}}_k$ and $\Delta\underline{\boldsymbol{\Upsilon}}_{k+1}$ is minimum, i.e. the solution $\delta\Lambda_k$ of Eq. B.7 is chosen such that $\langle\Delta\underline{\boldsymbol{\Upsilon}}_k, \Delta\underline{\boldsymbol{\Upsilon}}_{k+1}\rangle$ yields the largest value:

$$\delta\Lambda_k = \underset{\delta\tilde{\Lambda}\in\{\delta\tilde{\Lambda}|c_1\delta\tilde{\Lambda}^2+c_2\delta\tilde{\Lambda}+c_3=0\}}{\arg\max} \{\langle\Delta\underline{\boldsymbol{\Upsilon}}_k, \Delta\underline{\boldsymbol{\Upsilon}}_k + \delta\underline{\boldsymbol{\Upsilon}}_k^I + \delta\tilde{\Lambda}\delta\underline{\boldsymbol{\Upsilon}}_k^{II}\rangle\}. \tag{B.8}$$

The incremental load factor is eventually updated using Eq. B.1.
When $k = 0$ (the predictor solution), Eq. B.8 cannot be used for determination of the appropriate $\delta\Lambda_0$ because the initial guess $\Delta\underline{\boldsymbol{\Upsilon}}_0 = \underline{\mathbf{0}}$, does not contain information about the path being followed during the iterative procedure. Therefore $\delta\Lambda_0$ is chosen using

$$\delta\Lambda_0 = \pm\frac{\ell}{\|\delta\underline{\boldsymbol{\Upsilon}}_0^{II}\|_2}. \tag{B.9}$$

The success of the correct path-following technique depends highly on the choice of the sign of Eq. B.9 [24]. Possible options to determine the sign for $\delta\Lambda_0$ are

$$\text{sign } \delta\Lambda_0 = \text{sign det}(\underline{\underline{\boldsymbol{T}}}_0), \tag{B.10}$$

$$\text{sign } \delta\Lambda_0 = \text{sign}\langle\Delta\underline{\boldsymbol{\Upsilon}}_0^{II}, \underline{\boldsymbol{f}}_{ex}\rangle, \tag{B.11}$$

$$\text{sign } \delta\Lambda_0 = \text{sign}\langle\Delta\underline{\boldsymbol{\Upsilon}}^{(n)}, \delta\underline{\boldsymbol{\Upsilon}}_0^{II}\rangle, \tag{B.12}$$

where $\Delta\underline{\boldsymbol{\Upsilon}}^{(n)}$ is the incremental update of the previous increment. Eq. B.10 is widely used in commercial finite element codes, and works well in absence of bifuraction points, according to de Souza Neto and Feng [24]. Eq. B.11 is 'blind' to bifurcations, but proves to be ineffective during the descending part of the load-deflection curve, according to de Souza Neto and Feng [24]. To be

able to pass the problem of the previous two, Feng et al. [25, 26] proposed Eq. B.12, which is used in the simulations in our model.
Crisfield's arc-length method has the advantage of limiting the displacement increment for all iterations within a step to a constant value ℓ. However, the solution(s) of Eq. B.7 might be complex. Moreover, it is not guaranteed that Eq. B.8 makes the correct choice for $\delta\Lambda$ [27]. The modified Riks-Wempner arc-length method overcomes some of these disadvantages and is considered next.

B.2 Modified Riks-Wempner arc-length method

Ramm proposed a method, similar to Crisfield's one, called the modified Riks-Wempner method [27]. With the modified Riks-Wempner method, the solution is found by following a line orthogonal to $\delta\underline{\boldsymbol{\Upsilon}}_0$, expressed by

$$\langle \delta\underline{\boldsymbol{\Upsilon}}_0, \delta\underline{\boldsymbol{\Upsilon}}_k \rangle = 0. \tag{B.13}$$

The incremental update $\delta\underline{\boldsymbol{\Upsilon}}_0$ is given by

$$\delta\underline{\boldsymbol{\Upsilon}}_0 = \delta\Lambda_0 \delta\underline{\boldsymbol{\Upsilon}}_0^{II}, \tag{B.14}$$

with the load factor update given by

$$\delta\Lambda_0 = \frac{\ell}{\|\delta\underline{\boldsymbol{\Upsilon}}_0^{II}\|_2}. \tag{B.15}$$

Using Eq. B.5 the load factor becomes

$$\delta\Lambda_k = -\frac{\langle \delta\underline{\boldsymbol{\Upsilon}}_0, \delta\underline{\boldsymbol{\Upsilon}}_k^{I} \rangle}{\langle \delta\underline{\boldsymbol{\Upsilon}}_0, \delta\underline{\boldsymbol{\Upsilon}}_k^{II} \rangle}. \tag{B.16}$$

Eventually the load factor is updated using Eq. B.1. The incremental solution vector is found via substitution of Eq. B.16 in Eq. B.5, and using the relation $\Delta\underline{\boldsymbol{\Upsilon}}_{k+1} = \Delta\underline{\boldsymbol{\Upsilon}}_k + \delta\Upsilon_k$.
The modified Riks-Wempner arc-length method offers the advantage of simplicity, and there is only one value for $\delta\Lambda_k$. This avoids complex roots, and choosing the wrong update as is possible in Crisfield's arc-length method. However, the arc-length ℓ is imposed only at the first iteration, which might lead to difficulties in tracing the right solution path in case of an abrupt change [27].

C Plate equilibrium equation

The linearized equilibrium equation about an intermediate state is, according to de Böck [28], given by

$$\begin{aligned}
\sigma_{xx,x} + \sigma_{xy,y} + \sigma_{xz,z} + T_{xx}u_{1,xx} + T_{xy}u_{1,xy} + T_{yy}u_{1,yy} + f_x = 0,\\
\sigma_{yx,x} + \sigma_{yy,y} + \sigma_{yz,z} + T_{xx}u_{2,xx} + T_{xy}u_{2,xy} + T_{yy}u_{2,yy} + f_y = 0,\\
\sigma_{zx,x} + \sigma_{zy,y} + \sigma_{zz,z} + T_{xx}u_{3,xx} + T_{xy}u_{3,xy} + T_{yy}u_{3,yy} + f_z = 0,
\end{aligned} \tag{C.1}$$

with σ_{ij} the stress tensor components, T_{ij} the intermediate stresses due to stretching of the plate, u_i the displacements from Eq. 4.2, and f_i the body forces associated with the principal directions. The intermediate stresses due to stretching of the plate are given by

$$T_{xx} = \frac{N_{xx}}{h}, \qquad T_{xy} = \frac{2N_{xy}}{h}, \qquad T_{yy} = \frac{N_{yy}}{h}, \tag{C.2}$$

with $\underline{\boldsymbol{N}} = (N_{xx}, N_{yy}, N_{xy})^T$ given by Eq. 4.9. Integrating over the plate's thickness, using Eq. 4.2 with $u = v = 0$, assuming $f_i = f_i(x, y)$, $i \in \{x, y, z\}$, and neglecting all terms of $\mathcal{O}(\varepsilon^3)$, results in

$$\begin{aligned}
&\int_{-h/2}^{h/2} \left(\sigma_{xx,x} + \sigma_{xy,y} + \sigma_{xz,z} - \frac{z}{h}\left(N_{xx}w_{,xxx} + 2N_{xy}w_{,xxy} + N_{yy}w_{,xyy}\right) + f_x\right) \mathrm{d}z\\
&= N_{xx,x} + N_{xy,y} + [\sigma_{xz}]_{-h/2}^{h/2} + q_x = 0,\\
&\int_{-h/2}^{h/2} \left(\sigma_{yx,x} + \sigma_{yy,y} + \sigma_{yz,z} - \frac{z}{h}\left(N_{xx}w_{,xxy} + 2N_{xy}w_{,xyy} + N_{yy}w_{,yyy}\right) + f_y\right) \mathrm{d}z\\
&= N_{yx,x} + N_{yy,y} + [\sigma_{yz}]_{-h/2}^{h/2} + q_y = 0,\\
&\int_{-h/2}^{h/2} \left(\sigma_{zx,x} + \sigma_{zy,y} + \sigma_{zz,z} + \frac{1}{h}\left(N_{xx}w_{,xx} + 2N_{xy}w_{,xy} + N_{yy}w_{,yy}\right) + f_z\right) \mathrm{d}z\\
&= Q_{x,x} + Q_{y,y} + [\sigma_{zz}]_{-h/2}^{h/2} + N_{xx}w_{,xx} + 2N_{xy}w_{,xy} + N_{yy}w_{,yy} + q_z = 0,
\end{aligned} \tag{C.3}$$

with $q_i = \int_{-h/2}^{h/2} f_i \mathrm{d}z$, $i \in \{x, y, z\}$. Following the assumptions of Sec. 4 for the *Kirchhoff-Love plate theory* allows us to omit the boundary terms of Eq. C.3, resulting in

$$\begin{aligned}
N_{xx,x} + N_{xy,y} + q_x = 0,\\
N_{yx,x} + N_{yy,y} + q_y = 0,\\
Q_{x,x} + Q_{y,y} + N_{xx}w_{,xx} + 2N_{xy}w_{,xy} + N_{yy}w_{,yy} + q_z = 0.
\end{aligned} \tag{C.4}$$

Moment equilibrium in $x-$, respectively $y-$direction, upon using partial integration on the derivatives with respect to z, is given by (We neglect all terms of $\mathcal{O}(\varepsilon^3)$)

$$\begin{aligned}
\int_{-h/2}^{h/2} \left(z\sigma_{xx,x} + z\sigma_{xy,y} - \sigma_{xz} + zf_x\right) \mathrm{d}z = M_{xx,x} + M_{xy,y} - Q_x = 0,\\
\int_{-h/2}^{h/2} \left(z\sigma_{yx,x} + z\sigma_{yy,y} - \sigma_{yz} + zf_y\right) \mathrm{d}z = M_{yx,x} + M_{yy,y} - Q_y = 0,
\end{aligned} \tag{C.5}$$

with

$$\begin{aligned}
Q_x = \int_{-h/2}^{h/2} \sigma_{xz} \mathrm{d}z,\\
Q_y = \int_{-h/2}^{h/2} \sigma_{yz} \mathrm{d}z.
\end{aligned} \tag{C.6}$$

The shear forces Q_x and Q_y are eliminated via substitution of Eq. C.5 in equation Eq. C.4, resulting in

$$\begin{aligned} N_{xx,x} + N_{xy,y} + q_x &= 0, \\ N_{yx,x} + N_{yy,y} + q_y &= 0, \\ M_{xx,xx} + 2M_{xy,xy} + M_{yy,yy} &= -\left(q_z + N_{xx}w_{,xx} + 2N_{xy}w_{,xy} + N_{yy}w_{,yy}\right), \end{aligned} \tag{C.7}$$

which is the desired result.